

## ABSTRACT

PAYNE, ALEXIS LEILANI. A Characterization Platform for 3D Ferroelectric Thin Films. (Under the direction of Dr. Jacob L. Jones).

Recent advances in producing ferroelectric thin films via atomic layer deposition has enabled the conformal coating of 3D objects, these 3D ferroelectric thin films are useful in applications such as microrobotics, energy storage, and nonvolatile memory. To advance 3D ferroelectric thin films into state of the art devices, questions related to limitations of the conformality of the thin film growth as well as their crystallization and electrical response on these 3D platforms need to be answered. In this work, a 3D structured substrate was designed to be a broad characterization tool for 3D ferroelectrics with structures dedicated to planar and 3D electrical performance, crystallography, piezoelectric, thermal, and resonant properties. As a demonstration of the functionality of the platform, antiferroelectric Al:HfO<sub>2</sub> thin films were used. A robust study characterizing planar Al:HfO<sub>2</sub> thin films grown via atomic layer deposition for energy storage applications with either 4 at% or 8 at% dopant concentration and a film thickness of 20 nm either 50 nm was conducted. 50nm thick 8 at% Al-doped HfO<sub>2</sub> showed a maximum energy storage density of 63 J/cm<sup>3</sup> while maintaining an efficiency of 85%. The loss tangents of the thin films were under 2% over the range of -4 to 4 MV/cm and at frequencies ranging from 500 Hz-100 kHz. A further study compared Pt/ 50 nm 4 at% Al:HfO<sub>2</sub>/Pt and TiN/50 nm 4 at% Al:HfO<sub>2</sub>/TiN devices and how their polarization-electric field loops and loss tangent varied with respect to temperature, -125 °C to 125 °C. The devices with their different electrodes, either TiN or Pt, were expected to different defect chemistries. However, both sets of capacitors showed similar leakage current density and loss tangent values, and were determined to have remarkably stable polarization-electric field hysteresis loops with over the entire temperature range measured.

A TiN/50 nm 4 at% Al:HfO<sub>2</sub>/TiN thin film was deposited onto the 3D structured characterization platform. The electric properties of the thin film differed between planar capacitors and area enhanced capacitors (AECs) as expected. The crystal structure of the thin film deposited on the sidewalls, which were specifically analyzed using a blanket ion mill of a high density AEC, were found to have less tetragonal phase relative to the entire AEC. The first ever reported released cantilever for a HfO<sub>2</sub>-based thin film was created and actuated, and from the measurement of the actuation of the cantilever the indirect transverse piezoelectric coefficient was calculated,  $e_{31,f}^*$ . The nonlinear  $e_{31,f}^*$  was extracted as a function of voltage, with a zero field  $e_{31,f}^*$  value of 1.38 C/m<sup>2</sup> being observed. The positive  $e_{31,f}^*$  was opposite of theorized and suggests that the antiferroelectric-like nature of the 4 at% Al:HfO<sub>2</sub> thin films could be indeed due to an electrically field driven by a phase transition from non-polar tetragonal to polar orthorhombic.

A Characterization Platform for 3D Ferroelectrics

by  
Alexis Leilani Payne

A thesis submitted to the Graduate Faculty of  
North Carolina State University  
in partial fulfillment of the  
requirements for the degree of  
Doctor of Philosophy

Materials Science and Engineering

Raleigh, North Carolina

2021

APPROVED BY:

---

Jacob L. Jones  
Committee Chair

---

Brendan Hanrahan  
External Member

---

Aram Amassian

---

Veronica Augustyn

---

Gregory Parsons

## **DEDICATION**

To my loved ones who helped lift me back up when I was at my lowest

## **BIOGRAPHY**

Alexis Payne was born in Honolulu, Hawaii as her father was stationed there as a medical doctor in the United States Army. She always enjoyed and excelled at math as a young girl and took her first physics class in high school. The course went on to inspire her to obtain her B.S. in Physics from the College of Charleston in 2015. After graduating, Alexis worked in the Research and Development Department at Northrop Grumman SYNOPTICS in Charlotte, NC. During her time there, she met many other scientists and engineers with doctorates in Materials Science and Engineering. Her discussions with them about her desires for her career as well as an introduction to the exciting field of materials led her to apply to the graduate program in Materials Science and Engineering at NCSU. After an initial year of coursework, Alexis began her dissertation research under the advisement of Dr. Jacob L. Jones. During her third year of her program, she was awarded a fellowship at the Army Research Laboratory (ARL) in Adelphi, MD to conduct and complete her dissertation research.

## ACKNOWLEDGEMENTS

I first would like to acknowledge and thank my advisors, Professor Jacob L. Jones and Dr. Brendan Hanrahan, for their advice related to both scientific and non-scientific topics. They both have fostered and grown my ability to problem solve, to communicate scientific knowledge effectively, and to ask critical questions among other skills. They also both were extremely supportive in some difficult moments, and for that I will always be especially grateful.

There were also numerous other collaborators involved in this work that deserve special thanks. I would be remiss if I did not thank Nicholas Strnad for his development of the atomic layer depositions conducted at ARL and his continuous advice on designing experiments. I also want to thank the clean room manager, Robert Burke, and many of the cleanroom staff that contributed to this work, Jaron Krupp, Madhu Roy, and James (Jim) Mulcahy. Also thanks to Robert Bruce, for his help with developing the deep reactive ion etching process, as well as Brian Power and Robert Benoit for their occasional expertise on sputtering or lithography. I also want to thank Ryan Rudy for all the device designs he contributed to this work as well as the instruction he provided on resonators and actuators. I also would like to thank Dr. Mike Waits and Dr. Sarah Bedair and the rest of the Energy Conversion Branch at ARL. I also need to thank my fellow group members, H. Alex Hsain and Younghwan Lee, who produced the thin films that were grown at NCSU. I also would like to thank other former and current members of the Jones research group Rachel Broughton, Alexandra (Ali) Henriques, Dr. Alexandria Cruz, Dr. Jianwei Zhou, Dr. Hanhan Zhou, and Dr. Alisa Paterson, for their advice on presentations, manuscripts, and more.

I would also like to thank my parents, Carol and Charles Payne, for always encouraging and fostering a love of mathematics and science in me. Special thanks to my fiancé, Nathan

Sesar, for his multiple readings of this dissertation and his constant encouragement. I also would like to thank and mention a few fast friends who supported me on this journey to obtaining my doctorate, specifically Kalah Seidel, Hanna Morehead, and Aubrey Penn, I do not know if I would have persevered if not for you all.

Finally, this project was supported in part by a fellowship at the US CCDC Army Research Laboratory, administered by Oak Ridge Associated Universities (ORAU) through the U.S. Department of Energy Oak Ridge Institute for Science and Education. Partial support for this work came from the National Science Foundation under award number CMMI-1634955. This work benefited from another collaboration with the National Science Foundation, as part of the Center for Dielectrics and Piezoelectrics under Grant Nos. IIP-1841453 and IIP-1841466. I also acknowledge Analytical Instrumentation Facility for providing advanced scientific instruments, which is supported by the State of North Carolina and the National Science Foundation under award No. ECCS-1542015.

# TABLE OF CONTENTS

<b>LIST OF TABLES</b> .....	viii
<b>LIST OF FIGURES</b> .....	ix
<b>Chapter 1: Introduction and Background</b> .....	1
<b>1.1. Dielectric, Ferroelectrics, Antiferroelectric Materials</b> .....	1
1.1.1. Relationship Between Dielectric, Ferroelectrics, and Antiferroelectrics .....	1
1.1.2. Applications for Ferroelectric Thin Films.....	3
<b>1.2. 3D Ferroelectrics</b> .....	6
1.2.1. Atomic Layer Deposition.....	8
1.2.2. Ferroelectric HfO <sub>2</sub> .....	9
1.2.3. Motivation for Continued Research into 3D Ferroelectrics .....	10
<b>1.3. Thesis Overview</b> .....	12
<b>References</b> .....	13
<b>Chapter 2: Literature review of HfO<sub>2</sub> Ferroelectric Thin Films</b> .....	16
<b>2.1. Origin of Ferroelectricity in HfO<sub>2</sub></b> .....	16
2.1.1. Ferroelectric Response Impact Factors .....	17
2.1.2. Driving Mechanisms for AFE-like Response .....	22
<b>2.2. Critical Parameters for Device Creation</b> .....	23
2.2.1. Rated Capacitance, Rated Voltage, and Breakdown Voltage .....	23
2.2.2. Relative Dielectric Permittivity .....	24
2.2.3. Piezoelectric Coefficient .....	25
2.2.4. Leakage Current Density .....	25
2.2.5. Loss Tangent .....	27
2.2.6. Electrical Characteristics vs. Temperature and Frequency .....	28
2.2.7. Reliability Metrics .....	31
<b>References</b> .....	34
<b>Chapter 3: Characterization Platform Overview</b> .....	38
<b>3.1. Characterization Structures</b> .....	38
3.1.1. Planar Areas .....	38
3.1.2. Area Enhanced Structures .....	39
3.1.3. Theta Mechanical Testing Structures .....	42
3.1.4. Cantilevers .....	43
3.1.5. Actuators .....	45
3.1.6. Resonators .....	46
3.1.7. Trenches for Sidewall Crystal Structure Characterization .....	47
<b>3.2. Process Flow Overview</b> .....	48
3.2.1. Photolithography .....	48
3.2.2. Deep Reactive Ion Etching .....	49
3.2.3. TiN/Al:HfO <sub>2</sub> /TiN Sample Creation .....	51
3.2.4. Ion Milling .....	52
3.2.5. Contact Pad Creation .....	54
3.2.6. Release Etch .....	55

<b>References</b> .....	57
<b>Chapter 4: Application Driven Characterization of Planar HfO<sub>2</sub> Films</b> .....	58
<b>4.1. AFE-like Al:HfO<sub>2</sub> Thin Films for Energy Storage</b> .....	58
4.1.1. Planar Capacitor Production with Pt Electrodes.....	58
4.1.2. Structural Characterization .....	60
4.1.3. Energy Storage Density and Efficiency.....	61
4.1.4. Operating Voltage, Breakdown Voltage, Reliability.....	64
<b>4.2. Thermal Stability of AFE-like Al:HfO<sub>2</sub> with Pt or TiN Electrodes</b> .....	69
4.2.1. Polarization Electric Field Loops vs. Temperature .....	69
4.2.2. GIXRD Patterns .....	71
4.2.3. ESD, Efficiency, and Losses.....	73
4.2.4. Endurance Cycling.....	77
<b>References</b> .....	82
<b>Chapter 5: 3D AFE-like Al:HfO<sub>2</sub> Thin Film Characterization</b> .....	84
<b>5.1. Area Enhanced Capacitor Electrical Measurements</b> .....	84
<b>5.2. Sidewall Thin Film Crystal Structure</b> .....	87
<b>5.3. Piezoelectric Response</b> .....	92
<b>References</b> .....	102
<b>Chapter 6: Conclusions and Future Outlook</b> .....	104
<b>6.1. Conclusions</b> .....	104
<b>6.2. Future Outlook</b> .....	108
6.2.1. Fine Tuning Dopant Concentration of Al:HfO <sub>2</sub> .....	108
6.2.2. Other 3D Ferroelectric Thin Film Growth and Characterization .....	108
<b>References</b> .....	112

## LIST OF TABLES

Table 3.1. List of types of area enhanced capacitors with type of structure, diameter or width of structure, number of structures, electrode footprint, and surface area enhancement in order of surface area enhancement. ....	40
Table 3.2. List of type of cantilever produced, along with beam length(s), and number of that type of cantilever per quadrant 2 found on the substrate.....	44
Table 4.1. A list of the composition of the planar capacitors along with the thickness of the Al:HfO <sub>2</sub> thin films.....	59
Table 4.2. Electrical characteristics of Al:HfO <sub>2</sub> Capacitors .....	65
Table 5.1. Thickness, width, length, and Young's modulus of each layer of the cantilever.....	96

## LIST OF FIGURES

Figure 1.1. A schematic demonstrating the relationship between dielectric materials, piezoelectric materials, pyroelectric materials, and ferroelectric materials.....	2
Figure 1.2. A schematic of example P-E loops for a linear dielectric, ferroelectric, and antiferroelectric, with the area in green representing the energy storage density of the material and the area in red demonstrating the energy lost in the material.....	5
Figure 1.3. (a) Schematic of a classic 2D ferroelectric, (b) schematic of an example 3D ferroelectric.....	6
Figure 1.4. Dose Sequence for an ALD process.....	8
Figure 2.1. Pressure – temperature phase diagram for bulk HfO <sub>2</sub> with the dotted lines representing assumed boundaries. © 2018 WILEY-VCH Verlag GmbH & Co. KGaA, Weinheim.....	17
Figure 2.2. A schematic illustrating how charged defects can pin domains, but as they move the pinned domains become unpinned. <sup>30</sup> Reprinted (adapted) with permission from Patrick D. Lomenzo, Claudia Richter, Thomas Mikolajick, and Uwe Schroeder, Depolarization as Driving Force in Antiferroelectric Hafnia and Ferroelectric Wake-Up, ACS Applied Electronic Materials 2 (6), 1583 (2020). Copyright 2020 American Chemical Society.....	21
Figure 2.3. Schematic of the t-phase, P4 <sub>2</sub> /nmc, crystal structure for HfO <sub>2</sub> and the o-phase, Pca2 <sub>1</sub> , crystal structure with the a- axis along the [110] for HfO <sub>2</sub> and the o-phase, Pca2 <sub>1</sub> , crystal structure for HfO <sub>2</sub> .....	22
Figure 2.4. Leakage current density vs. voltage plots for (a) 5.5-, (b) 10-, (c) 17-, and (d) 25-nm-thick Hf <sub>0.5</sub> Zr <sub>0.5</sub> O <sub>2</sub> thin films with annealing temperature of 400-800 °C,	

respectively.<sup>24</sup> Reprinted from [Min Hyuk Park, Han Joon Kim, Yu Jin Kim, Woongkyu Lee, Taehwan Moon, and Cheol Seong Hwang, Evolution of phases and ferroelectric properties of thin  $\text{Hf}_{0.5}\text{Zr}_{0.5}\text{O}_2$  films according to the thickness and annealing temperature, *Applied Physics Letters* **102** (24), 242905 (2013)], with the permission of AIP Publishing..... 27

Figure 2.5. (A) Temperature dependent PV loops ranging from 100 to 400 K for  $\text{Hf}_{0.5}\text{Zr}_{0.5}\text{O}_2$ ,  $\text{Hf}_{0.3}\text{Zr}_{0.7}\text{O}_2$ , and  $\text{ZrO}_2$ . (B) Increasing temperature dependence of the permittivity is observed from  $\text{Hf}_{0.5}\text{Zr}_{0.5}\text{O}_2$  over  $\text{Hf}_{0.3}\text{Zr}_{0.7}\text{O}_2$  towards  $\text{ZrO}_2$ .<sup>16</sup> Reprinted (adapted) with permission from Johannes Müller, Tim S. Böske, Uwe Schröder, Stefan Mueller, Dennis Bräuhaus, Ulrich Böttger, Lothar Frey, and Thomas Mikolajick, *Ferroelectricity in Simple Binary  $\text{ZrO}_2$  and  $\text{HfO}_2$* , *Nano Letters* **12** (8), 4318 (2012). Copyright 2012 American Chemical Society..... 29

Figure 2.6. An SEM image of a doubly clamped resonator based on TiN/HZO/TiN stack with an aspect ratio exceeding  $10^4:1$ .<sup>63</sup> Reprinted from [M. Ghatge, G. Walters, T. Nishida, and R. Tabrizian, A 30-nm thick integrated hafnium zirconium oxide nano-electro-mechanical membrane resonator, *Applied Physics Letters* **116** (4), 043501 (2020)], with the permission of AIP Publishing..... 31

Figure 2.7. Plot of ESD and efficiency of (a) Si:HZO and (b) Al:HZO thin films at different electric fields.<sup>59</sup> Reprinted from [Patrick D. Lomenzo, Ching-Chang Chung, Chuanzhen Zhou, Jacob L. Jones, and Toshikazu Nishida, Doped  $\text{Hf}_{0.5}\text{Zr}_{0.5}\text{O}_2$  for high efficiency integrated supercapacitors, *Applied Physics Letters* **110** (23), 232904 (2017)], with the permission of AIP Publishing..... 32

Figure 3.1. AutoCAD drawing of a 25 mm x 25 mm chip on the 6" wafer, the chip contains 4 quadrants separated by a 5 mm wide cross section of holes, trenches, and fins outlined in green. The schematic also shows the 5th quadrant design as well..... 39

Figure 3.2. (a) Schematic of trench capacitor, (b) schematic of capacitor with holes, (c) schematic of pillar array capacitor, (d) SEM image of cross section of trenches with variable widths and depths..... 40

Figure 3.3. (a) Schematic of theta mechanical test structure (b) SEM image of theta mechanical test structure..... 42

Figure 3.4. (a) Schematic of an M-cantilever, (b) schematic of a piano key cantilever, (c) SEM image of an M-cantilever, (d) Optical microscope image of a piano-key cantilever..... 43

Figure 3.5. (a) Schematic of a cymbal actuator from a top-down perspective, (b) a 3D schematic of the cymbal actuator, (c) an optical microscope image of a 5-cymbal actuator..... 45

Figure 3.6. (a) Schematic of a butterfly actuator with arrows in the direction of actuation. (b) An optical microscope image of a butterfly actuator..... 46

Figure 3.7. Schematic of trenches pre and post ion milling leaving the thin film on the sidewalls of the trenches for XRD analysis..... 47

Figure 3.8. (a) Schematic of silicon wafer after applying photoresist, (b) schematic of patterning the photoresist using an optical mask with a UV dose, (c) silicon with photoresist after developing the photoresist..... 48

Figure 3.9. Schematic of the deep reactive ion etching process of a silicon wafer with a patterned photoresist (P.R.)..... 50

Figure 3.10. An SEM image of the various trench structures with their widths and lengths labeled.....	51
Figure 3.11. (a) Schematic of the sample layers after ALD deposition, (b) schematic of sample after defining top electrodes via ion milling, (c) schematic of sample after bottom electrode is exposed via ion milling.....	54
Figure 4.1. (a) GIXRD of all four Al:HfO <sub>2</sub> compositions, (b) around largest intensity orthorhombic/tetragonal peak and monoclinic peaks between 27°-33°.....	61
Figure 4.2. Monopolar loops taken at increasing fields for (a) 4 at% Al:HfO <sub>2</sub> 20 nm (b) 4 at% Al:HfO <sub>2</sub> 50 nm (c) 8 at% Al:HfO <sub>2</sub> 20 nm (d) 8 at% Al:HfO <sub>2</sub> 50 nm for the calculation of energy storage density values (d) shows only intermittent loops due significantly overlapping curves.....	62
Figure 4.3. (a) Polarization versus electric field loops of thin film Al:HfO <sub>2</sub> of various compositions and thicknesses at 75% E <sub>BD</sub> and (b) ESD and η calculations with increasing applied field.....	63
Figure 4.4. Weibull distribution of breakdown field for each Al:HfO <sub>2</sub> sample with the Weibull modulus listed for each one. The x'd data points were excluded from calculations as they suffered from early “infant mortality” failure.....	64
Figure 4.5. The endurance of the Al:HfO <sub>2</sub> films cycled at 40% of E <sub>BD</sub> up to 10 <sup>6</sup> -10 <sup>7</sup> cycles with a triangular waveform. How the P <sub>r</sub> (dashed) and P <sub>max</sub> (solid) change over this range of cycling is shown.....	66
Figure 4.6. The relative dielectric permittivity and loss tangent vs. electric field (a) and frequency (b) for the Al:HfO <sub>2</sub> thin films.....	67
Figure 4.7. P-E loops of (a) TiN/ 50 nm 4 at % Al:HfO <sub>2</sub> /TiN and (b) Pt/ 50 nm 4 at% Al:HfO <sub>2</sub> /Pt from -125 °C to 125 °C at 25 °C steps.....	70

Figure 4.8. GIXRD patterns of TiN/ 50nm 4 at% Al:HfO<sub>2</sub>/TiN and Pt/ 50nm 4 at% Al:HfO<sub>2</sub> with reference XRD patterns for the orthorhombic phase (PDF 04-005-559), the tetragonal phase (04-011-882), and the monoclinic phase (PDF 00-034-0104) shown below..... 72

Figure 4.9. ESD and efficiency values measured calculated from 15 V monopolar hysteresis loops taken every 25 °C from -125 °C to 125 °C..... 73

Figure 4.10. Leakage current measurements of (a) TiN/50 nm 4 at% Al:HfO<sub>2</sub>/TiN sample and (b) Pt/50 nm 4 at% Al:HfO<sub>2</sub>/Pt at temperatures from -125 °C to 125 °C at 25 °C intervals..... 74

Figure 4.11. Relative permittivity and loss tangent values of TiN/ 50 nm 4 at% Al:HfO<sub>2</sub>/TiN and (Pt/ 50 nm 4 at% Al:HfO<sub>2</sub>/Pt from -125 °C to 125 °C at 25 °C steps..... 75

Figure 4.12. Dielectric permittivity vs. frequency of (a) TiN/50 nm 4 at% Al:HfO<sub>2</sub>/TiN sample and (b) Pt/50 nm at% Al:HfO<sub>2</sub>/Pt taken every 25 °C from -125 °C to 125 °C..... 76

Figure 4.13. Remanent polarization (P<sub>r</sub>) and maximum polarization (P<sub>max</sub>) vs. number of cycles for (a) TiN/ 50 nm 4 at% Al:HfO<sub>2</sub>/TiN and (b) Pt/ 50 nm 4 at% Al:HfO<sub>2</sub>/Pt at -125 °C, 25 °C , and 125 °C..... 77

Figure 4.14. Pre and post endurance cycling P-E loops at -125 °C, 25 °C, and 125 °C for (a) TiN/50 nm 4 at% Al:HfO<sub>2</sub>/TiN sample and (b) Pt/50 nm at% Al:HfO<sub>2</sub>/Pt..... 78

Figure 4.15. Pre and post endurance cycling leakage current measurements at -125 °C, 25 °C, and 125 °C for (a) TiN/50 nm 4 at% Al:HfO<sub>2</sub>/TiN sample and (b) Pt/50 nm at% Al:HfO<sub>2</sub>/Pt..... 79

Figure 5.1. (a) P-E loops with increasing voltage of a planar capacitor (b) P-E loops with increasing voltage of AEC, specifically a trench capacitor that has twenty trenches that are 2  $\mu\text{m}$  wide and 10  $\mu\text{m}$  deep. The AEC has a surface area enhancement of 1.85 over the planar capacitor ..... 84

Figure 5.2. (a) ESD as a function of applied voltage for the AEC, containing twenty trenches that are 2  $\mu\text{m}$  wide and 10  $\mu\text{m}$  deep, using the foot print area of the AEC for the calculation, using the estimated surface area (up and over trenches) denoted as the normalized AEC, and the ESD of the planar capacitor, (b) efficiency of the AEC and the planar capacitor vs. applied voltage ..... 85

Figure 5.3. (a) monopolar P-E loops as a function of applied electric field for the planar capacitor used to calculate ESD and efficiency (b) monopolar P-E loops as a function of applied electric field for the AEC, containing twenty trenches that are 2  $\mu\text{m}$  wide and 10  $\mu\text{m}$  deep, the area used in calculating the polarization was the footprint of the AEC..... 86

Figure 5.4. Leakage current density measurements for both the planar capacitor and the AEC capacitor containing twenty trenches that are 2  $\mu\text{m}$  wide and 10  $\mu\text{m}$  deep..... 87

Figure 5.5. A schematic of the trench structures mounted with respect to the source and detector of the XRD source.  $\omega$  and  $2\theta$  represent the angle of the incident beam and reflected beam respectively,  $\chi$  represents the sample tilt angle, and  $\phi$  represents the sample spin angle..... 88

Figure 5.6. XRD Pattern of the full capacitor prior to being ion milled, and then the capacitor after being ion milled with only sidewall thin film remaining..... 89

Figure 5.7. Bragg Brentano XRD Patterns from 27° to 32.5°, along with the peak positions for the o-phase (PDF 04-005-5597), t-phase (PDF 04-011-8820), and the m-phase (00-034-0104). The peak positions of the PDFs have been shifted from original positions to compensate for strain.....	89
Figure 5.8. (a) $\omega$ -rocking curve, (b) $\Phi$ -rocking curve, (c) $\chi$ -rocking curve around o111/t101 HfO <sub>2</sub> peak.....	91
Figure 5.9. (a) Schematic representing the M-cantilever upon release with the position of the laser from the LDV denoted as well as the initial radius, $R_i$ , (b) an optical microscope image of the M-cantilever as measured by the LDV, with the laser spot showing up as a white dot on the backside of the curled M-cantilever.....	92
Figure 5.10. Plot of displacement of top of M-cantilever versus applied electric field.....	93
Figure 5.11. Plot of $e_{31}$ versus electric field for the SiO <sub>2</sub> /TiN/Al:HfO <sub>2</sub> /TiN M-cantilever.....	97
Figure 5.12. A displacement versus applied voltage plot after increasing number of electric field cycles was applied to a 175 $\mu\text{m}$ M-cantilever, consisting of SiO <sub>2</sub> /TiN/Al:HfO <sub>2</sub> /TiN.....	100
Figure 6.1. A plot of $P_r$ and relative dielectric permittivity as a function of Al-dopant concentration in HfO <sub>2</sub> thin films.....	108
Figure 6.2. Energy storage density, energy loss (a), and efficiency (b) at 3 V of planar 10 nm thick Si:HfO <sub>2</sub> thin films as a function Si-dopant concentration. Reprinted with permission from [Kati Kühnel, Malte Czernohorsky, Clemens Mart, and Wenke Weinreich, Journal of Vacuum Science & Technology B <b>37</b> (2), 021401 (2019).Copyright 2019, American Vacuum Society.....	109

Figure 6.3. (a) P-E loops for a 20nm, 50nm, and 200 nm PbHfO<sub>3</sub> thin films taken at 1 kHz, (b) leakage current density versus applied electric field for each thickness measured, (c) fatigue measurements for the 20 nm thin film. Reproduced from [Brendan Hanrahan, Cosme Milesi-Brault, Asher Leff, Alexis Payne, Shi Liu, Mael Guennou, and Nicholas Strnad, The other model antiferroelectric: PbHfO<sub>3</sub> thin films from ALD precursors, *APL Materials* **9** (2), 021108 (2021).], with the permission of AIP Publishing..... 110

## Chapter 1. Introduction and Background

### 1.1. Dielectric, Ferroelectric, Antiferroelectric Materials

#### 1.1.1. Relationship between Dielectrics, Ferroelectrics, and Antiferroelectrics

Dielectrics are a class of materials that are electrical insulators that can be strongly polarized by an applied electric field. Polarization occurs as the electric dipoles in the material are aligned along the direction of the applied electric field, resulting in the separation of positive and negative charge. A subclass of dielectric materials is piezoelectric materials. Piezoelectric materials exhibit a linear response of charge development on their surface when a mechanical stress is exerted on them. Piezoelectricity is a property only present in materials with noncentrosymmetric crystal structures. Out of the 32 crystal point groups, 21 are noncentrosymmetric and of those 20 are piezoelectric. The crystal structure must be noncentrosymmetric in order to generate a net dipole moment under stress<sup>1</sup>. The direct piezoelectric coefficient ( $d_{ijk}$ ) quantifies the proportionality of the electrical response, polarization ( $P_i$ ), to the magnitude of the applied stress ( $\sigma_{jk}$ ), as described in Eq. (1 – 1)<sup>1</sup>:

$$P_i = d_{ijk}\sigma_{jk} \quad (1 - 1)$$

There is also the inverse or indirect piezoelectric coefficient ( $e_{ijk}$ ) which describes the proportionality of the strain ( $\epsilon_{ij}$ ) induced in a material to the magnitude of the applied electric field ( $E_k$ ), as described in Eq. (1 – 2)<sup>1</sup>:

$$\epsilon_{ij} = e_{ijk}E_k \quad (1 - 2)$$

A subclass of piezoelectric materials is pyroelectric materials. Consequentially, these materials also have noncentrosymmetric crystal structures, but in addition they need to be able to support an electrical dipole moment in an unstrained state. Of the 20 crystal structures that are

piezoelectric, only 10 are pyroelectric<sup>1</sup>. Pyroelectric materials have a spontaneous polarization which changes with a change in temperature, absent of an applied electric field.

A subclass of pyroelectric materials is ferroelectric materials. These materials have to have the polar non-centrosymmetric crystal structures of pyroelectrics, but have a spontaneous polarization that can be switched under the application of an applied electric field. Some pyroelectrics are not ferroelectrics because the material will experience dielectric breakdown before a reorientation of the polarization of the material<sup>1</sup>. There are no crystallographic distinctions between pyroelectrics and ferroelectrics. The relationship between dielectrics, piezoelectrics, pyroelectrics, and ferroelectrics as shown in Figure 1.1.

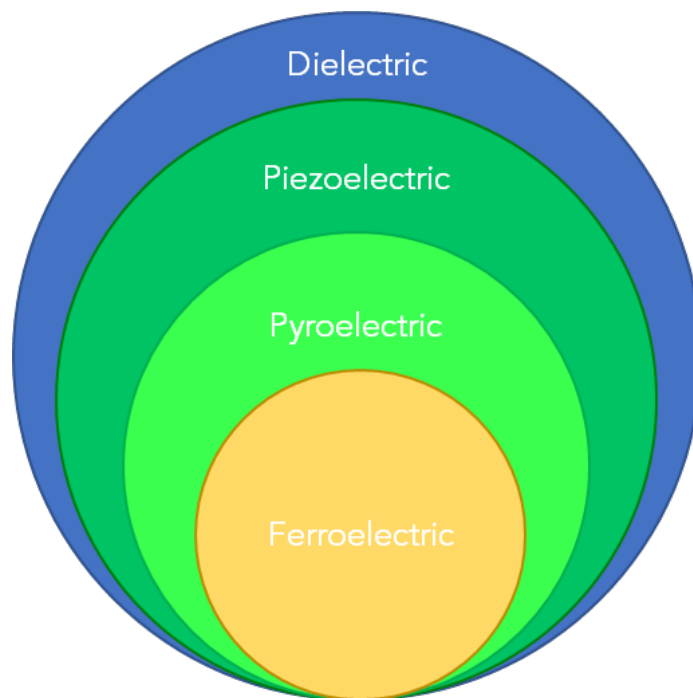


Figure 1.1. A schematic demonstrating the relationship between dielectric materials, piezoelectric materials, pyroelectric materials, and ferroelectric materials.

There is also a class of materials known as antiferroelectrics (AFEs). Originally, AFEs were defined by Kittel in 1951 as a material in which lines of ions in the crystal are spontaneously polarized in antiparallel directions<sup>2</sup>. Thus, in the absence of an applied electric

field there is no net polarization. In practice, AFE materials are identified from their double polarization-electric field (PE) hysteresis loop and a phase transition between two non-polar phases accompanied by a dielectric anomaly<sup>3</sup>. One of the first materials discovered to be AFE was  $\text{PbZrO}_3$  (PZO) in 1951<sup>4</sup>. The origin of the AFE response in PZO has since been determined to be due to the antiparallel alignment of lead ions and the tilting of oxygen octahedra<sup>5</sup>. Thus, even PZO does not fit the definition proposed by Kittel perfectly. More recent works have striven to provide a more robust definition defined by symmetry arguments<sup>3,6</sup>, which aim to determine the physical origin of an AFE response in a material. However, even with progress on providing a definitive list of properties a crystal structure must have to be considered an AFE, the ability to pre-determine what materials will be AFE has yet to come to fruition.

### 1.1.2. Applications for Ferroelectric Thin Films

In 1920, the first material discovered to be ferroelectric was Rochelle salt ( $\text{KNaC}_4\text{H}_4\text{O}_6 \cdot 4\text{H}_2\text{O}$ )<sup>7</sup>. Since its discovery, many more ferroelectric materials have been discovered, most notably  $\text{PbZr}_x\text{Ti}_{1-x}\text{O}_3$  (PZT) (1952)<sup>8</sup> and  $\text{BaTiO}_3$ (1946)<sup>9</sup>. The first ferroelectric thin film was a  $\text{BaTiO}_3$  thin film and it was produced in 1955<sup>10</sup>. Since then, many more compositions of ferroelectric thin films have been produced and subsequently used in non-volatile memory<sup>11</sup>, microwave devices<sup>12</sup>, pyroelectric(thermal) sensors<sup>13</sup>, piezoelectric microactuators<sup>14</sup>, and other applications.

The use of ferroelectric thin films in memory devices stem from their ability to stay polarized after the removal of an applied electric field. Their polarization can also be reversed, thus they inherently have a positive and a negative remanent polarization ( $P_r$ ) state. These two states are readily defined as the computational ‘1’ or ‘0’ in a memory device<sup>15</sup>. Ferroelectric random access memory (FRAM) devices have read and write speeds less than 100 ns<sup>15</sup> and

relatively low power consumption, making them competitive commercial devices<sup>15</sup>. The ability of the polarization of ferroelectric thin films to be reversed also enables their use in ferroelectric field effect transistors (FeFETs). These devices are also primarily considered for memory applications and have the advantage over FRAM devices in that they have nondestructive readout<sup>15</sup>. However, FeFET memories have yet to become widely commercially available as the first demonstration of viability in a mainstream complementary metal oxide semiconductor (CMOS) process only recently occurred in 2016<sup>16</sup>. The other applications ferroelectric thin films are found in often rely on their pyroelectric or piezoelectric properties. Their pyroelectric properties are often used for IR sensors and motion detectors<sup>17,18</sup>, as small changes in thermal radiation result in changes in the surface charge of the pyroelectric thin film, which can be detected by a FET in the device. Pyroelectric thin films are also considered for recovering energy from waste heat<sup>19</sup>, wireless power transmission<sup>20</sup>, and novel portable power devices<sup>13</sup>.

The piezoelectric behavior inherent to ferroelectric thin films has lead to a whole class of piezoelectric microelectric mechanical systems (piezoMEMS), which are MEMS that achieve actuation via the piezoelectric effect rather than another mechanism such as thermal expansion or electrostatic transduction. Some example of piezoMEMS are acoustoelectric components, such as surface acoustic wave (SAW) filters<sup>15,21</sup> and bulk acoustic wave (BAW) filters<sup>22</sup>, as well as types of resonators<sup>23-25</sup>. Other piezoMEMS are devices such as gyroscopes<sup>26,27</sup>, actuators<sup>28</sup>, and transducers<sup>29</sup>. Piezoelectric thin films have also been incorporated into some initial microrobotic devices, such as micropositioners<sup>30</sup>, microrobotic legs<sup>31,32</sup>, and a microrobotic wing<sup>33</sup>.

AFE thin films have found use in decoupling capacitors and filters, however, they are most prominently used in energy storage devices. AFEs were considered for energy storage

applications as early as 1961 by Jaffe *et al.*<sup>34</sup>. The energy storage density of a material can be calculated by the integration of electric field,  $E$ , with respect to the polarization,  $P$ , as follows<sup>35</sup>:

$$W_{tot} = \int_0^{P_{max}} E dP \quad (1 - 3)$$

$$W_{rec} = \int_{P_{max}}^{-P_r} E dP \quad (1 - 4)$$

Where the total energy density is  $W_{tot}$  and the recoverable energy density is  $W_{rec}$ , most often referred to as the energy storage density (ESD). Materials with higher maximum polarization ( $P_{max}$ ) values, such as ferroelectrics and AFEs, have larger ESDs than dielectrics, which have lower  $P_{max}$  values. The energy storage density lost ( $W_{loss}$ ) in the system is the  $W_{tot} - W_{rec}$ , and is calculated by the area within the P-E hysteresis loop. Figure 1.2. demonstrates the ESD, area in green, and energy lost, area in red, for a linear dielectric, ferroelectric, and AFE.

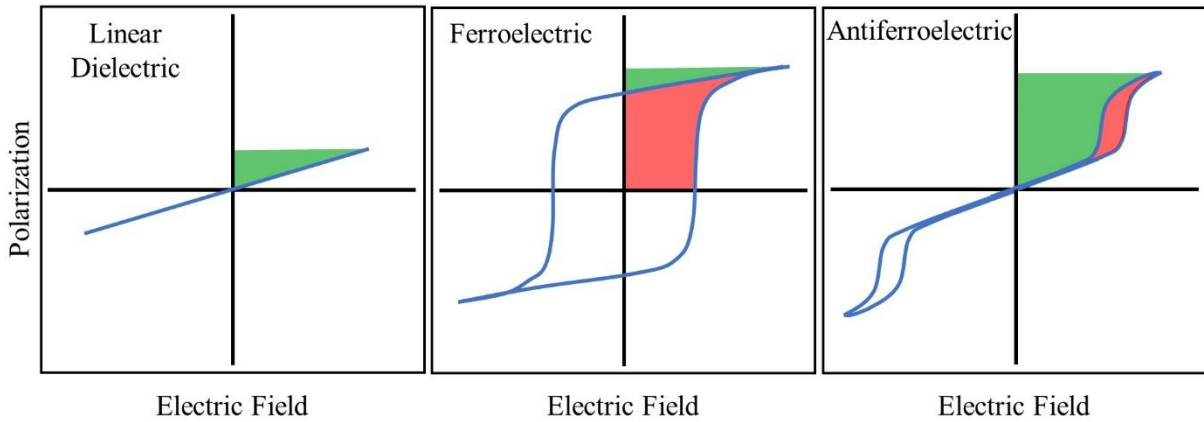


Figure 1.2. A schematic of example P-E loops for a linear dielectric, ferroelectric, and antiferroelectric, with the area in green representing the energy storage density of the material, and the area in red demonstrating the energy lost in the material.

A material with a larger hysteresis, such as a ferroelectric, has higher losses than a material with no hysteresis, such as a linear dielectric. The efficiency of the system is defined by the following:

$$\eta = \frac{W_{rec}}{W_{tot}} = \frac{W_{rec}}{W_{rec} + W_{loss}} \quad (1 - 5)$$

Thus, the AFE balances these two desired properties of large maximum polarization with slimmer hysteresis, resulting in an ideal material for energy storage applications. Another device that uses AFE thin films is decoupling capacitors, which are used to remove an AC signal while retaining a DC component<sup>36</sup>. The AFE thin film upon receiving a high voltage will become polarized, then upon backswitching to the unpolarized state the polarization charge becomes released at a fixed voltage. This fixed voltage release makes high pulses of power manageable to an integrated circuit. Also, the rate at which the backswitching speed occurs from the polarized to the unpolarized state is on the order of nanoseconds<sup>37</sup>. These combined qualities make AFE thin films ideal for high power decoupling capacitors.

## 1.2. 3D Ferroelectrics

The majority of the previously discussed applications for ferroelectric thin films have used “2D ferroelectrics,” meaning they consist of a planar substrate onto which a bottom electrode is deposited, followed by a ferroelectric thin film, and then a top electrode (Figure 1.3a.).

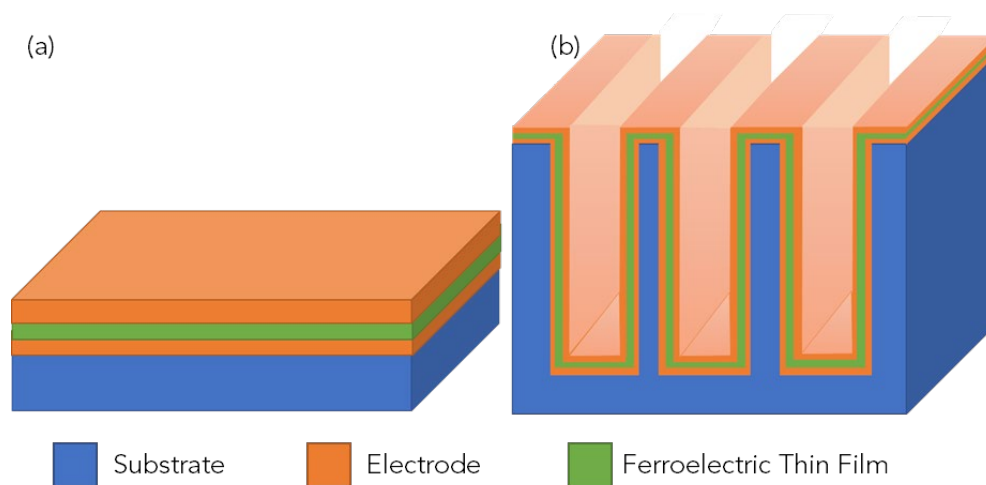


Figure 1.3. (a) Schematic of a classic 2D ferroelectric, (b) schematic of an example 3D ferroelectric.

Ferroelectric materials have recently started being deposited onto 3D structures, thus they are termed “3D ferroelectrics” (Figure 1.3b.). The ability to conformally coat simple 3D structures like trenches provides opportunity for increased capacitance in energy storage devices as well as vertical integration for dense memory devices. The increase in capacitance is due to the relationship capacitance has with surface area as given in Eq. (1 –6):

$$C = \epsilon_0 \epsilon_r \left( \frac{A}{t} \right) \quad (1 - 6)$$

Where  $C$  is capacitance,  $\epsilon_0$  is permittivity of a vacuum,  $\epsilon_r$  is relative dielectric permittivity of the material,  $A$  is surface area,  $t$  is thickness. Thus, as the surface area of a capacitor increases, so does its capacitance. Consequently, 3D structures like trenches increase the active device area without altering the footprint. Other 3D structures such as fins are often utilized as bulk acoustic resonators, specifically FinBARs<sup>38</sup>. As the ability to coat 3D structured substrates with ferroelectric thin films has only recently started developing, there are many more structures that could prove useful that have not yet been demonstrated. For example, it is possible to think of coating a 3D shape that could be used as a 3D pressure sensor with the ability to distinguish between forces applied from the top, bottom, left, or right. Another 3D structure could yield a 3D actuator, which could have significant implications in the world of microrobotics. As 3D ferroelectrics are further developed, many other not yet thought of applications will arise.

Initial attempts at creating a 3D ferroelectric were not very successful, as the deposition methods used, such as MOCVD, were not conducive to uniform coating of 3D structures. For example, initial attempts at putting PZT onto trenches via MOCVD resulted in a thin film with chemical inhomogeneity and high leakage current<sup>39,40</sup>. More recent work that has attempted to deposit PZT via MOCVD on trenches resulted in the thin film on the sidewalls being an undesirable pyrochlore phase rather than ferroelectric PZT<sup>41</sup>. It was not until ferroelectric thin

films were able to be produced readily via atomic layer deposition (ALD) that 3D ferroelectric thin films have become a viable option for future commercial applications.

### 1.2.1. Atomic Layer Deposition

The ability to produce ferroelectric thin films via ALD has been critical to production of 3D ferroelectric thin films. ALD offers the ability to conformally coat high aspect ratio structures, unlike many other deposition techniques such as sputtering, evaporation, chemical vapor deposition, pulsed laser deposition, etc. ALD is a thin-film deposition technique that produces films through sequential, self-limiting reactions, resulting in angstrom level control over film thicknesses, even over high aspect ratio structures. Typical ALD processes consist of two or more vapor-phase precursors that are never present simultaneously in the growth chamber. Instead, one precursor is flown into the chamber, followed by a purge gas, then a second precursor is flowed into the chamber, again followed by a purge step, see Figure 1.4.

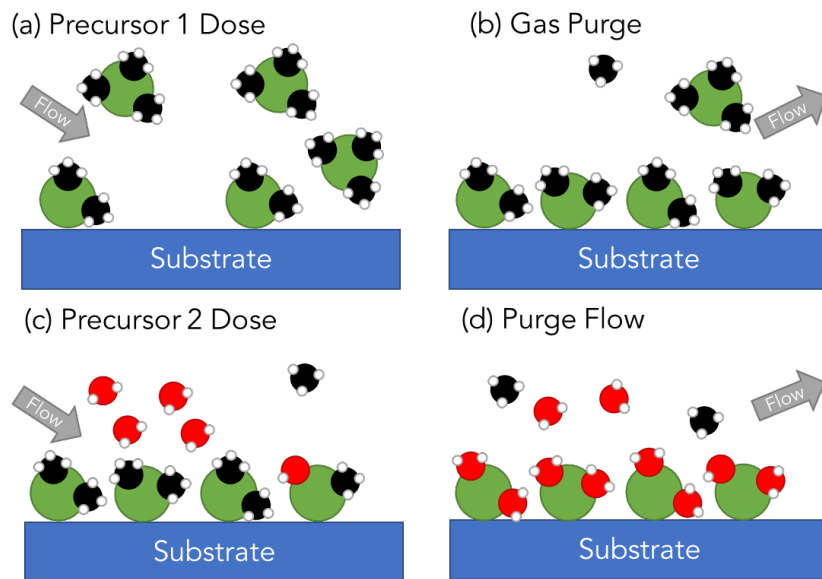


Figure 1.4. Dose Sequence of an ALD process.

The purpose of the purge step is to remove excess precursor gas that did not react with the surface from the chamber, as well as to remove the surface reaction byproducts from the growth

chamber. In an ideal ALD deposition, this results in the thin film being grown one monolayer at a time, enabling the coating of high aspect ratio structures. For example, the top of a trench will not become closed off with an excess of film growth before the bottom of the trench is coated.

### 1.2.2. Ferroelectric HfO<sub>2</sub>

Multiple ferroelectric materials have recently been demonstrated to be grown via ALD, such as PZT, PbHfO<sub>3</sub> (PHO), and PbHf<sub>x</sub>Ti<sub>1-x</sub>O<sub>3</sub> (PHT)<sup>42</sup>. However, to date, the materials that have had the most success in producing 3D ferroelectric thin films are HfO<sub>2</sub>-based. Bulk HfO<sub>2</sub> is not ferroelectric, thus it was a surprising and important discovery that, in 2011, Si:HfO<sub>2</sub> thin films were found to be ferroelectric<sup>43</sup>. HfO<sub>2</sub>-based thin films have quickly garnered the attention of the semiconductor industry because HfO<sub>2</sub> is compatible with current commercial production, as it is already used as a gate dielectric. HfO<sub>2</sub>-based thin films can either be ferroelectric or AFE-like, based on the dopant used in the thin film, as well as its concentration<sup>44</sup>. HfO<sub>2</sub>-based ferroelectric thin films also have the distinct advantage of demonstrating ferroelectricity at thicknesses as small as 1 nm<sup>45</sup>, unlike other ferroelectric thin films like PZT which lose their ferroelectric behavior at small length scales (<120 nm)<sup>46</sup>. Due to their simplistic fluorite structure, HfO<sub>2</sub>-based thin films are grown readily via ALD, and even deposited onto 3D structures, such as trenches. Polakowski *et al.* demonstrated Al:HfO<sub>2</sub> thin films on arrays with up to 100k trenches for non-volatile memory applications<sup>47</sup>. Si:HfO<sub>2</sub> thin films on trench structures were reported to have enhanced ESD values over their planar counterparts<sup>48</sup>. Si:HfO<sub>2</sub> on an area-enhanced substrate was shown to have a factor of 19 greater pyroelectric power output than its planar counterparts<sup>49</sup>. The application space for 3D ferroelectrics will only continue to grow as novel architectures are able to be coated with ferroelectric thin films grown via ALD.

### 1.2.3. Motivation for Continued Research Into 3D Ferroelectrics

In order for 3D ferroelectric thin films to reach their full potential, some critical questions must be addressed. First, how conformally can the ALD thin film be grown? Conformality of ALD growth varies with the reactivity of the precursor and the growth parameters, such as temperature, precursor purge times, purge gas chemistry and purity<sup>50</sup>. The reactivity of the precursor is one of the most influential parameters in determining the aspect ratio of structures that can be coated. For example, Al<sub>2</sub>O<sub>3</sub> thin films via ALD were demonstrated to coat structures with aspect ratios as high as 1:200<sup>51</sup>, while TiO<sub>2</sub> thin films via ALD were able to coat 1:120 structures<sup>51</sup>, and HfO<sub>2</sub> was demonstrated to only coat aspect ratios as high as 1:50<sup>52</sup>. The conformality of the thin film growth also depends on the complexity of the structure being coated, as a more complex structure will hinder the ability of the precursor gas to flow into the structure and the ability of the surface reactant byproducts to flow out. Thus, a trench with the same aspect ratio as a hole allows for more flow than the hole, and when considering even more complex structures, such as porous structures, the ability of the gases to flow within the structure becomes even more laborious<sup>53</sup>.

Second, for 3D ferroelectric thin films to be utilized, the difference between ferroelectric thin films deposited on vertical sidewalls and their lateral planar counterparts will need to be understood. Knowledge of the crystal structure of ferroelectric thin films deposited on sidewalls is currently lacking. Consider the use of a 3D ferroelectric thin film in a microactuator, where its piezoelectric response is key. Depending on the texture of the thin film, the piezoelectric response of the thin film will vary<sup>54</sup>. With ALD HfO<sub>2</sub>-based thin films, it is critical to form the orthorhombic polar phase if a ferroelectric response is desired<sup>55</sup>, while, for a ferroelectric response from ALD PbZr<sub>x</sub>Ti<sub>1-x</sub>O<sub>2</sub> thin films, it is critical to retain chemical homogeneity

throughout the film<sup>56</sup>. There has already been initial work that noted that the measured properties of 3D ferroelectrics were different from their expected properties. For example, Kühnel *et al.* deposited Si:HfO<sub>2</sub> over trenches and expected the area enhanced devices to have an ESD that was 19.5 times that of their planar counterparts due to surface area calculations from scanning electron microscopy (SEM) images<sup>48</sup>. However, the measured ESD of the area enhanced devices was only 11 times that of the planar devices<sup>48</sup>. Kühnel *et al.* theorized this could be due to inhomogeneity in dopant concentrations throughout the depth of the trenches<sup>48</sup>. Understanding if and why there are differences in planar vs. 3D devices in many other properties critical to device development, such as leakage current, loss tangent, and breakdown voltage will also accelerate the development of 3D ferroelectrics.

Third, a number of 3D ferroelectric applications rely on the piezoelectric properties of the material. To date, there has been limited, if any, research published on the piezoelectric response of ALD-grown ferroelectrics on released structures. Releasing piezoelectric thin films from their underlying substrate was reported to increase the piezoelectric response of those thin films<sup>57,58</sup>. Wallace *et al.* demonstrated an increase of 26% in the ferroelectric domain reorientation for a 75% de-clamped PZT thin film grown via chemical solution deposition<sup>57</sup>. Released 0.7Pb(Mg<sub>1/3</sub>Nb<sub>2/3</sub>)O<sub>3</sub>-0.3PbTiO<sub>3</sub> (PMN-PT) thin films have also been demonstrated to have a  $d_{33,f}$  three times as large as their unreleased counterparts<sup>58</sup>. As released structures become more common in resonator designs, understanding how the piezoelectric response of ALD grown ferroelectrics differs between released and unreleased structures will aid their development in RF application spaces.

### 1.3. Thesis Overview

In this dissertation, a simple, robust characterization platform for 3D ferroelectrics was designed and developed. The functionality of the characterization platform was demonstrated by depositing an AFE-like Al:HfO<sub>2</sub> thin film onto the platform and measuring the ESD, crystal structure, and piezoelectric response of the 3D ferroelectric thin film. The dissertation is organized as follows. Chapter 2 reviews prior research on HfO<sub>2</sub> based thin films, including the driving mechanisms for ferroelectricity and antiferroelectricity. In Chapter 2, the critical parameters for device creation are also introduced, along with typical values for HfO<sub>2</sub>-based ferroelectric thin films. In Chapter 3, the characterization structures on the platform are introduced, and the process flow for creating the structures is detailed. Additionally, Chapter 3 is also meant to serve as a how-to processing guide for anyone interested in producing this characterization platform in their own laboratories. Chapter 4 details the deposition parameters of the Al:HfO<sub>2</sub> thin films and the characterization of these thin films on planar substrates. In Chapter 5, the characterization of 3D Al:HfO<sub>2</sub> thin films is presented, as well as how the crystal structure, ESD, and ferroelectric response of the 3D devices compare to those of 2D counterparts. These differences are further analyzed and discussed. The displacement as a function of applied voltage of a cantilever is also measured, and from that the indirect transverse piezoelectric coefficient of the material is calculated. Finally, Chapter 6 concludes the dissertation by summarizing the results and looking to the future of how this 3D ferroelectric characterization platform could serve as a benchmarking substrate design.

## References

- 1 N. Setter, *Piezoelectric materials in devices : extended reviews on current and emerging piezoelectric materials technology, and applications*. (EPFL, Lausanne, 2003).
- 2 C. Kittel, *Phys. Rev.* **82** (5), 729 (1951).
- 3 Pierre Tolédano and Mael Guennou, *Phys. Rev. B* **94** (1), 014107 (2016).
- 4 E. Sawaguchi, H. Maniwa, and S. Hoshino, *Phys. Rev.* **83** (5), 1078 (1951).
- 5 R. W. Whatmore and A. M. Glazer, *Journal of Physics C: Solid State Physics* **12** (8), 1505 (1979).
- 6 J. Roos, R. Kind, and J. Petzelt, *Zeitschrift für Physik B Condensed Matter* **24** (1), 99 (1976).
- 7 J. Valasek, *Phys. Rev.* **17** (4), 475 (1921).
- 8 Etsuro Sawaguchi, *Journal of the Physical Society of Japan* **8** (5), 615 (1953).
- 9 Eugene Wainer, *Transactions of The Electrochemical Society* **89** (1), 331 (1946).
- 10 Charles Feldman, *Review of Scientific Instruments* **26** (5), 463 (1955).
- 11 B. H. Park, B. S. Kang, S. D. Bu, T. W. Noh, J. Lee, and W. Jo, *Nature* **401** (6754), 682 (1999).
- 12 M. J. Lancaster, J. Powell, and A. Porch, *Superconductor Science and Technology* **11** (11), 1323 (1998).
- 13 Brendan Hanrahan, Justin Easa, Alexis Payne, Yomery Espinal, S. Pamir Alpay, Haval Kareem, Casey O'Brien, and Andrew Smith, *Cell Reports Physical Science* **1** (6), 100075 (2020).
- 14 Dennis L. Polla, *Microelectronic Engineering* **29** (1), 51 (1995).
- 15 N. Setter, D. Damjanovic, L. Eng, G. Fox, S. Gevorgian, S. Hong, A. Kingon, H. Kohlstedt, N. Y. Park, G. B. Stephenson, I. Stolitchnov, A. K. TagansteV, D. V. Taylor, T. Yamada, and S. Streiffer, *Journal of Applied Physics* **100** (5), 051606 (2006).
- 16 M. Trentzsch, S. Flachowsky, R. Richter, J. Paul, B. Reimer, D. Utess, S. Jansen, H. Mulaosmanovic, S. Müller, S. Slesazeck, J. Ocker, M. Noack, J. Müller, P. Polakowski, J. Schreiter, S. Beyer, T. Mikolajick, and B. Rice, presented at the 2016 IEEE International Electron Devices Meeting (IEDM), 2016 (unpublished).
- 17 Masanori Okuyama, Hiroyuki Seto, Motohiro Kojima, Yasushi Matsui, and Yoshihiro Hamakawa, *Jpn. J. Appl. Phys.* **21** (S1), 225 (1982).
- 18 Paul Muralt, *Rep. Prog. Phys.* **64** (10), 1339 (2001).
- 19 Shishir Pandya, Gabriel Velarde, Lei Zhang, Joshua D. Wilbur, Andrew Smith, Brendan Hanrahan, Chris Dames, and Lane W. Martin, *NPG Asia Materials* **11** (1), 26 (2019).
- 20 Brendan Hanrahan, Cameron Neville, Andrew Smith, Nikolay Ter-Gabrielyan, Nicholas Jankowski, and Chris Mike Waits, *Advanced Materials Technologies* **1** (9), 1600178 (2016).
- 21 Tadashi Shiosaki and Akira Kawabata, *Ferroelectrics* **42** (1), 219 (1982).
- 22 H. P. Lobl, M. Klee, C. Metzmacher, W. Brand, R. Milsom, P. Lok, and F. van Straten, presented at the 2001 IEEE Ultrasonics Symposium. Proceedings. An International Symposium (Cat. No.01CH37263), 2001 (unpublished).
- 23 M. Y. Elsayed, P. Cicek, F. Nabki, and M. N. El-Gamal, *Journal of Microelectromechanical Systems* **25** (2), 252 (2016).
- 24 Yoshio Satoh, Tokihiro Nishihara, Tsuyoshi Yokoyama, Masanori Ueda, and Tsutomu Miyashita, *Jpn. J. Appl. Phys.* **44** (5A), 2883 (2005).

25 Qingming Chen and Qing-Ming Wang, *Applied Physics Letters* **86** (2), 022904 (2005).  
26 Fabian T. Goericke, Gabriele Vigevani, Igor I. Izyumin, Bernhard E. Boser, and Albert P.  
Pisano, presented at the IEEE International Ultrasonics Symposium, Dreseden, Germany,  
27 2012 (unpublished).  
J. M. Puder, I. Kierzewski, V. F. Tseng, R. R. Knight, J. S. Pulskamp, and J. L. Martin,  
presented at the 2019 IEEE International Symposium on Inertial Sensors and Systems  
(INERTIAL), 2019 (unpublished).  
28 F. Kurokawa, Y. Oochi, A. Sadanda, Y. Tsujiura, H. Hida, and I. Kanno, presented at the  
2015 Transducers - 2015 18th International Conference on Solid-State Sensors, Actuators  
and Microsystems (TRANSDUCERS), 2015 (unpublished).  
29 Asif Khan, Zafar Abas, Heung Soo Kim, and Il-Kwon Oh, *Smart Materials and*  
*Structures* **25** (5), 053002 (2016).  
30 Ning Chen and Chuan Tian, *Sensors and Actuators A: Physical* **323**, 112660 (2021).  
31 C.H. Rhee, Pulskamp, J.S., Polcawich, R.G., Oldham, K.R., *Journal of*  
*Microelectromechanical Systems* **21** (6) (2012).  
32 Jongsoo Choi, Minchul Shin, Ryan Q. Rudy, Christopher Kao, Jeffrey S. Pulskamp,  
Ronald G. Polcawich, and Kenn R. Oldham, *International Journal of Intelligent Robotics*  
*and Applications* **1** (2), 180 (2017).  
33 Gabriel L. Smith, Jeffrey S. Pulskamp, Luz M. Sanchez, Daniel M. Potrepka, Robert M.  
Proie, Tony G. Ivanov, Ryan Q. Rudy, William D. Nothwang, Sarah S. Bedair,  
Christopher D. Meyer, and Ronald G. Polcawich, **95** (6), 1777 (2012).  
34 B. Jaffe, *Proceedings of the IRE* **49** (8), 1264 (1961).  
35 I. Burn and D. M. Smyth, **7**, 339 (1972).  
36 in *Radio and Electronics Cookbook*, edited by George Brown (Newnes, Oxford, 2001),  
pp. 34.  
37 S. S. N. Bharadwaja and S. B. Krupanidhi, *Journal of Applied Physics* **89** (8), 4541  
(2001).  
38 M. Ramezani, M. Ghatge, V. Felmetger, and R. Tabrizian, presented at the 2019 IEEE  
MTT-S International Microwave Symposium (IMS), 2019 (unpublished).  
39 Chia-Pin Yeh, Marco Lisker, Bodo Kalkofen, and Edmund P. Burte, *AIP Advances* **6**  
(3), 035128 (2016).  
40 Youngsoo Park, Jung Hyun Lee, June Mo Koo, Suk Pil Kim, Sangmin Shin, Choong Rae  
Cho, and June Key Lee, *Integrated Ferroelectrics* **66** (1), 85 (2004).  
41 Sangmin Shin, Hee Han, Yong Jun Park, Jae-Young Choi, Youngsoo Park, and Sunggi  
Baik, *AIP Conference Proceedings* **879** (1), 1554 (2007).  
42 Nicholas A. Strnad, Brendan M. Hanrahan, Daniel M. Potrepka, Jeffrey S. Pulskamp,  
Raymond J. Phaneuf, and Ronald G. Polcawich, *Journal of the American Ceramic*  
*Society* **104** (3), 1216 (2021).  
43 T. S. Böscke, J. Müller, D. Bräuhäus, U. Schröder, and U. Böttger, *Applied Physics*  
*Letters* **99** (10), 102903 (2011).  
44 Min Hyuk Park, Young Hwan Lee, Han Joon Kim, Yu Jin Kim, Taehwan Moon, Keum  
Do Kim, Johannes Müller, Alfred Kersch, Uwe Schroeder, Thomas Mikolajick, and  
Cheol Seong Hwang, *Advanced Materials* **27** (11), 1811 (2015).  
45 Suraj S. Cheema, Daewoong Kwon, Nirmaan Shanker, Roberto dos Reis, Shang-Lin Hsu,  
Jun Xiao, Haigang Zhang, Ryan Wagner, Adhiraj Datar, Margaret R. McCarter, Claudy  
R. Serrao, Ajay K. Yadav, Golnaz Karbasian, Cheng-Hsiang Hsu, Ava J. Tan, Li-Chen

46 Wang, Vishal Thakare, Xiang Zhang, Apurva Mehta, Evguenia Karapetrova, Rajesh V.  
Chopdekar, Padraic Shafer, Elke Arenholz, Chenming Hu, Roger Proksch, Ramamoorthy  
Ramesh, Jim Ciston, and Sayeef Salahuddin, *Nature* **580** (7804), 478 (2020).

47 Yaser Bastani, Thorsten Schmitz-Kempen, Andreas Roelofs, and Nazanin Bassiri-Gharb,  
*Journal of Applied Physics* **109** (1), 014115 (2011).

48 P. Polakowski, S. Riedel, W. Weinreich, M. Rudolf, J. Sundqvist, K. Seidel, and J.  
Muller, presented at the IEEE 6th International Memory Workshop (IMW), Taipei, 2014  
(unpublished).

49 Kati Kühnel, Malte Czernohorsky, Clemens Mart, and Wenke Weinreich, *Journal of  
Vacuum Science & Technology B* **37** (2), 021401 (2019).

50 Brendan Hanrahan, Clemens Mart, Thomas Kämpfe, Malte Czernohorsky, Wenke  
Weinreich, and Andrew Smith, *Energy Technology* **7** (10), 1900515 (2019).

51 Jihong Yim, Oili M. E. Ylivaara, Markku Ylilampi, Virpi Korpelainen, Eero Haimi,  
Emma Verkama, Mikko Utriainen, and Riikka L. Puurunen, *Phys. Chem. Chem. Phys.*  
**22** (40), 23107 (2020).

52 R. L. Puurunen and F. Gao, presented at the 2016 14th International Baltic Conference on  
Atomic Layer Deposition (BALD), 2016 (unpublished).

53 Alireza M. Kia, Nora Haufe, Sajjad Esmaeili, Clemens Mart, Mikko Utriainen, Riikka L.  
Puurunen, and Wenke Weinreich, *Nanomaterials (Basel)* **9** (7), 1035 (2019).

54 Véronique Cremers, Riikka L. Puurunen, and Jolien Dendooven, *Applied Physics  
Reviews* **6** (2), 021302 (2019).

55 Zhen Zhou, Su-Wei Zhang, Yao Zhang, Jin Luo, Wei Sun, Xuping Wang, and Jing-Feng  
Li, *Advanced Electronic Materials* **4** (11), 1800351 (2018).

56 Stefan Mueller, Johannes Mueller, Aarti Singh, Stefan Riedel, Jonas Sundqvist, Uwe  
Schroeder, and Thomas Mikolajick, *Advanced Functional Materials* **22** (11), 2412  
(2012).

57 Nicholas Anthony Strnad, University of Maryland, 2019.

58 M. Wallace, R. L. Johnson-Wilke, G. Esteves, C. M. Fancher, R. H. T. Wilke, J. L. Jones,  
and S. Trolrier-McKinstry, *Journal of Applied Physics* **117** (5), 054103 (2015).

Ryan Keech, Linghan Ye, James L. Bosse, Giovanni Esteves, Jonathon Guerrier, Jacob  
L. Jones, Marcelo A. Kuroda, Bryan D. Huey, and Susan Trolrier-McKinstry, *Advanced  
Functional Materials* **27** (9), 1605014 (2017).

## Chapter 2. Literature Review of Ferroelectric HfO<sub>2</sub> Thin Films

### 2.1. Origin of Ferroelectricity in HfO<sub>2</sub>

Since the discovery of ferroelectricity in HfO<sub>2</sub> thin films a decade ago<sup>1</sup>, the ferroelectric phase has been determined to be the non-centrosymmetric polar orthorhombic III phase (o-phase,  $Pca2_1$ )<sup>2</sup>. This phase is not present in bulk HfO<sub>2</sub>, which has a cubic phase (c-phase,  $Fm3m$ ) at high temperature and low pressure and when cooled, transitions to a tetragonal phase (t-phase,  $P4_2/nmc$ ) followed by a monoclinic phase (m-phase,  $P2_1/c$ ) as shown in Figure 2.1<sup>3</sup>. However, computational *ab initio* electronic structure calculations<sup>4</sup> and first principle calculations<sup>5</sup> have determined that the o-phase can be stabilized over the more energetically favorable t-phase or m-phase under a certain range of compressive pressures and temperatures. Experimentally, the o-phase has been stabilized in HfO<sub>2</sub>-based thin films through the use of dopants<sup>6</sup>, stress<sup>7</sup>,

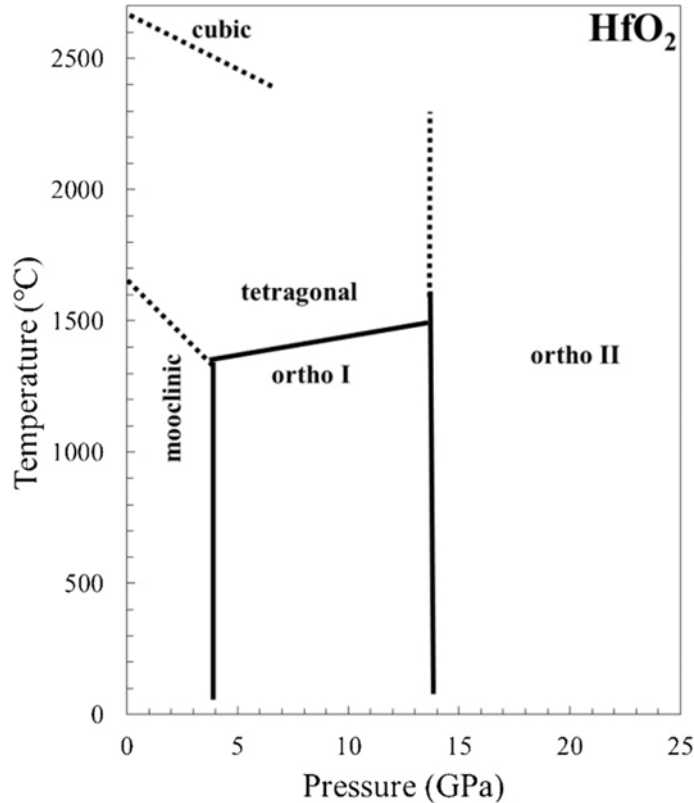


Figure 2.1. Pressure – temperature phase diagram for bulk HfO<sub>2</sub> with the dotted lines representing assumed boundaries.<sup>3</sup>

surface/interface/grain boundary energy<sup>8,9</sup>, defects such as oxygen vacancies<sup>10,11</sup>, or electric field<sup>12</sup>. In reality, the o-phase is stabilized by a combination of these mechanisms<sup>13</sup>.

### 2.1.1. Ferroelectric Response Impact Factors

As previously stated, ferroelectricity was first discovered in Si:HfO<sub>2</sub>, thus dopants were among the first mechanisms explored for stabilizing the o-phase in HfO<sub>2</sub>-based thin films<sup>1</sup>.

Dopants alone cannot induce ferroelectricity in HfO<sub>2</sub>, rather the combination of a dopant plus another mechanism such as stress is required to induce ferroelectricity<sup>14,15</sup>. As much as dopants are not a solo mechanism for ferroelectricity, they do play a significant role in determining the ferroelectric response of HfO<sub>2</sub>-based thin films. Dopants that have been reported in ferroelectric HfO<sub>2</sub>-based thin films are Si<sup>1</sup>, Zr<sup>16</sup>, Al<sup>2</sup>, Gd<sup>17</sup>, Y<sup>18</sup>, La<sup>19</sup>, and Sr<sup>20</sup>. Determining the role dopants play in stabilizing the o-phase has been the focus of a few computational studies<sup>11,14,15</sup>. Batra *et*

*al.* observed dopants that form an additional bond between the dopant cation and their second-nearest oxygen neighbor significantly lower the formation energy for the o-phase<sup>14</sup>. The shorter the bond length is, the lower the formation energy for the o-phase becomes<sup>14</sup>. Thus, *Batra et al.* concluded that dopants with higher ionic radius and lower electronegativity were found to help stabilize the o-phase more efficiently<sup>14</sup>. Another computational study by *Lee et al.* determined that dopants smaller than Hf stabilized the t-phase over the c-phase, while in thin films where the dopant was larger than Hf the opposite was true, with the c-phase stabilized over the t-phase<sup>11</sup>. This result helps explain the empirical observation that dopants smaller than Hf like Al, Zr, and Si, can induce an AFE-like response in HfO<sub>2</sub>-based thin films, while dopants with larger radii than Hf only appear to induce a ferroelectric response<sup>21</sup>.

Another mechanism shown to help stabilize the ferroelectric o-phase in HfO<sub>2</sub>-based thin films is defects. Dopants themselves along with the oxygen vacancies that naturally arise during fabrication and annealing for charge neutrality are considered point defects. *Zhou et al.* in a computational study demonstrated that an increase in oxygen vacancies lowers the formation energy for the o-phase, resulting in the o-phase having a lower formation energy than both the t-phase and the c-phase<sup>22</sup>. An experimental study by *Pal et al.* confirmed this effect by demonstrating that a decrease in ozone dosage time in an ALD growth of undoped HfO<sub>2</sub> thin films increased  $P_r$ .<sup>10</sup> The increase in  $P_r$  was attributed to an increase in o-phase upon annealing, *Pal et al.* theorized the o-phase formation was aided by the increased presence of oxygen vacancies. Another study demonstrated the effects other defects, such as carbon impurities, have on the microstructure of undoped HfO<sub>2</sub> thin films upon annealing<sup>23</sup>. *Kim et al.* demonstrated undoped HfO<sub>2</sub> thin films deposited at lower temperatures had larger  $P_r$  values which was

attributed to smaller grains being formed as a result of carbon impurities<sup>23</sup>. This is a prime example of how many of these stabilization mechanisms for the o-phase are interconnected.

Stress, surface energy, interface energy, and grain boundary energy have all been attributed to stabilization of the o-phase in HfO<sub>2</sub>-based thin films<sup>7,8,23-26</sup>. Materlik *et al.* used first principle calculations to demonstrate that increased in-plane strain in HfO<sub>2</sub> can allow the o-phase to form because the stress decreases the o-phase formation energy<sup>8</sup>. The stress state of a HfO<sub>2</sub>-based thin film can be influenced by process parameters such as growth temperature<sup>23</sup>, annealing temperature<sup>24</sup>, and annealing time<sup>25</sup> as well as the choice of electrode<sup>26</sup> and substrate<sup>7</sup> used. For example, Lee *et al.* demonstrated the effects of using different electrode materials on the ferroelectric properties of Hf<sub>0.5</sub>Zr<sub>0.5</sub>O<sub>2</sub> (HZO) thin films<sup>26</sup>. The authors produced HZO samples with TiN bottom electrodes and TiN, Mo, W or Ni top electrodes as well as samples with TiN top electrodes and TiN, Mo, W, or Ni bottom electrodes<sup>26</sup>. The authors discovered that the coefficient of thermal expansion of the top and bottom electrode changed the amount of tensile strain induced in HZO thin films<sup>26</sup>. The lower the coefficient of thermal expansion, the higher the  $P_r$ , which was attributed to an increase in the amount of o-phase being formed<sup>26</sup>. Lee *et al.* also noted that the bottom electrode played a much larger role in influencing the ferroelectric properties over the top electrode, both with how it influences the mechanical stress in the film and with the formation of an interfacial dead layer<sup>26</sup>. Different bottom electrodes produced different interfacial dead layer thicknesses. A dead layer is an interfacial layer between the ferroelectric thin film and the electrode that is not ferroelectric. Studies have also been conducted on the effects that variations in processing parameters have on HfO<sub>2</sub>-based thin films. Müller *et al.* reported that the ferroelectric response increased in HfO<sub>2</sub>-based thin films when the films were annealed after a top electrode had been deposited versus prior to a top electrode being

deposited<sup>18</sup>. This again is a result of a higher tensile strain state favoring the formation of more o-phase<sup>18</sup>. Another factor in determining the stress state of a HfO<sub>2</sub>-based thin film is the thickness of the thin film and subsequent grain size distribution. The grain size distribution is critical in determining the interface/grain boundary energy present in the thin film, with larger grains having lower grain boundary energy than smaller grains<sup>1,7,24,27</sup>. Materlik *et al.* presented a first principles study demonstrating that surface energy of grains in HZO thin films as a key component to the stabilization of the o-phase<sup>8</sup>. Park *et al.* further demonstrated that 29.2 nm thick ALD grown HZO thin films had larger grains and had reduced polarization values compared to their counterparts that were 9.2 nm thick and had smaller grains<sup>9</sup>.

Electric field is another mechanism that has been shown to stabilize the o-phase in HfO<sub>2</sub>-based thin films. This is most apparent in the phenomenon known as the ‘wake-up’ effect<sup>12,28-30</sup>. Wake-up is the phenomena where an initially pinched hysteresis loops with zero or near zero  $P_r$  has an increase in  $P_r$  during electric field cycling<sup>28</sup>. One predominate theory for the initial pinched hysteresis loop and following wake-up in HfO<sub>2</sub>-based thin films is that charge defects present in the thin film pin domains preventing a large  $P_r$  to be reached initially, however, these defects move with the cyclic application of an electric field allowing for the ferroelectric domains to become unpinned<sup>12,28,31</sup>. A schematic of the role of defects in pinning domains and subsequent release of pinned domains with electric field cycling is shown in Figure 2.2<sup>30</sup>.

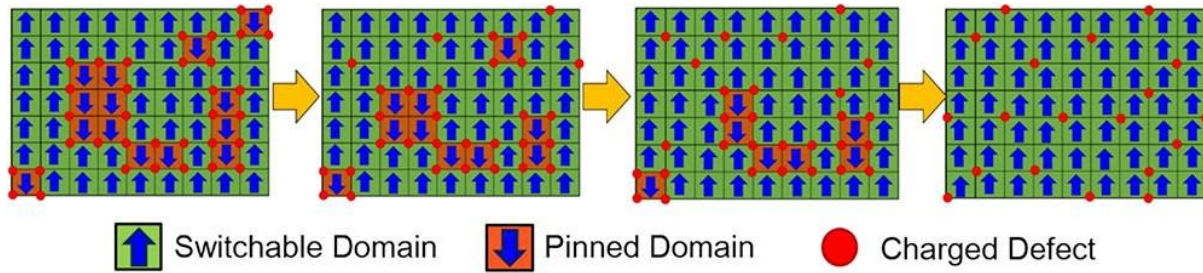


Figure 2.2. A schematic illustrating how charged defects can pin domains, but as they move the pinned domains become unpinned.<sup>30</sup> Reprinted (adapted) with permission from Patrick D. Lomenzo, Claudia Richter, Thomas Mikolajick, and Uwe Schroeder, Depolarization as Driving Force in Antiferroelectric Hafnia and Ferroelectric Wake-Up, *ACS Applied Electronic Materials* **2** (6), 1583 (2020). Copyright 2020 American Chemical Society.

These charge defects could be oxygen vacancies, as oxygen vacancies have been demonstrated to be produced during electric field cycling in undoped  $\text{HfO}_2$  thin films<sup>32</sup>. Schenk *et al.* were able to model the wake-up effect seen in  $\text{Si:HfO}_2$  thin films through the movement of oxygen vacancies<sup>12</sup>. In  $\text{Y:HfO}_2$  thin films, the wake-up effect was shown to be temperature dependent, with higher temperatures resulting in larger rates of increase in  $P_r$  per electric field cycle ( $dP_r/dN$ )<sup>33</sup>. This increase in  $dP_r/dN$  suggested that the mechanism of wake-up was temperature dependent in the form of mobile charged defects, such as oxygen vacancies<sup>33</sup>. Another defect mechanism that has been reported as a possible driver for wake-up is the charge trapping or the injection of screening charges from the electrodes<sup>30</sup>. For example,  $\text{HfO}_2$ -based thin films TiN and TaN bottom electrode interfaces are believed to oxidize during thin film deposition, while the TiN or TaN top electrodes do not oxidize after sputtering and after annealing act as oxygen scavengers from the ferroelectric thin film<sup>30,31</sup>. Other work has attributed wake-up to an electric field driven phase transformation from either m-phase to o-phase<sup>29</sup>, or t-phase to o-phase<sup>16,34</sup>. Wake-up has also been theorized to be caused by the ferroelastic realignment of ferroelectric dipoles towards the out-of-plane direction<sup>30,35-37</sup>. This has been confirmed as a plausible

explanation through the use of X-ray diffraction (XRD) in epitaxial grown Y:HfO<sub>2</sub><sup>35</sup>, and via scattering Kikuchi patterns in HZO thin films<sup>36</sup>.

### 2.1.2. Driving mechanisms for AFE-like Response

However, there are AFE-like HfO<sub>2</sub>-based thin films that maintain low  $P_r$  even with electric field cycling. As mentioned previously, HfO<sub>2</sub>-based thin films with dopants smaller than Hf can be AFE-like<sup>21</sup>. The reason for the “AFE-like” nomenclature in this work is the current lack of consensus of the physical origins of the hysteresis “double loop” characteristic of AFEs<sup>8,16,28,31,38,39</sup>. Many of the same theories for why there is an initial low  $P_r$  for samples that experience wake-up, have been attributed for the reason for the stable AFE-like response in HfO<sub>2</sub>-based thin films. The most prevalent theory is a reversible field induced phase transition from the t-phase to the o-phase causes the AFE-like behavior<sup>16</sup>. This has been computationally confirmed to be a plausible explanation as the activation energy between the t-phase and o-phase has been calculated at 35 meV per formula unit<sup>40</sup>. This transition would require the long axis of the t-phase, the  $c$ -axis, to transition to the longest axis of the o-phase, which is the  $a$ -axis<sup>27</sup>, as shown in Figure 2.3<sup>41</sup>. The polarization axis of the o-phase is the  $c$ -axis. Similar to wake-up,

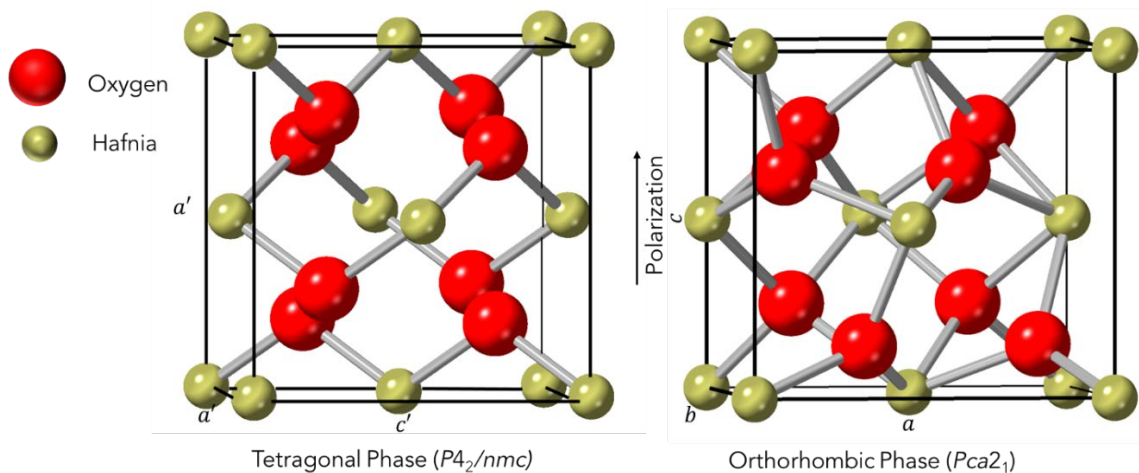


Figure 2.3. Schematic of the t-phase,  $P4_2/nmc$ , crystal structure with the  $a$ -axis along the [110] for HfO<sub>2</sub> and the o-phase,  $Pca2_1$ , crystal structure for HfO<sub>2</sub><sup>41</sup>.

interfacial charged defects have also been attributed to be the mechanism driving a stable AFE-like response, as they act as permanent pinning sites for domain wall motion inhibiting the total switchable polarization of the thin film<sup>28,31,39</sup>. Another theory for the double hysteresis/AFE-like response of Hf-based thin films is an alternate polar phase<sup>42</sup>. It has also been suggested that there is no reason the  $Pca2_1$  could not exist in an antipolar state, with ferroelectric domains oriented in antiparallel<sup>8</sup>. In terms of ESD, the low or zero remanent polarization observed in these films, regardless of physical origin, is beneficial. Energy is stored when either the material is transitioning from ferroelectric to AFE or pinning caused by charged defects is overcome.

## **2.2. Critical Parameters for Device Creation**

Prior measurements of ferroelectric HfO<sub>2</sub>-based thin films primarily focused on their  $P_r$  values for memory applications and in AFE-like thin films their ESD values for energy storage applications. However, other values critical to device development are loss tangent, leakage current, relative dielectric permittivity, breakdown and operating voltage, and reliability metrics, and these parameters are significantly underreported in comparison.

### **2.2.1. Rated Capacitance, Rated Voltage, and Breakdown Voltage**

Device specifications listed for every commercial capacitor are its rated voltage ( $V_R$ ) and its rated capacitance ( $C_R$ ). The rated capacitance is typically measured at 25 °C for commercial devices, however, the frequency and voltage at which it is measured varies from device to device and manufacturer to manufacturer. The rated voltage of a device is its operating voltage ( $V_{op}$ ), which is typically 4 to 5 times below that of the breakdown voltage ( $V_{BD}$ ) of the device. The breakdown voltage of the device is the voltage at which the material is no longer electrically insulating. For multilayer ceramic capacitors their rated voltage can be 10 times lower than their  $V_{BD}$ <sup>43</sup>, and tantalum capacitors have been tested up to 132% of their rated voltage<sup>44</sup>. These values

should be kept in mind when conducting reliability measurements on HfO<sub>2</sub>-based devices, such as when conducting endurance cycling measurements at the theoretical operating voltage and by reporting relative permittivity and capacitance values vs. electric field.

### 2.2.2. Relative Dielectric Permittivity

The relative permittivity of a material, also known as the dielectric constant of a material, is a measure of how well a material stores charge and is a determining factor in the capacitance of a device as noted previously in section 1.2. Several publications have given permittivity vs. electric field plots for HfO<sub>2</sub>-based thin films which show a wide spread of reported values from 20-50<sup>18,31</sup>. This spread has been attributed to most HfO<sub>2</sub>-based thin films being multiphase, containing o-phase, t-phase, and m-phase together<sup>1,21,45</sup>. Materlik calculated the orientationally averaged relative dielectric permittivities from first principles as 22.4, 45.9, 27.0, or 36.0 the m-phase, t-phase, o-phase, and c-phase respectively for HfO<sub>2</sub><sup>46</sup>. Thus, the variability in relative permittivity values can be attributed in part to the multiple phases often present. Since dopant and dopant concentration play a role in determining the phase composition of a HfO<sub>2</sub>-based thin film as previously noted<sup>11,14,45</sup>, dopants also play a role in determining the relative dielectric permittivity. Thus, just as smaller dopants have been noted for their stabilization of the t-phase over the c-phase, HfO<sub>2</sub>-based thin films with smaller dopants often have larger relative permittivity values thought to be due to higher t-phase fractions as compared with HfO<sub>2</sub>-based thin films with larger dopants<sup>8</sup>. For example, ferroelectric 2 mol% Y:HfO<sub>2</sub> showed a permittivity value of ~20<sup>18</sup>, while 8.5 mol% Al:HfO<sub>2</sub> thin films with TiN electrodes had measured permittivity values of 35<sup>2</sup>.

### 2.2.3. Piezoelectric Coefficient

Besides the relative dielectric permittivity, there is also the piezoelectric constant, an important metric for piezoMEMS applications. The piezoelectric response of ferroelectric HfO<sub>2</sub> was first measured using piezoresponse force microscopy (PFM) with the discovery it was ferroelectric in 2011 using double beam laser interferometry (DBLI)<sup>1</sup>. Another PFM study on Si:HfO<sub>2</sub> thin films gave further evidence to suggest the origin of the ferroelectric response was due to the o-phase<sup>47</sup>. Kirbach *et al.* measured the piezoelectric response of a 50 nm Si:HfO<sub>2</sub> thin film using DBLI and calculated a piezoelectric constant,  $d_{33,f}$  of 20 pm/V, which decreased after the thin film experienced wake-up after 10<sup>4</sup> cycles<sup>48</sup>. DBLI was also used to measure the  $d_{33,f}$  of AFE-like Si:HfO<sub>2</sub> thin films at 14.6 pm/V, and these films maintained this value even after 160k cycles<sup>37</sup>. Another report calculated the  $d_{31}$  for Si:HfO<sub>2</sub> by rapidly thermally cycling the thin film, the value for  $d_{31}$  was reported at -11.5 pm/V<sup>49</sup>. These studies are among the few that have reported piezoelectric coefficients for a HfO<sub>2</sub>-based thin films, however to date, none of these studies have reported a piezoelectric coefficient from a measurement of a released structure such as a cantilever beam for a ferroelectric HfO<sub>2</sub>-based thin film. Released PZT thin films have been demonstrated to have enhanced piezoelectric response over their clamped counterparts<sup>50</sup>. Hsain *et al.* also demonstrated enhanced piezoelectric response in HZO thin films on flexible substrates<sup>51</sup>. The enhanced piezoelectric response was conjectured to be due to domain wall motion becoming easier on the flexible substrates as compared with their rigid substrate counterparts<sup>51</sup>.

### 2.2.4. Leakage Current Density

Another critical parameter often underreported for HfO<sub>2</sub>-based thin films is the dielectric loss of the material. Even if a material has extremely high polarization values if it suffers from

high dielectric loss it will never become widely used. The first type of loss is conduction loss, which is the flow of charge through a dielectric when a DC voltage is applied, this loss is defined as the leakage current density of the device. Leakage current density is measured by applying a voltage for a set period of time often called the soak period, this allows for the sample to reach a steady state after the initial application of voltage. After this soak period is over, the current through the sample is measured, this is the leakage current. This parameter is often found on capacitor specification sheets listed as the DC Leakage, or DCL<sup>52</sup>. On specification sheets, it is given in terms of the product of the rated voltage and the rated capacitance,  $C_R \cdot V_R$ . For example a DCL of 0.01CV listed on a specification sheet for a 100  $\mu\text{F}/10\text{ V}$  rated device, would have a DCL of 10  $\mu\text{A}$ <sup>53</sup>. However, the leakage current density values reported in literature are often leakage current density vs. voltage plots<sup>23,25,54</sup>. The leakage current density of some HfO<sub>2</sub>-based thin films has been reported, however, it varies significantly with processing. Kim *et al.* reported variation in leakage current density in undoped ferroelectric HfO<sub>2</sub> thin films from a variation in deposition temperature<sup>23</sup>. The authors reported an increase in leakage current with a decrease in deposition temperature due to increased carbon<sup>23</sup>. With leakage current densities of  $10^{-4}\text{ A/cm}^2$  reported for samples with increased carbon impurities as compared to  $10^{-7}\text{ A/cm}^2$  for samples with lower carbon impurities<sup>23</sup>. Another process parameter demonstrated to affect leakage current density is annealing temperature, Park *et al.* demonstrated an increase in leakage current density with an increase in annealing temperature as shown in Figure 2.4<sup>24</sup>. The authors surmised that the increase in leakage current density was most likely due to an increase in grain size in the thin films<sup>24</sup>. However, not all variations in processing conditions result in changes in leakage current density. For example, it was demonstrated that an annealing atmosphere of N<sub>2</sub>, O<sub>2</sub>, or forming gas did not significantly alter the P-E curves of the HZO films nor the leakage current

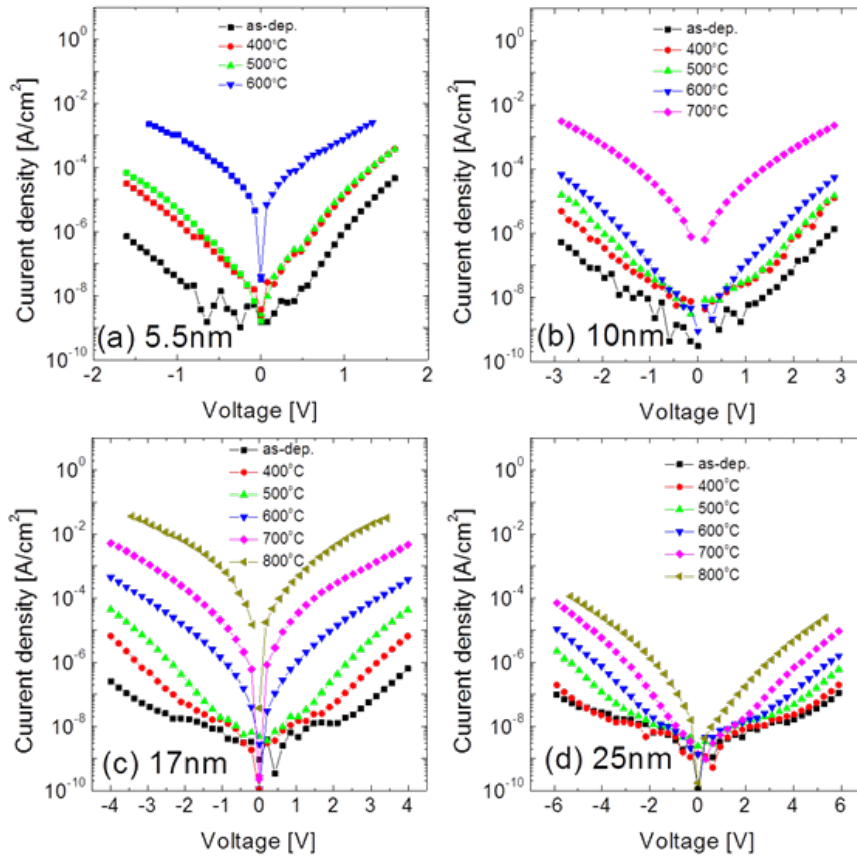


Figure 2.4. Leakage current density vs. voltage plots for (a) 5.5-, (b) 10-, (c) 17-, and (d) 25-nm-thick  $\text{Hf}_{0.5}\text{Zr}_{0.5}\text{O}_2$  thin films with annealing temperature of 400-800 °C, respectively.<sup>24</sup> Reprinted from [Min Hyuk Park, Han Joon Kim, Yu Jin Kim, Woongkyu Lee, Taehwan Moon, and Cheol Seong Hwang, Evolution of phases and ferroelectric properties of thin  $\text{Hf}_{0.5}\text{Zr}_{0.5}\text{O}_2$  films according to the thickness and annealing temperature, Applied Physics Letters **102** (24), 242905 (2013)], with the permission of AIP Publishing.

density of  $3 \times 10^{-7} \text{ A/cm}^2$ <sup>54</sup>. Also Park *et al.* demonstrated that HZO thin films with various Zr concentrations had similar leakage current densities to one another at  $10^{-3} \text{ A/cm}^2$ <sup>55</sup>.

### 2.2.5. Loss Tangent

The other loss parameter is the loss tangent, which is a measure of AC losses in a material due to the movement or rotation of atom or molecules. Mathematically, the loss tangent is defined as the ratio between the resistance of the capacitor and the reactance of the capacitor, or the reactive and resistance components of its permittivity as given in Eq. (2 – 1):

$$\tan \delta = \frac{\varepsilon''}{\varepsilon'} \quad (2 - 1)$$

Where  $\tan \delta$  is the loss tangent,  $\varepsilon''$  is the imaginary component of the complex permittivity, and  $\varepsilon'$  is the real component of the complex permittivity. On commercial specification sheets, the parameter often listed is the dissipation factor (DF), which is simply the loss tangent expressed as a percentage<sup>53</sup>. The loss tangent of a device can be dependent on frequency, at high frequencies it is governed by how well a material dissipates heat, while at low frequencies it is governed predominately by the dielectric strength of the material<sup>56</sup>. One of the only studies to date to publish this value for HfO<sub>2</sub>-based thin films focused on understanding the wave propagation constant of HZO in the frequency range 1-14 GHz<sup>57</sup>. To the best of the author's knowledge, prior to the work produced in this dissertation, there have been no other reported loss tangent values for ferroelectric HfO<sub>2</sub>-based thin films.

### **2.2.6. Electrical Characteristics vs. Temperature and Frequency**

Understanding how the electrical characteristics of HfO<sub>2</sub>-based thin films change in various temperatures is critical to the development of commercial devices using this material. This is especially true of electronics used for the military, which are required to be capable of operating within military specification temperatures (-55 °C to 125 °C). Müller *et al.* conducted P-E loop measurements and calculated the relative dielectric permittivity of HZO thin films with varying ZrO<sub>2</sub> concentrations, and demonstrated the higher the ZrO<sub>2</sub> content the less temperature dependence the thin films had, this is shown in Figure 2.5<sup>16</sup>. Other work has demonstrated ferroelectric Si:HfO<sub>2</sub> thin films have decreasing  $P_r$  values with increasing temperature, which was confirmed to be due to an increase in the o-phase fraction of the thin films with decreasing temperature via analysis of grazing incident x-ray diffraction (GIXRD) patterns of the thin films<sup>58</sup>. For AFE-like HfO<sub>2</sub>-based thin films, a few studies have focused on demonstrating the

temperature stability of ESD values. Lomenzo *et al.* demonstrated 4 at% Si:Hf<sub>0.5</sub>Zr<sub>0.5</sub>O<sub>2</sub> and 4 at% Al:Hf<sub>0.5</sub>Zr<sub>0.5</sub>O<sub>2</sub> with TiN electrodes maintained energy storage density (ESD) values of  $\approx 45$

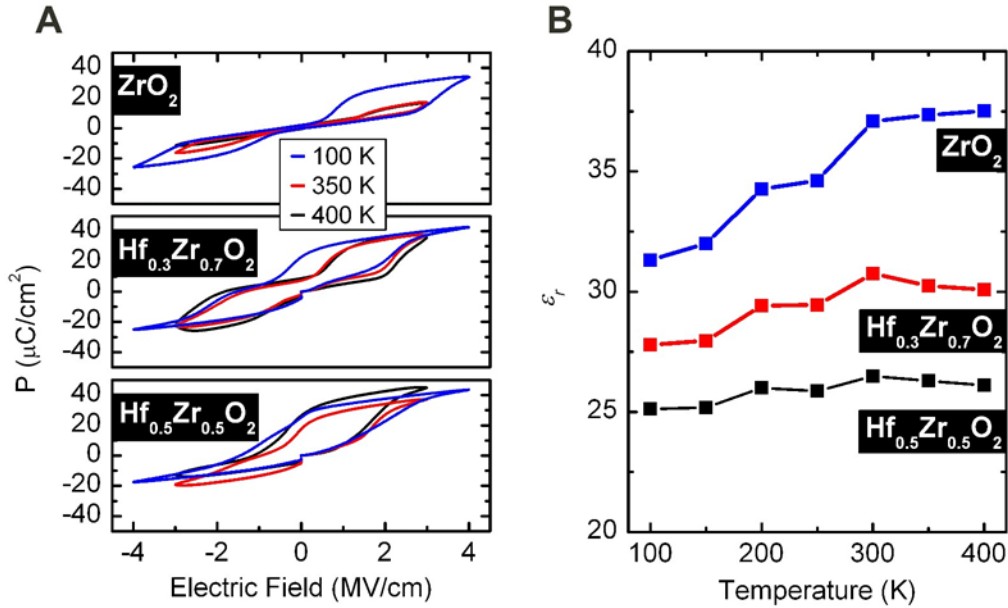


Figure 2.5. (A) Temperature dependent P-E loops ranging from 100 to 400 K for Hf<sub>0.5</sub>Zr<sub>0.5</sub>O<sub>2</sub>, Hf<sub>0.3</sub>Zr<sub>0.7</sub>O<sub>2</sub>, and ZrO<sub>2</sub>. (B) Increasing temperature dependence of the permittivity is observed from Hf<sub>0.5</sub>Zr<sub>0.5</sub>O<sub>2</sub> over Hf<sub>0.3</sub>Zr<sub>0.7</sub>O<sub>2</sub> towards ZrO<sub>2</sub>.<sup>16</sup> Reprinted (adapted) with permission from Johannes Müller, Tim S. Böschke, Uwe Schröder, Stefan Mueller, Dennis Bräuhaus, Ulrich Böttger, Lothar Frey, and Thomas Mikolajick, *Ferroelectricity in Simple Binary ZrO<sub>2</sub> and HfO<sub>2</sub>*, *Nano Letters* **12** (8), 4318 (2012). Copyright 2012 American Chemical Society.

$\text{J}/\text{cm}^3$  and  $\approx 25 \text{ J}/\text{cm}^3$  respectively from 25 °C to 125 °C and up to  $10^7$  cycles<sup>59</sup>. AFE-like

Hf<sub>0.3</sub>Zr<sub>0.7</sub>O<sub>2</sub> thin films with TiN electrodes have also demonstrated sustained ESD values of  $\approx 30$

$\text{J}/\text{cm}^3$  from 25 °C to 175 °C<sup>55</sup>. However, temperature stability of other parameters such as relative dielectric permittivity and loss tangent remain unreported in the literature.

The frequency studies conducted to date on ferroelectric HfO<sub>2</sub>-based thin films have been impedance spectroscopy measurements on both Si:HfO<sub>2</sub><sup>60</sup> and Gd:HfO<sub>2</sub><sup>29</sup>. The impedance spectroscopy measurements demonstrated the metal electrode/ ferroelectric thin film/metal electrode (MFM) devices needed four resistance capacitance (RC) elements to be modeled accurately, i.e. the bottom electrode, the ferroelectric thin film, the interfacial dead layers, and

the top electrode<sup>29,60</sup>. Both the impedance of the Si:HfO<sub>2</sub> and Gd:HfO<sub>2</sub> thin films decreased by 3 orders of magnitude from 1 Hz to 1 MHz<sup>29,60</sup>.

For resonators, the measurement of the quality factor ( $Q$ ) of the mechanical resonance is a dimensionless parameter that describes the initial energy stored in the parameter to the energy lost in a single cycle. In terms of resonance bandwidth,  $Q$  can be calculated using Eq. (2 – 2):

$$Q = \frac{f}{\delta} \quad (2 - 2)$$

Where  $f$  is the resonance frequency and  $\delta$  is the full width half max (FWHM) of the resonance<sup>61</sup>.

Prior to HfO<sub>2</sub>-based thin films, the miniaturization of high- $Q$  resonators was limited by the thickness of the piezoelectric thin films, such as PZT (120 nm). However, 30 nm thick HZO thin films have recently been demonstrated in double clamped resonators by Ghatge *et al.*<sup>62,63</sup>. An HZO-based double clamped resonator structure as shown in Figure 2.6<sup>63</sup>. The authors demonstrated the resonator had a  $Q$  factor of 15 at ambient pressure and 2300 at 800 mTorr<sup>63</sup>. The initial demonstration by Ghatge *et al.* is an exciting first step into the use of HfO<sub>2</sub>-based thin film resonators for high- $Q$  resonators.

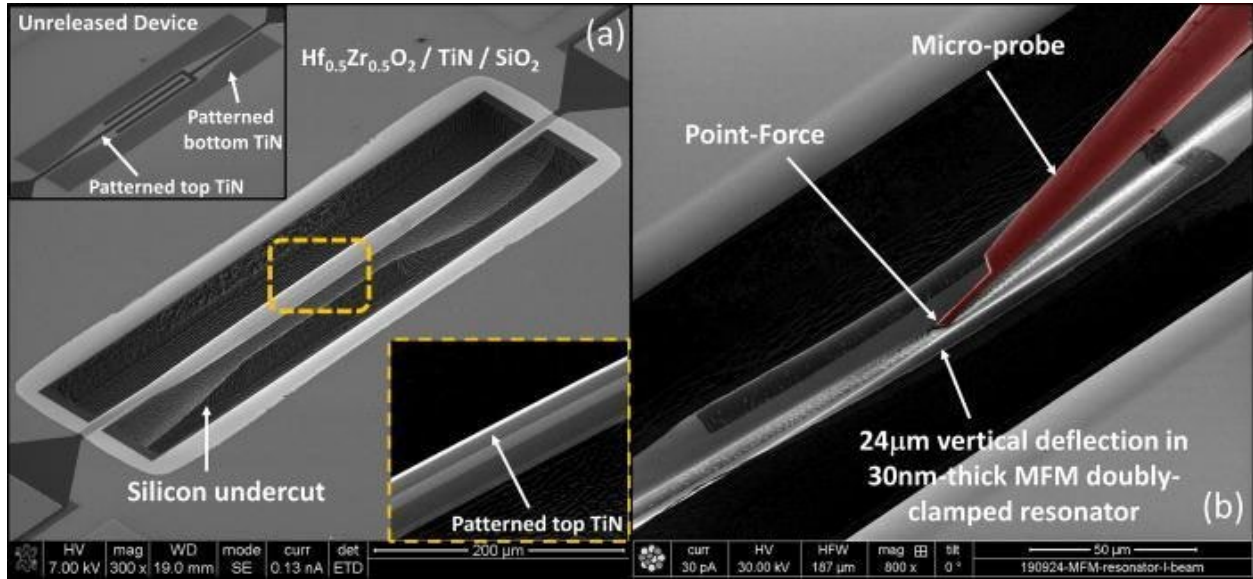


Figure 2.6. An SEM image of a doubly clamped resonator based on TiN/HZO/TiN stack with an aspect ratio exceeding  $10^4:1$ .<sup>63</sup> Reprinted from [M. Ghatge, G. Walters, T. Nishida, and R. Tabrizian, A 30-nm thick integrated hafnium zirconium oxide nano-electro-mechanical membrane resonator, *Applied Physics Letters* **116** (4), 043501 (2020)], with the permission of AIP Publishing.

### 2.2.7 Reliability Metrics

The final device parameters discussed in this section are reliability metrics. The most common reliability measurement performed on ferroelectric thin films is endurance cycling<sup>21</sup>. La:HfO<sub>2</sub> has been cycled up to  $10^5$  cycles without experiencing electrical breakdown<sup>64</sup>, Sr:HfO<sub>2</sub> samples have gone up to  $10^6$  before fatiguing, and Si:Hf<sub>0.5</sub>Zr<sub>0.5</sub>O<sub>2</sub> thin films have been demonstrated the ability to maintain ESD values up to  $10^9$  cycles<sup>59</sup>. As much as it is common to find the results of these measurements in literature for HfO<sub>2</sub>-based thin films, there is no standard operating procedure for the magnitude of the voltage applied nor the frequency or wave form of the voltage either in these endurance cycling measurements. Increasing the magnitude or decreasing the frequency of the applied voltage can result in different endurance cycling characteristics. For example, Lomenzo *et al.* conducted endurance cycling testing HZO-based capacitors at a variety of different applied field as shown in Figure 2.7<sup>59</sup>. With a higher applied

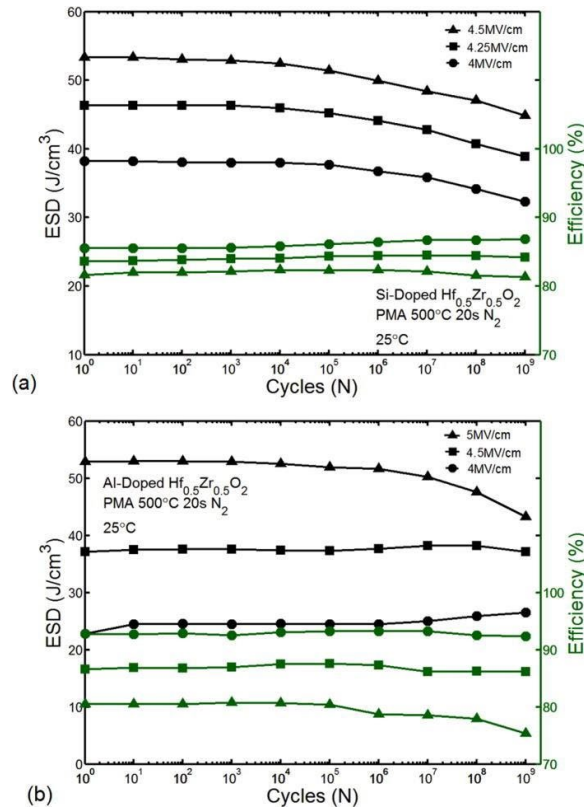


Figure 2.7. Plot of ESD and efficiency of (a) Si:HZO and (b) Al:HZO thin films at different electric fields.<sup>59</sup> Reprinted from [Patrick D. Lomenzo, Ching-Chang Chung, Chuanzhen Zhou, Jacob L. Jones, and Toshikazu Nishida, Doped Hf<sub>0.5</sub>Zr<sub>0.5</sub>O<sub>2</sub> for high efficiency integrated supercapacitors, Applied Physics Letters **110** (23), 232904 (2017)], with the permission of AIP Publishing.

voltage for endurance cycling, the Al-doped HZO thin film capacitors exhibit a  $P_r$  that decreases more rapidly than at lower applied voltages. Thus, it is important to consider other reliability metrics as well when analyzing HfO<sub>2</sub>-based devices. Another reliability metric that has been reported to analyze Si:HfO<sub>2</sub> thin films on an area enhanced substrate has been a Weibull modulus<sup>65</sup>. Eqs. (2 – 3) and (2 – 4) demonstrate how the Weibull distribution is calculated

$$X_i = \ln \ln(E_i) \quad (2 - 3)$$

$$Y_i = \ln \ln \left[ \ln \ln \left( 1 - \frac{i}{n + 1} \right) \right] \quad (2 - 4)$$

Where  $i$  is an individual sample,  $n$  is the total number of samples, and  $E_i$  is the breakdown strength of an individual sample. The Weibull modulus ( $\beta$ ), is the slope of linear-fitted curves in the Weibull distribution and refers to the reliability of the devices<sup>66</sup>. Kühnel *et al.* fitted Weibull distribution data and extrapolated a characteristic lifetime of 17.5 years for their area enhanced HZO devices with an operation voltage of 3V<sup>65</sup>.

## References

- 1 T. S. Böske, J. Müller, D. Bräuhäus, U. Schröder, and U. Böttger, *Applied Physics Letters* **99** (10), 102903 (2011).
- 2 Stefan Mueller, Johannes Mueller, Aarti Singh, Stefan Riedel, Jonas Sundqvist, Uwe Schroeder, and Thomas Mikolajick, *Advanced Functional Materials* **22** (11), 2412 (2012).
- 3 Tsubasa Tobase, Akira Yoshiasa, Hiroshi Arima, Kazumasa Sugiyama, Osamu Ohtaka, Tomotaka Nakatani, Ken-ichi Funakoshi, and Shinji Kohara, *physica status solidi (b)* **255** (11), 1800090 (2018).
- 4 J. E. Lowther, J. K. Dewhurst, J. M. Leger, and J. Haines, *Phys. Rev. B* **60** (21), 14485 (1999).
- 5 Tran Doan Huan, Vinit Sharma, George A. Rossetti, and Rampi Ramprasad, *Phys. Rev. B* **90** (6), 064111 (2014).
- 6 Lun Xu, Tomonori Nishimura, Shigehisa Shibayama, Takeaki Yajima, Shinji Migita, and Akira Toriumi, *Journal of Applied Physics* **122** (12), 124104 (2017).
- 7 Takahisa Shiraishi, Kiliha Katayama, Tatsuhiko Yokouchi, Takao Shimizu, Takahiro Oikawa, Osami Sakata, Hiroshi Uchida, Yasuhiko Imai, Takanori Kiguchi, Toyohiko J. Konno, and Hiroshi Funakubo, *Applied Physics Letters* **108** (26), 262904 (2016).
- 8 R. Materlik, C. Künneth, and A. Kersch, *Journal of Applied Physics* **117** (13), 134109 (2015).
- 9 Min Hyuk Park, Young Hwan Lee, Han Joon Kim, Tony Schenk, Woongkyu Lee, Keum Do Kim, Franz P. G. Fengler, Thomas Mikolajick, Uwe Schroeder, and Cheol Seong Hwang, *Nanoscale* **9** (28), 9973 (2017).
- 10 Ashish Pal, Vijay Kris Narasimhan, Stephen Weeks, Karl Littau, Dipankar Pramanik, and Tony Chiang, *Applied Physics Letters* **110** (2), 022903 (2017).
- 11 Choong-Ki Lee, Eunae Cho, Hyo-Sug Lee, Cheol Seong Hwang, and Seungwu Han, *Phys. Rev. B* **78** (1), 012102 (2008).
- 12 Tony Schenk, Uwe Schroeder, Milan Pešić, Mihaela Popovici, Yuriy V. Pershin, and Thomas Mikolajick, *ACS Appl. Mater. Interfaces* **6** (22), 19744 (2014).
- 13 Rohit Batra, Tran Doan Huan, Jacob L. Jones, George Rossetti, and Rampi Ramprasad, *The Journal of Physical Chemistry C* **121** (8), 4139 (2017).
- 14 Rohit Batra, Tran Doan Huan, George A. Rossetti, and Rampi Ramprasad, *Chem. Mater.* **29** (21), 9102 (2017).
- 15 Christopher Künneth, Robin Materlik, Max Falkowski, and Alfred Kersch, *ACS Applied Nano Materials* **1** (1), 254 (2018).
- 16 Johannes Müller, Tim S. Böske, Uwe Schröder, Stefan Mueller, Dennis Bräuhäus, Ulrich Böttger, Lothar Frey, and Thomas Mikolajick, *Nano Letters* **12** (8), 4318 (2012).
- 17 S. Mueller, C. Adelman, A. Singh, S. Van Elshocht, U. Schroeder, and T. Mikolajick, *ECS Journal of Solid State Science and Technology* **1** (6), N123 (2012).
- 18 J. Müller, U. Schröder, T. Böske, I. Müller, U. Böttger, L. Wilde, J. Sundqvist, M. Lemberger, P. Kuecher, T. Mikolajick, and L. Frey, *Journal of Applied Physics* **110**, 114113 (2011).
- 19 M. G. Kozodaev, A. G. Chernikova, E. V. Korostylev, M. H. Park, U. Schroeder, C. S. Hwang, and A. M. Markeev, *Applied Physics Letters* **111** (13), 132903 (2017).

20 T. Schenk, S. Mueller, U. Schroeder, R. Materlik, A. Kersch, M. Popovici, C. Adelman, S. Van Elshocht, and T. Mikolajick, presented at the 2013 Proceedings of the European Solid-State Device Research Conference (ESSDERC), 2013 (unpublished).

21 Min Hyuk Park, Young Hwan Lee, Han Joon Kim, Yu Jin Kim, Taehwan Moon, Keum Do Kim, Johannes Müller, Alfred Kersch, Uwe Schroeder, Thomas Mikolajick, and Cheol Seong Hwang, *Advanced Materials* **27** (11), 1811 (2015).

22 Y. Zhou, Y. K. Zhang, Q. Yang, J. Jiang, P. Fan, M. Liao, and Y. C. Zhou, *Computational Materials Science* **167**, 143 (2019).

23 K. D. Kim, M. H. Park, H. J. Kim, Y. J. Kim, T. Moon, Y. H. Lee, S. D. Hyun, T. Gwon, and C. S. Hwang, *J. Mater. Chem. C* **4** (28), 6864 (2016).

24 Min Hyuk Park, Han Joon Kim, Yu Jin Kim, Woongkyu Lee, Taehwan Moon, and Cheol Seong Hwang, *Applied Physics Letters* **102** (24), 242905 (2013).

25 Patrick D. Lomenzo, Qanit Takmeel, Saeed Moghaddam, and Toshikazu Nishida, *Thin Solid Films* **615**, 139 (2016).

26 Y. Lee, Y. Goh, J. Hwang, D. Das, and S. Jeon, *IEEE Transactions on Electron Devices* **68** (2), 523 (2021).

27 Min Hyuk Park, Han Joon Kim, Yu Jin Kim, Taehwan Moon, and Cheol Seong Hwang, *Applied Physics Letters* **104** (7), 072901 (2014).

28 Dayu Zhou, Jin Xu, Qing Li, Yan Guan, Fei Cao, Xianlin Dong, Johannes Müller, Tony Schenk, and Uwe Schröder, *Applied Physics Letters* **103** (19), 192904 (2013).

29 Everett D. Grimley, Tony Schenk, Xiahan Sang, Milan Pešić, Uwe Schroeder, Thomas Mikolajick, and James M. LeBeau, *Advanced Electronic Materials* **2** (9), 1600173 (2016).

30 Patrick D. Lomenzo, Claudia Richter, Thomas Mikolajick, and Uwe Schroeder, *ACS Applied Electronic Materials* **2** (6), 1583 (2020).

31 Patrick D. Lomenzo, Qanit Takmeel, Chuanzhen Zhou, Chris M. Fancher, Eric Lambers, Nicholas G. Rudawski, Jacob L. Jones, Saeed Moghaddam, and Toshikazu Nishida, *Journal of Applied Physics* **117** (13), 134105 (2015).

32 Chao Li, Yuan Yao, Xi Shen, Yanguo Wang, Junjie Li, Changzhi Gu, Richeng Yu, Qi Liu, and Ming Liu, *Nano Research* **8** (11), 3571 (2015).

33 S. Starschich, S. Menzel, and U. Böttger, *Applied Physics Letters* **108** (3), 032903 (2016).

34 Tony Schenk, Michael Hoffmann, Johannes Ocker, Milan Pešić, Thomas Mikolajick, and Uwe Schroeder, *ACS Appl. Mater. Interfaces* **7** (36), 20224 (2015).

35 Takao Shimizu, Takanori Mimura, Takanori Kiguchi, Takahisa Shiraishi, Toyohiko Konno, Yoshio Katsuya, Osami Sakata, and Hiroshi Funakubo, *Applied Physics Letters* **113** (21), 212901 (2018).

36 M. Lederer, T. Kämpfe, R. Olivo, D. Lehniger, C. Mart, S. Kirbach, T. Ali, P. Polakowski, L. Roy, and K. Seidel, *Applied Physics Letters* **115** (22), 222902 (2019).

37 S. Kirbach, M. Lederer, S. Eßlinger, C. Mart, M. Czernohorsky, W. Weinreich, and T. Wallmersperger, *Applied Physics Letters* **118** (1), 012904 (2021).

38 Xiahan Sang, Everett D. Grimley, Tony Schenk, Uwe Schroeder, and James M. LeBeau, *Applied Physics Letters* **106** (16), 162905 (2015).

39 Fei Huang, Xing Chen, Xiao Liang, Jun Qin, Yan Zhang, Taixing Huang, Zhuo Wang, Bo Peng, Peiheng Zhou, Haipeng Lu, Li Zhang, Longjiang Deng, Ming Liu, Qi Liu, He Tian, and Lei Bi, *Phys. Chem. Chem. Phys.* **19** (5), 3486 (2017).

40 Sebastian E. Reyes-Lillo, Kevin F. Garrity, and Karin M. Rabe, *Phys. Rev. B* **90** (14),  
140103 (2014).

41 Images generated using CrystalMaker®: a crystal and molecular structures program for  
Mac and Windows. CrystalMaker Software Ltd, Oxford, England  
([www.crystallmaker.com](http://www.crystallmaker.com)).

42 S. V. Barabash, *J Comput Electron* **16** (4), 1227 (2017).

43 H. Domingos, D. Quattro, and J. Scaturro, *IEEE Transactions on Components, Hybrids,  
and Manufacturing Technology* **1** (4), 423 (1978).

44 Bill Long, Mike Prevallet, John D. Prymak, and E. Woodfield, 2005 (unpublished).

45 M. H. Park, T. Schenk, C. M. Fancher, E. D. Grimley, C. Zhou, C. Richter, J. M. LeBeau,  
J. L. Jones, T. Mikolajick, and U. Schroeder, *J. Mater. Chem. C* **5** (19), 4677 (2017).

46 R. Materlik, TU Dresden, 2019.

47 Dominik Martin, Johannes Müller, Tony Schenk, Thomas M. Arruda, Amit Kumar,  
Evgheni Strelcov, Ekaterina Yurchuk, Stefan Müller, Darius Pohl, Uwe Schröder, Sergei  
V. Kalinin, and Thomas Mikolajick, *Advanced Materials* **26** (48), 8198 (2014).

48 S. Kirbach, K. Kühnel, and W. Weinreich, presented at the 2018 IEEE 18th International  
Conference on Nanotechnology (IEEE-NANO), 2018 (unpublished).

49 Clemens Mart, Thomas Kämpfe, Raik Hoffmann, Sophia Eßlinger, Sven Kirbach, Kati  
Kühnel, Malte Czernohorsky, Lukas M. Eng, and Wenke Weinreich, *Advanced  
Electronic Materials* **6** (3), 1901015 (2020).

50 F. Griggio, S. Jesse, A. Kumar, O. Ovchinnikov, H. Kim, T. N. Jackson, D. Damjanovic,  
S. V. Kalinin, and S. Trolier-McKinstry, *Phys. Rev. Lett.* **108** (15), 157604 (2012).

51 H. Alex Hsain, Pankaj Sharma, Hyeonggeun Yu, Jacob L. Jones, Franky So, and Jan  
Seidel, *Applied Physics Letters* **113** (2), 022905 (2018).

52 T. Zednicek, Sikula, J., Leibovitz, H., AVX Tantalum Corporation, Technical Report,  
2020.

53 "Section 4: Technical Summary and Application Guidelines" AVX, Technical Report.

54 M. H. Park, H. J. Kim, Y. J. Kim, T. Moon, K. D. Kim, Y. H. Lee, S. D. Hyun, and C. S.  
Hwang, *J. Mater. Chem. C* **3** (24), 6291 (2015).

55 Min Hyuk Park, Han Joon Kim, Yu Jin Kim, Taehwan Moon, Keum Do Kim, and Cheol  
Seong Hwang, *Advanced Energy Materials* **4** (16), 1400610 (2014).

56 Mailadil T. Sebastian, in *Dielectric Materials for Wireless Communication*, edited by  
Mailadil T. Sebastian (Elsevier, Amsterdam, 2008), pp. 11.

57 M. Aldrigo, M. Dragoman, S. Iordanescu, F. Nastase, S. Vulpe, A. Dinescu, and D.  
Vasilache, *IEEE Access* **7**, 136686 (2019).

58 Min Hyuk Park, Ching-Chang Chung, Tony Schenk, Claudia Richter, Michael  
Hoffmann, Steffen Wirth, Jacob L. Jones, Thomas Mikolajick, and Uwe Schroeder,  
*Advanced Electronic Materials* **4** (4), 1700489 (2018).

59 Patrick D. Lomenzo, Ching-Chang Chung, Chuanzhen Zhou, Jacob L. Jones, and  
Toshikazu Nishida, *Applied Physics Letters* **110** (23), 232904 (2017).

60 T. Schenk, M. Hoffmann, M. Pešić, M. H. Park, C. Richter, U. Schroeder, and T.  
Mikolajick, *Physical Review Applied* **10** (6), 064004 (2018).

61 Markys G. Cain and Mark Stewart, in *Characterisation of Ferroelectric Bulk Materials  
and Thin Films*, edited by Markys G. Cain (Springer Netherlands, Dordrecht, 2014), pp.  
15.

- 62 Mayur Ghatge, Glen Walters, Toshikazu Nishida, and Roozbeh Tabrizian, *Nature*  
Electronics **2** (11), 506 (2019).
- 63 M. Ghatge, G. Walters, T. Nishida, and R. Tabrizian, *Applied Physics Letters* **116** (4),  
043501 (2020).
- 64 Uwe Schroeder, Claudia Richter, Min Hyuk Park, Tony Schenk, Milan Pešić, Michael  
Hoffmann, Franz P. G. Fengler, Darius Pohl, Bernd Rellinghaus, Chuanzhen Zhou,  
Ching-Chang Chung, Jacob L. Jones, and Thomas Mikolajick, *Inorganic Chemistry* **57**  
(5), 2752 (2018).
- 65 Kati Kühnel, Malte Czernohorsky, Clemens Mart, and Wenke Weinreich, *Journal of*  
*Vacuum Science & Technology B* **37** (2), 021401 (2019).
- 66 J. D. Sullivan and P. H. Lauzon, *J Mater Sci Lett* **5** (12), 1245 (1986).

## **Chapter 3: Characterization Platform Overview**

The purpose of this dissertation was to design and demonstrate an all-in-one characterization platform for ferroelectric thin films grown via ALD. This chapter is intended to serve as a guide for any future researchers that desire to create and use the platform for their own research. The first part of this chapter explains the characterization structures and their intended purpose, the latter part of the chapter gives a detailed process flow in how to create these structures.

### **3.1. Characterization Structures**

#### **3.1.1. Planar Structures**

The 150 mm substrate is designed to be diced into 25 mm × 25 mm chips, an example chip is shown in Figure 3.1. Each chip is designed with 5 mm wide strips centered horizontally and vertically down its center of holes, trenches, and fins. This cross region outlined in green in Figure 3.1. divides each chip into 4 quadrants. There are 5 different quadrant designs, which are dispersed in relatively equal numbers across the entire substrate. The first quadrant design, labeled Quadrant 1 in Figure 3.1., is an array of planar capacitors. The arrays contain a total of 180 planar capacitors which are either 0.492 mm<sup>2</sup> or 1.81 mm<sup>2</sup> in size. Arrayed planar capacitors allow for the use of an auto probing station, which takes electrical measurements of many samples quickly. Electrical measurements of multiple planar capacitors enable analysis of the consistency of device parameters such as breakdown voltage and loss tangent from device to device. Other large sections of planar film are on the substrate to enable measurements like

ellipsometry or x-ray photoelectron spectroscopy, which could also be used to incorporate new device designs in future 3D structured substrate iterations.

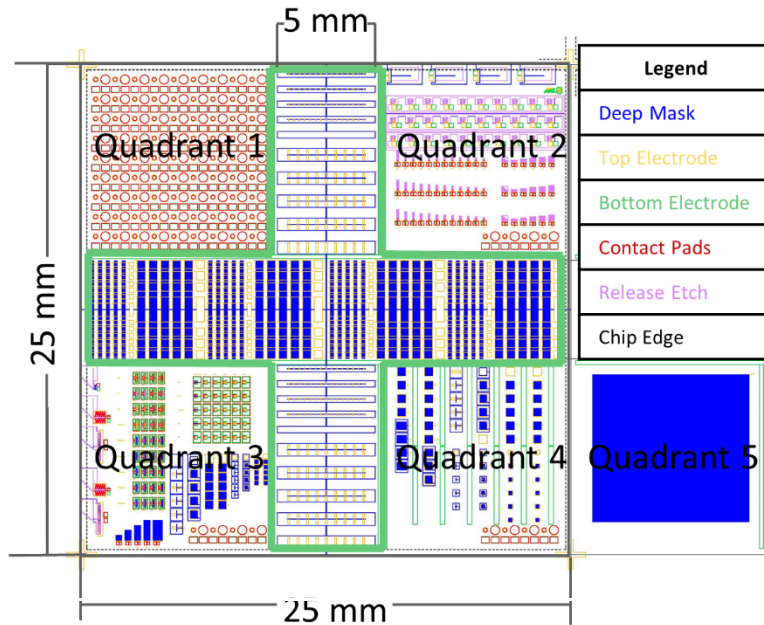


Figure 3.1. AutoCAD drawing of a 25 mm x 25 mm chip on the 6" wafer, the chip contains 4 quadrants separated by a 5 mm wide cross section of holes, trenches, and fins outlined in green. The schematic also shows the 5th quadrant design as well.

### 3.1.2. Area Enhanced Devices

Arrays of holes, pillars, and trenches can be found not only in the cross section outlined in green in Figure 3.1., but also in Quadrants 3 and 4. These structures increase the active device area without altering the footprint. This enhancement in device area leads to an enhancement of the capacitance as previously explained in section 1.2. Schematics of the three different types of capacitors with trenches, holes, and pillars are shown in Figure 3.2., along with a cross section scanning electron microscopy (SEM) image taken of the trenches. A table listing the various hole diameter, pillar diameter, or trench widths of features in area-enhanced capacitors (AECs), followed by an estimated depth of those features, and an estimated increase in surface area over

the AECs planar counterpart is shown in Table 3.1. The estimated surface area increase is the ratio of the surface area of the AEC divided by footprint of that AEC. The footprint of the AEC is the same as that of a planar capacitor on the substrate.

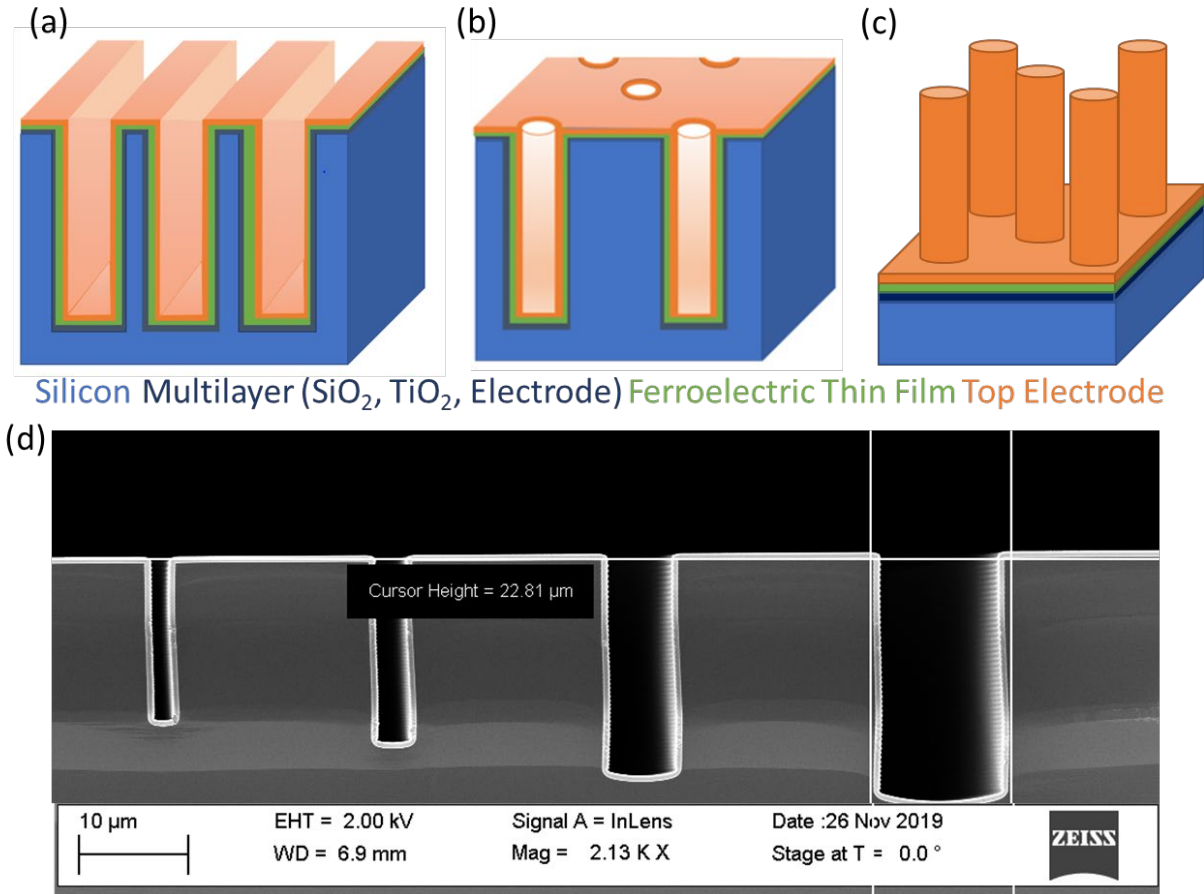


Figure 3.2. (a) Schematic of trench capacitor, (b) schematic of capacitor with holes, (c) schematic of pillar array capacitor, (d) SEM image of cross section of trenches with variable widths and depths.

Table 3.1. List of types of area enhanced capacitors with type of structure, diameter or width of structure, number of structures, electrode footprint, and surface area enhancement in order of surface area enhancement.

Structure	Diameter or Width (μm)	Number of structures	Electrode Footprint (cm <sup>2</sup> )	Surface Area Enhancement
Holes	0.5	42	0.000492	1.01
Holes	0.5	187	0.00181	1.01
Holes	1	42	0.000492	1.03
Holes	1	187	0.00181	1.03
Holes	2	42	0.000492	1.06

Table 3.1. (continued)

<b>Pillars</b>	4	20	0.00181	1.07
<b>Holes</b>	2	187	0.00181	1.07
<b>Pillars</b>	4	93	0.000492	1.09
<b>Pillars</b>	8	20	0.000492	1.16
<b>Trenches</b>	5	42	0.000492	1.20
<b>Pillars</b>	8	93	0.00181	1.21
<b>Holes</b>	5	187	0.000492	1.24
<b>Trenches</b>	5	6	0.00181	1.33
<b>Trenches</b>	0.5	6	0.000492	1.39
<b>Holes</b>	16	20	0.00181	1.41
<b>Trenches</b>	1	6	0.000492	1.45
<b>Trenches</b>	10	42	0.00181	1.46
<b>Trenches</b>	0.5	13	0.00181	1.49
<b>Trenches</b>	16	93	0.000492	1.52
<b>Pillars</b>	2	6	0.000492	1.55
<b>Trenches</b>	10	187	0.00181	1.55
<b>Trenches</b>	22	20	0.000492	1.56
<b>Pillars</b>	1	13	0.00181	1.56
<b>Holes</b>	0.5	7618	0.00181	1.58
<b>Holes</b>	2	13	0.000492	1.69
<b>Trenches</b>	22	93	0.00181	1.71
<b>Pillars</b>	10	6	0.000492	1.75
<b>Holes</b>	5	13	0.00181	1.84
<b>Pillars</b>	1	20	0.00181	1.87
<b>Trenches</b>	10	13	0.00181	1.94
<b>Trenches</b>	2	20	0.00181	2.06
<b>Holes</b>	22	19	0.00181	2.52
<b>Trenches</b>	1	38	0.00181	2.65
<b>Fins</b>	22	224	0.000492	2.71
<b>Pillars</b>	8	837	0.00181	2.86
<b>Pillars</b>	16	25	0.00181	3.00
<b>Trenches</b>	2	38	0.00181	3.01
<b>Fins</b>	5	822	0.000492	3.15
<b>Pillars</b>	16	389	0.00181	3.16
<b>Fins</b>	8	41	0.000492	3.62
<b>Holes</b>	5	2083	0.00181	3.73
<b>Fins</b>	4	63	0.000492	4.12
<b>Pillars</b>	1	77	0.00181	4.34
<b>Trenches</b>	4	3680	0.00181	4.58
<b>Trenches</b>	2	77	0.00181	5.07
<b>Trenches</b>	1	96	0.00181	5.17

Table 3.1. (continued)

<b>Trenches</b>	2	96	0.00181	5.91
<b>Holes</b>	1	42624	0.00181	7.11
<b>Holes</b>	2	18870	0.00181	8.51
<b>Trenches</b>	1	192	0.00181	9.34
<b>Holes</b>	1	76181	0.00181	11.70

### 3.1.3. Theta Mechanical Test Structures

Quadrant 2 shown in Figure 3.1., contains theta mechanical test structures, M-cantilevers, and piano key cantilevers. A schematic of the theta mechanical test structure beside an SEM image of a produced theta mechanical test structure is shown Figure 3.3. The theta mechanical test

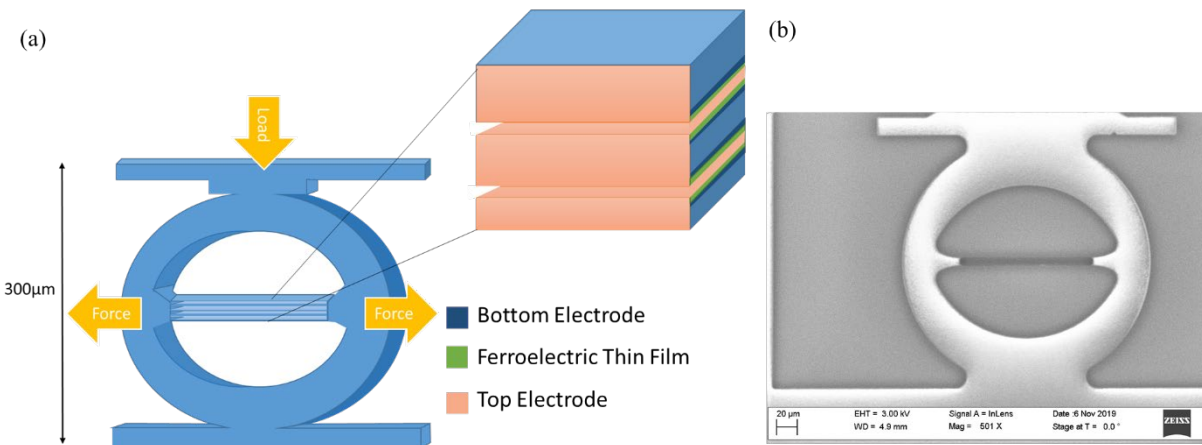


Figure 3.3. (a) schematic of theta mechanical test structure (b) SEM image of theta mechanical test structure.

structures were developed at NIST in 2011<sup>1</sup>. The design created for this work expands upon the original idea with the addition of trenches in the webbing. When force is applied to the top of the theta structure a tensile strain is induced across the webbing. This in turn, gives rise to an electrical response in the film. From the measurements of the electric response of the thin film, the direct piezoelectric coefficient can be calculated. The creation and use of the theta mechanical test structures requires the use of a silicon-on-insulator (SOI) substrate. The theta mechanical test structures were placed on the substrate in rows of 10, with each quadrant 2 on

the substrate containing a total of 30 theta mechanical test structures. If using an SOI substrate, these rows could be removed from the substrate and turned upright and loaded into an instrumented indentation testing device<sup>1</sup>.

### 3.1.4. Cantilevers

The M-cantilevers and piano key cantilevers enable the indirect piezoelectric coefficient to be calculated. Schematics along with an SEM image or optical microscope image of these devices are shown in Figure 3.4. When an electric field is applied to these structures, the tip of

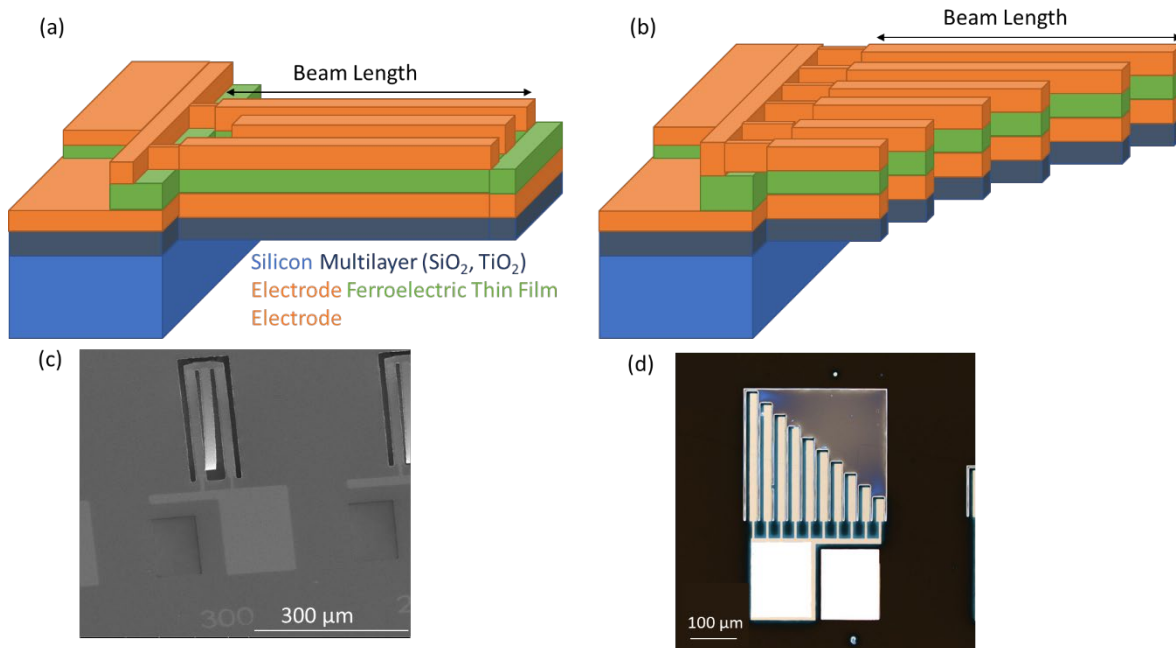


Figure 3.4. (a) Schematic of an M-cantilever, (b) schematic of a piano key cantilever, (c) SEM image of an M-cantilever, (d) Optical microscope image of a piano-key cantilever.

the cantilever displaces. This displacement can be measured using Laser Doppler Vibrometry (LDV). With knowledge of the layers in the cantilever, along with the layer thicknesses, and length of the cantilever, the indirect piezoelectric coefficient can be calculated. The M-cantilever was designed to reduce tensile strain with the side arms curling one direction, and the center arm curling in the opposite direction. The piano key cantilevers are a more traditional cantilever

design but have 10 cantilevers off a single set of electrode pads. There are also a series of long arm piano keys that require the use of an SOI substrate to be manufactured. These two cantilevers, along with all the resonators present on the substrate were designed by Ryan Q. Rudy, a Research Scientist at the Army Research Laboratory. All the various types of cantilevers produced, and their perspective beam lengths are listed in Table 3.2.

Table 3.2. List of type of cantilever produced, along with beam length(s), and number of that type of cantilever per quadrant 2 found on the substrate.

<b>Cantilever Type</b>	<b>Beam Length(s) <math>\mu\text{m}</math></b>	<b>Number Per Quadrant 2</b>
<b>M-cantilever</b>	500	3
<b>M-cantilever</b>	400	3
<b>M-cantilever</b>	350	3
<b>M-cantilever</b>	300	3
<b>M-cantilever</b>	275	3
<b>M-cantilever</b>	250	3
<b>M-cantilever</b>	225	3
<b>M-cantilever</b>	200	3
<b>M-cantilever</b>	175	3
<b>M-cantilever</b>	150	3
<b>M-cantilever</b>	125	3
<b>M-cantilever</b>	100	3
<b>Piano Key Cantilever</b>	50,75,100,125,150,175,200,225,250,275	3
<b>Piano Key Cantilever</b>	100	3
<b>Piano Key Cantilever</b>	150	3
<b>Piano Key Cantilever</b>	200	3
<b>Piano Key Cantilever</b>	250	3
<b>Piano Key Cantilever</b>	300	3
<b>Piano Key Cantilever (SOI)</b>	1000	2
<b>Piano Key Cantilever (SOI)</b>	750	1
<b>Piano Key Cantilever (SOI)</b>	500	1
<b>Piano Key Cantilever (SOI)</b>	250	1

### 3.1.5. Actuators

The final set of structures on Quadrant 2 are actuators. There are cymbal actuators<sup>2</sup>, a top down schematic a device is shown in Figure 3.5a., with a 3D rendering in Figure 3.5b. The cymbal actuators are intended to enhance displacement produced by the piezoelectric thin film, the center strip is designed to actuate along its length in the direction of the arrow in Figure 3.5a., while the outer cymbal shaped caps actuate outward in the directions of the arrows. The cymbal arms are set at a  $2^\circ$  angle from the center strip of the device. The cymbal actuators on the 3D structured substrate vary in cymbal depth 10  $\mu\text{m}$ , 20  $\mu\text{m}$ , or 30  $\mu\text{m}$ . There is also a cymbal actuator designed with 5-cymbals, and that is shown in an optical microscope image in Figure 3.5c.

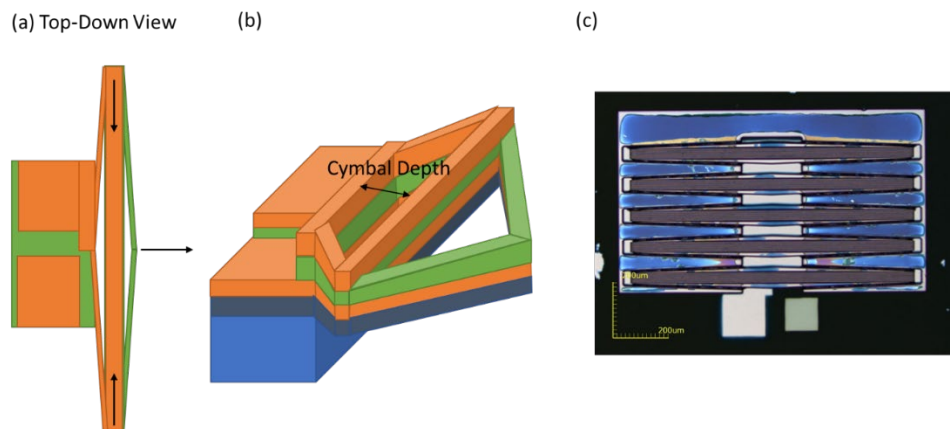


Figure 3.5. (a) Schematic of a cymbal actuator from a top-down perspective, (b) a 3D schematic of the cymbal actuator, (c) an optical microscope image of a 5-cymbal actuator.

Other types of actuators can be found on the mask in Quadrant 3. These are butterfly actuators, which are designed to measure in plane actuation. A schematic is shown in Figure 3.6a., with an optical microscope image in Figure 3.6b. A number of the butterfly actuator

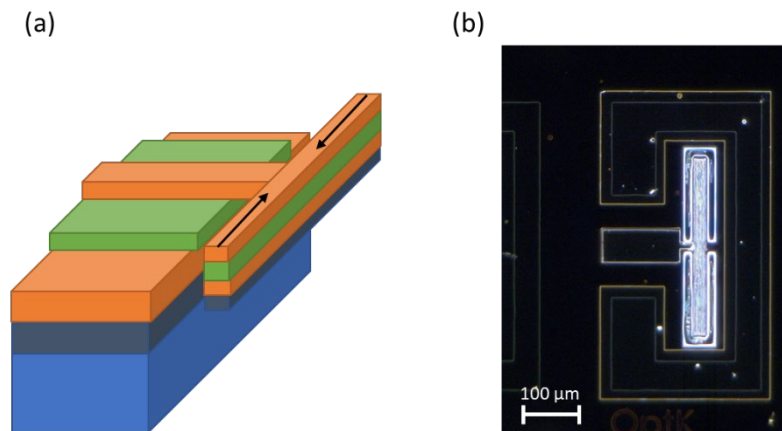


Figure 3.6. (a) Schematic of a butterfly actuator with arrows in the direction of actuation, (b) an optical microscope image of a butterfly actuator.

designs incorporate trenches across the length of the ‘wings’, these actuator designs specifically require the use of an SOI substrate to be created.

### 3.1.6. Resonators

Quadrant 3 mainly consists of resonator structures. The first set of resonators were adapted based on the work done by Ramezani *et. al.*, who demonstrated the first ferroelectric-on-semiconductor fin bulk acoustic resonators (FoS-FinBAR)<sup>3,4</sup>. Ramezani *et. al.* created silicon fin structures via Bosch deep reactive ion etching (DRIE) and then smoothed them with a high temperature hydrogen anneal. The created fin is then coated in either a Mo/AlN/Mo stack via sputtering<sup>3</sup> or a TiN/HZO/TiN stack via ALD<sup>4</sup>. These FoS-FinBAR have been proven to have electromechanical coupling factor ( $k_{eff}^2$ ) as high as 4.7% while maintaining high quality factors ( $Q$ s) as high as 500 at frequencies as large as 18 GHz<sup>5</sup>. The ability to maintain a large  $Q$  value at such a large frequency provides a distinct advantage to the FoS-FinBAR over planar or bulk acoustic wave resonators, which are limited to a range of 0.3-6 GHz<sup>5</sup>. However, to create these fin structures, large areas of etched silicon are required around the fin structure. The design of the fin resonator structures in Quadrant 5 are fins formed in between two trenches. These

resonator structures can be created with high aspect ratios but have the benefit of a smaller footprint as they do not require a large area of etched silicon around them and can be integrated more readily into standard commercial microchip designs.

### 3.1.7. Trenches for Sidewall Crystal Structure Characterization

Quadrant 5 on the substrate is a large, approximately 5 mm x 5 mm array of 2  $\mu\text{m}$  wide trenches. This dense array of trenches was designed to determine the crystal structure of ferroelectric thin films deposited on vertical sidewalls. This is accomplished by ion milling the trench arrays, removing the section of film from the top and bottom of the trenches as shown in Figure 3.7., leaving only the metal/ferroelectric thin film/metal (MFM) stack on the sidewalls of



Figure 3.7. Schematic of trenches pre and post ion milling leaving the thin film on the sidewalls of the trenches for XRD analysis.

the trenches. Measuring an XRD pattern of the post ion milled array isolates the crystallographic structure of the thin film on the sidewalls<sup>6</sup>. By comparing the XRD of the sidewall thin film only to that of XRD pattern of the ferroelectric thin film on the planar regions, the crystallographic differences between the planar and sidewall thin films can be elucidated.

## 3.2. Process Flow Overview

### 3.2.1. Photolithography

The creation of the 3D structured characterization platform begins with a (100)-oriented prime 150 mm wafer. A 5 photomask process is used to create the 3D structured substrates. The photolithography process used to create each of the patterns from the individual masks in this process starts with a clean wafer, which is then exposed to hexamethyldisilazane (HMDS) vapor in an oven set at 130 °C. For the first mask, which is called the “deep optical mask” in this work, the wafer is then spin coated using AZ 5214 photoresist at 4000 rpm for 40 seconds. The photoresist then is baked at 110 °C for 60 seconds. The wafer is then exposed using the deep optical mask to a UV dosage of 55 mJ/cm<sup>2</sup>. AZ 5214 is a positive photoresist, meaning that the resist that is exposed to UV light becomes more soluble in photoresist developer. This process is depicted in Figure 3.8. Thus, regions exposed are washed away in the developer, leaving regions

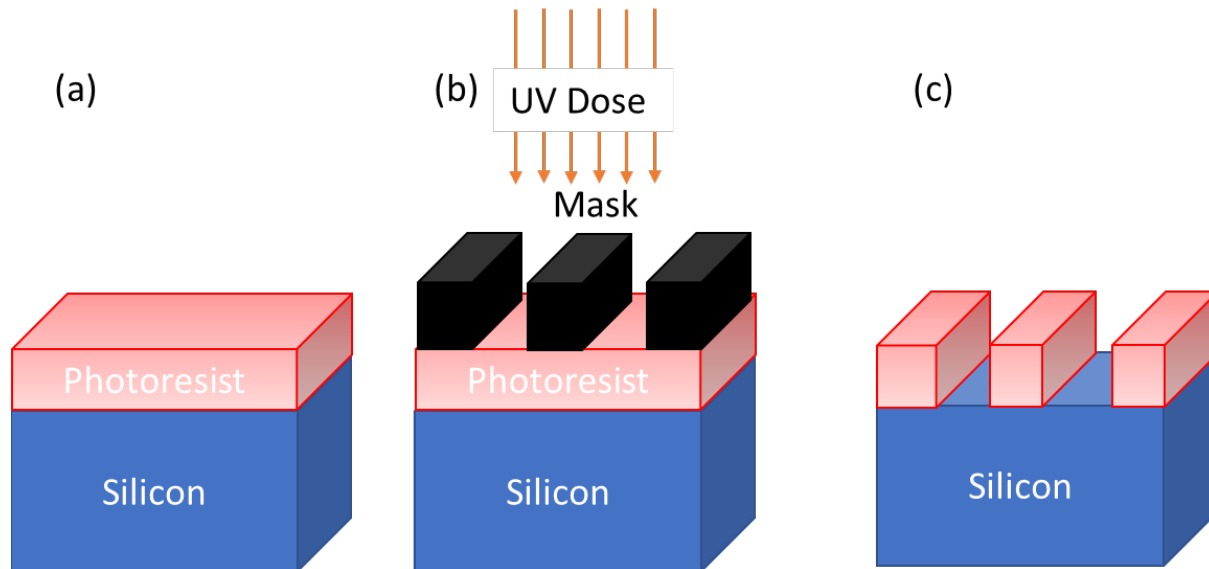


Figure 3.8. (a) Schematic of silicon wafer after applying photoresist, (b) schematic of patterning the photoresist using an optical mask with a UV dose, (c) silicon with photoresist after developing the photoresist.

of bare silicon that can then be etched via DRIE to create holes, pillars, trenches, and fins. A

final clean of the exposed area before the samples undergo DRIE is a plasma clean for 5 minutes in a PVA TePla Ion 40 Plasma System.

### **3.2.2. Deep Reactive Ion Etching**

The DRIE process uses alternating etching and passivation steps to create high aspect ratio structures.  $\text{SF}_6$  plasma is accelerated at the surface of the substrate and has some directionality, the plasma then etches the Si,  $\text{SiF}_x$  is the etchant byproduct. The  $\text{SF}_6$  plasma is created by applying RF power to the  $\text{SF}_6$  gas. The free radicals generated by the plasma enable etching through chemical reactions, the  $\text{SF}_x$  radicals react with the Si to produce  $\text{SiF}_4$ . However, the plasma also creates ions which can physically etch a sample. With enough energy, these ions can knock atoms out of the material to be etched without a chemical reaction. The physical mechanism of the ion etching greatly increases the etch rate, but more ions strike the surfaces perpendicular (bottom of a feature) to the beam than parallel (sidewalls of a feature), thus high aspect ratio structures can be formed. A  $\text{C}_4\text{F}_8$  plasma is then applied after the  $\text{SF}_6$  plasma to apply an etch resistant polymer conformally on the etched region. Due to the directionality of the  $\text{SF}_6$  plasma, the sidewall lateral etch is slower than that vertical depth etch. Repetition of the etch/passivation cycle results in high aspect ratio structures on the Si substrate<sup>7</sup>. The DRIE process is depicted in Figure 3.9. The DRIE system that was used was a Plasma-Therm Versaline Deep Silicon Etcher. The depth of the structures created via the DRIE process used for these wafers range from almost 1:2 to just over 1:26 and is shown in Figure 3.10. After completion of the DRIE, the photoresist present on the wafer is removed using a ratio of 3:1 sulfuric acid to hydrogen peroxide, often called a piranha solution. After this step the wafers were either

produced with Pt electrodes or TiN electrodes, the processing steps for each are outlined sequentially below.

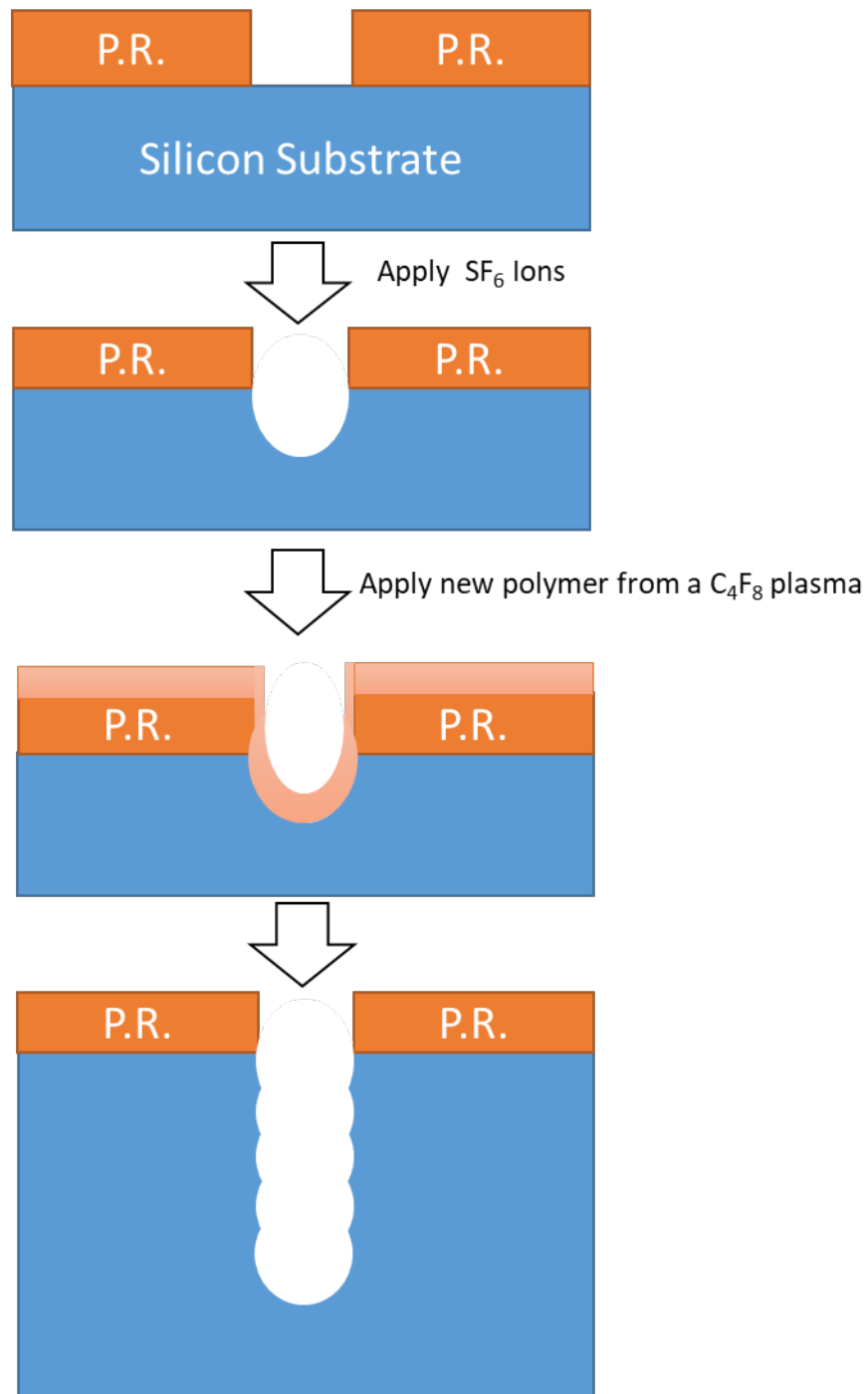


Figure 3.9. Schematic of the deep reactive ion etching process of a silicon wafer with a patterned photoresist (P.R.).

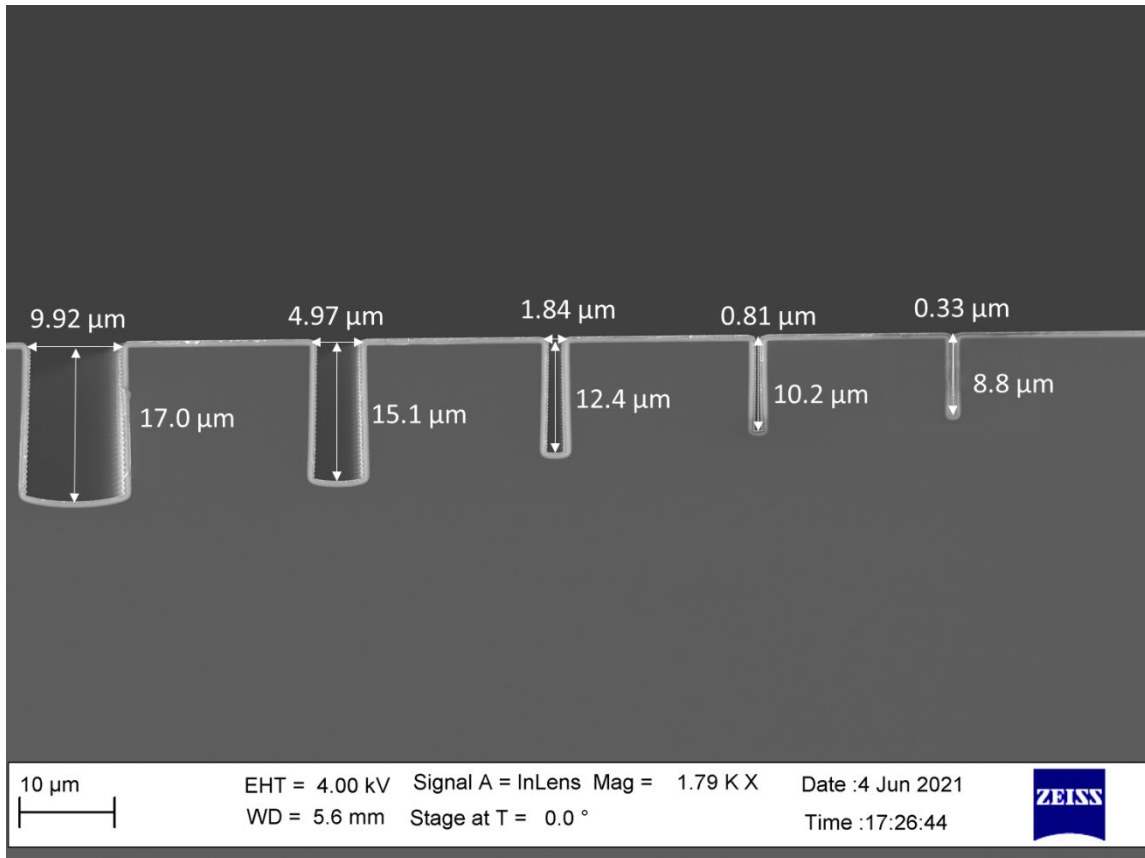


Figure 3.10. An SEM image of the various trench structures with their widths and lengths labeled.

### 3.2.3. TiN/Al:HfO<sub>2</sub>/TiN Sample Creation

The planar substrates underwent a wet thermal oxidation process in a Tystar ® Titan 3800 furnace at 1100 °C for 38 minutes and 40 sec to create a 500 nm +/- 5 % SiO<sub>2</sub> layer at the Army Research Laboratory. 4 at % 50 nm Al:HfO<sub>2</sub> thin films on TiN were prepared at the North Carolina State University Nanofabrication Facility (NNF). A 50 nm TiN bottom electrode was deposited on a Si/SiO<sub>2</sub> 3D structured substrate using plasma-enhanced atomic layer deposition (PEALD). An Ultratech/Cambridge Fiji G2 system was used for the ALD growths. The precursor used was tetrakis(dimethylamido)-titanium(IV) at a pressure of ~0.1 Torr for its half-cycles and 0.01 Torr for plasma half-cycles. Ar/N<sub>2</sub> gas was used to generate plasma, which was pulsed for 20 s at 250 W. After the TiN bottom electrode deposition, the substrate was not

removed from the chamber, i.e. the samples were grown via a Sequential, No-Atmosphere Process (SNAP)<sup>8</sup>. The 50 nm Al:HfO<sub>2</sub> was deposited using thermal ALD with TDMAH and TMA as the precursors and H<sub>2</sub>O as the oxidizer, with again a 1:24 ratio between the HfO<sub>2</sub> cycles and the Al<sub>2</sub>O<sub>3</sub> cycles. The substrate temperature was kept at 270 °C and Ar was the inert purge gas. The TiN top electrode was then deposited onto the Al:HfO<sub>2</sub> thin film without removing the thin film from the chamber. After deposition of the top TiN electrode, the sample then underwent a rapid thermal anneal at 700 °C for 60 s in N<sub>2</sub>.

#### **3.2.4. Ion Milling**

After ALD growth, the 3D structured substrate was again prepped for photoresist using an HDMS bake, it was then spray coated using a SUSS Delta Alta Spray Coater and AZ4999 photoresist. The spray coating of photoresist enables the high aspect ratio structures to be coated uniformly. If this substrate were spin coated with photoresist instead of spray coated, the photoresist would not reach the bottom of high aspect ratio structures and it would not have a uniform thickness. After spray coating, the wafer was baked at 95 °C for 180 sec. The wafer was then exposed to a UV dosage of 125 mJ/cm<sup>2</sup> using the top electrode optical mask. The regions where top electrode was supposed to stay remained covered in photoresist, while the areas where the top electrode would be removed, were clean of photoresist. The samples then underwent a 5 minute plasma clean to ensure the removal of any remnants of photoresist in clear areas. After the clean, the samples were then inserted into a 4wave 4W-PSIBE ion mill. An ion mill removes material by accelerating Ar ions at the substrate which physically etch the substrate by knocking samples off the substrate. The top electrode pattern required that the TiN top electrode be ion milled away from a majority of the surface of the substrate. This transition is depicted in a schematic from Figure 3.10a. to Figure 3.10b. After completing the top electrode formation via

ion milling, the sample was then cleaned with a minute of sonication in acetone, followed by a rinse in methanol then isopropanol. The spray coating photolithography steps described previously were then repeated using the bottom electrode optical mask. The samples again underwent an ion mill, with the Al:HfO<sub>2</sub> thin film removed during ion milling to expose the TiN bottom electrode. This transition is represented by schematics in Figure 3.10b. to Figure 3.10c. After completing the bottom electrode ion milling process, the sample was then cleaned again by

sonicating the substrate in an acetone bath for a minute, followed by a rinse in methanol then isopropanol.

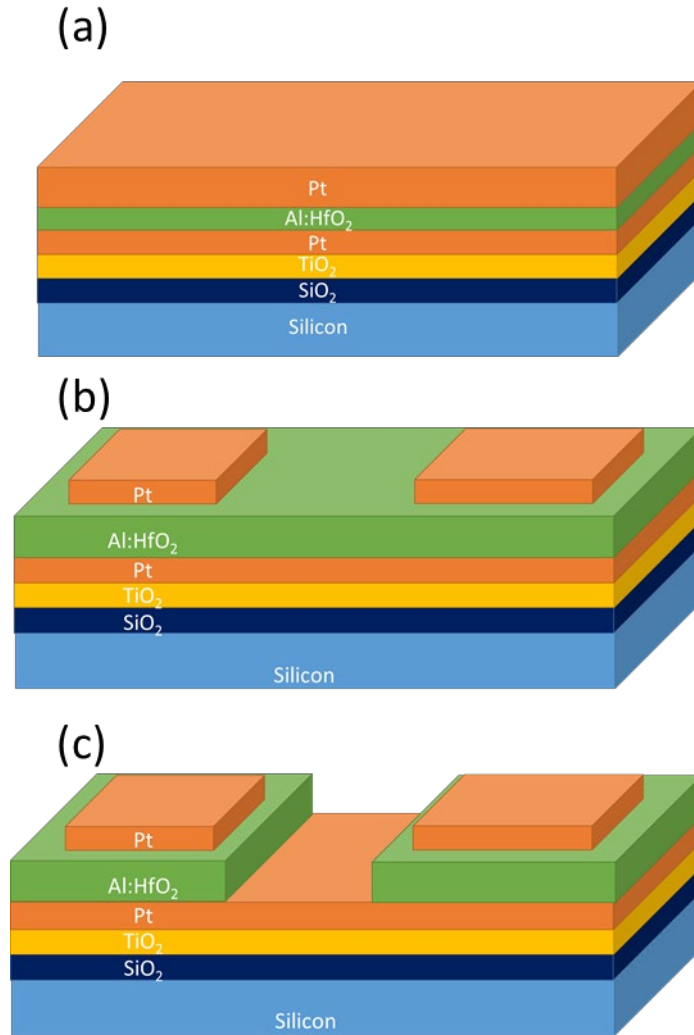


Figure 3.11. (a) Schematic of the sample layers after ALD deposition, (b) schematic of sample after defining top electrodes via ion milling, (c) schematic of sample after bottom electrode is exposed via ion milling.

### 3.2.5. Contact Pad Creation

The fourth optical mask used is the contact pad mask. This requires the 3D structured substrate to again undergo spray coating lithography steps using the contact pad optical mask. This mask is not necessary for the structures on the mask to function electrically. However, the

addition of contact pads mitigates the risk of scraping through the top or bottom electrode while attempting to electrically measure the samples as they are approximately 50 nm thick. The contact pads sputtered onto the TiN/Al:HfO<sub>2</sub>/TiN capacitors were Pt. These were also sputtered via DC Magnetron sputtering at a nominal 100 nm thick. The photoresist prevented the Pt adhering to any regions outside of the desired places over existing top and bottom electrodes. The 3D structured substrate was then sonicated for a few minutes in acetone, the photoresist along with the Pt sputtered on top of it lifted away from the surface of the 3D structured substrate, i.e. a lift-off process was used. The 3D structured substrate was then rinsed using methanol then isopropanol.

### **3.2.6. Release Etch**

The fifth and final optical mask is the released structures optical mask. The release etch was conducted with XeF<sub>2</sub>. XeF<sub>2</sub> etches Si in a highly selective isotropic manner<sup>9</sup>. The use of this process required that the sample first undergo spray coat photoresist lithography steps using the released structures optical mask. In order for the XeF<sub>2</sub> to remove the silicon underneath cantilever beams, the silicon had to be exposed, this required the sample to be ion milled. The ion milling step was required in order to mill through the Al:HfO<sub>2</sub> thin film, the TiN bottom electrode, the TiO<sub>2</sub> adhesion layer, and the 500 nm of SiO<sub>2</sub>. After ion milling the 3D structured substrates were then diced into individual 25 mm x 25 mm chips using a table saw. The individual chips were then cleaned by sonicating them in an acetone bath for 30 seconds to a minute and rinsing with methanol then isopropanol. These individual chips were then inserted into a Xactix-XeF<sub>2</sub> Isotropic Si etching system. As the XeF<sub>2</sub> release etch is dependent on surface area, depending on the amount of released structures present on an individual chip, 40-80 XeF<sub>2</sub> pulses each lasting 20 seconds at 2 Torr were required to release the cantilevers from the

substrate. The release etch was the final step in the process flow for the creation of the TiN/Al:HfO<sub>2</sub>/TiN chips. The samples were then ready to be tested.

## References

- 1 Michael S. Gaither, Frank W. DelRio, Richard S. Gates, and Robert F. Cook, *Journal of Materials Research* **26** (20), 2575 (2011).
- 2 A. Dogan, J. F. Fernandez, K. Uchino, and R. E. Newnham, presented at the ISAF '96. Proceedings of the Tenth IEEE International Symposium on Applications of Ferroelectrics, 1996 (unpublished).
- 3 M. Ramezani, M. Ghatge, and R. Tabrizian, presented at the 2018 IEEE Micro Electro Mechanical Systems (MEMS), 2018 (unpublished).
- 4 M. Ramezani, M. Ghatge, V. Felmetzger, and R. Tabrizian, presented at the 2019 IEEE MTT-S International Microwave Symposium (IMS), 2019 (unpublished).
- 5 F. Hakim, T. Tharpe, and R. Tabrizian, *IEEE Microwave and Wireless Components Letters*, 1 (2021).
- 6 Sangmin Shin, Hee Han, Yong Jun Park, Jae-Young Choi, Youngsoo Park, and Sunggi Baik, presented at the AIP Conference Proceedings, 2007 (unpublished).
- 7 K. R. Williams, K. Gupta, and M. Wasilik, *Journal of Microelectromechanical Systems* **12** (6), 761 (2003).
- 8 Younghwan Lee, H. Alex Hsain, Shelby S. Fields, Samantha T. Jaszewski, Madison D. Horgan, Patrick G. Edgington, Jon F. Ihlefeld, Gregory N. Parsons, and Jacob L. Jones, *Applied Physics Letters* **118** (1), 012903 (2021).
- 9 H. F. Winters and J. W. Coburn, *Applied Physics Letters* **34** (1), 70 (1979).

## **Chapter 4: Application Driven Characterization of Planar HfO<sub>2</sub> Films**

The majority of the text and all figures in this chapter are reprinted from [Alexis Payne, Owen Brewer, Asher Leff, Nicholas A. Strnad, Jacob L. Jones, and Brendan Hanrahan, Dielectric, energy storage, and loss study of antiferroelectric-like Al-doped HfO<sub>2</sub> thin films, Applied Physics Letters **117** (22), 221104 (2020)] with the permission of AIP Publishing<sup>1</sup>. The chapter is divided into two main sections, the first section focuses on fine tuning the voltage and energy storage density values by varying film thickness and composition. The second section of the chapter focuses on the effect the electrodes can have on Al:HfO<sub>2</sub> thin films and the origin of the AFE-like response in Al:HfO<sub>2</sub> thin films.

### **4.1. AFE-like Al:HfO<sub>2</sub> Thin Films for Energy Storage Devices**

#### **4.1.1 Planar Capacitor Production with Pt Electrodes**

AFE thin films have properties ideal for energy storage due to their lower losses compared to their ferroelectric counterparts as well as their robust endurance properties. This was previously elaborated on in section 1.1.2. In terms of energy storage capabilities, AFE/AFE-like materials have significant advantages over both linear dielectrics and ferroelectrics due to their remanent polarization being zero, or almost zero and their ability to become highly polarized at high fields.

It was critical to first produce antiferroelectric and ferroelectric thin films on planar substrates to ensure the viability of our processing steps as well as to have a benchmark against which to compare our 3D ferroelectric thin films. The planar samples produced are listed in Table 4.1.

Table 4.1. A list of the composition of the planar capacitors along with the thickness of the Al:HfO<sub>2</sub> thin films.

<b>Composition of Planar Capacitors</b>	<b>Al:HfO<sub>2</sub> Thin Film Thickness</b>
Si/SiO <sub>2</sub> /TiO <sub>2</sub> /Pt/ 4 at% Al:HfO <sub>2</sub> /Pt	20 nm
Si/SiO <sub>2</sub> /TiO <sub>2</sub> /Pt/ 4 at% Al:HfO <sub>2</sub> /Pt	50 nm
Si/SiO <sub>2</sub> /TiO <sub>2</sub> /Pt/ 8 at% Al:HfO <sub>2</sub> /Pt	20 nm
Si/SiO <sub>2</sub> /TiO <sub>2</sub> /Pt/ 8 at% Al:HfO <sub>2</sub> /Pt	50 nm

The planar 4 at% Al:HfO<sub>2</sub> and 8 at% Al:HfO<sub>2</sub> thin films were produced by on a Si substrate with 500 nm of thermally grown SiO<sub>2</sub>. Ti adhesion layer was sputtered and then oxidized to form a 32 nm thick TiO<sub>2</sub> layer. Both the Pt top electrode and bottom electrodes were sputtered using DC magnetron sputtering. The Al:HfO<sub>2</sub> thin films were grown using a Kurt Lesker ALD 150-LX system. The precursors used were TDMAH and TMA with H<sub>2</sub>O as the oxygen precursor. The substrate was heated at 250 °C with Ar as the inert purge gas. The ratio of Al<sub>2</sub>O<sub>3</sub> cycles was 1:24 for the 4 at% Al:HfO<sub>2</sub> thin film and 2:23 for the 8 at% Al:HfO<sub>2</sub> thin film. The thin films were grown using a deposition, anneal, deposition, anneal (DADA) process. ALD growth began with an initial deposition ranging from 1-2 nm thick. The substrate was then removed from the ALD chamber and exposed to a rapid thermal anneal (RTA) at 300 °C for 60 seconds in N<sub>2</sub>. This process was found to improve reliability which could be due to the removal of volatile organics at the Pt/Hf interface. Growth was then continued on the annealed sample. Once the film finished growth, the thickness was confirmed with ex-situ ellipsometry and matched the expected thicknesses, 20 nm or 50 nm, based on the standard growth rates of Al<sub>2</sub>O<sub>3</sub> and HfO<sub>2</sub>. The ALD growth chamber used was a commercial Kurt J. Lesker Company, Inc. (Jefferson Hills, PA,

USA) ALD 150-LX platform. The top electrodes were then defined using conventional photolithography followed by a lift-off process, described in section 3.2.1. For all growths, the samples underwent RTAs at temperatures ranging from 300 °C- 900 °C. Annealing conditions of 700 °C for 60 seconds in N<sub>2</sub> were found to provide the best energy storage properties for the Al:HfO<sub>2</sub> capacitors, the subsequent measurements and analysis were conducted on the 700 °C annealed thin films.

#### 4.1.2 Structural Characterization

GIXRD data were taken for each 700°C annealed thin film sample using a Panalytical XRD system. For the GIXRD, the incident angle was set at 2.0°, with the data collected over a range 10°-90° for 2θ. As previously noted, AFE-like behavior in Si or Al doped Hf<sub>0.5</sub>Zr<sub>0.5</sub>O<sub>3</sub> has been attributed to an electric field induced phase transition between the non-polar t-phase and the polar o-phase<sup>2</sup>. Comparing the GIXRD patterns from various dopants and thicknesses, differences occur in the region of 28°-33° (Fig. 4.1b.). The peak with highest intensity in the o-phase is the 111 peak near 30°, which all samples show. This also could be the 101 peak of the t-phase or a combination thereof. Distinguishing between these two phases is non-trivial without a high resolution measurement, either via x-ray or another technique. However, the 4 at% Al:HfO<sub>2</sub> thin film samples have two other peaks, at ~ 29° and ~ 32°, which correspond to the monoclinic  $\bar{1}11$  and 111. The GIXRD clearly shows the 4 at% Al: HfO<sub>2</sub> thin films to contain some m-phase present, which is not present in the 8 at% Al:HfO<sub>2</sub> thin films.

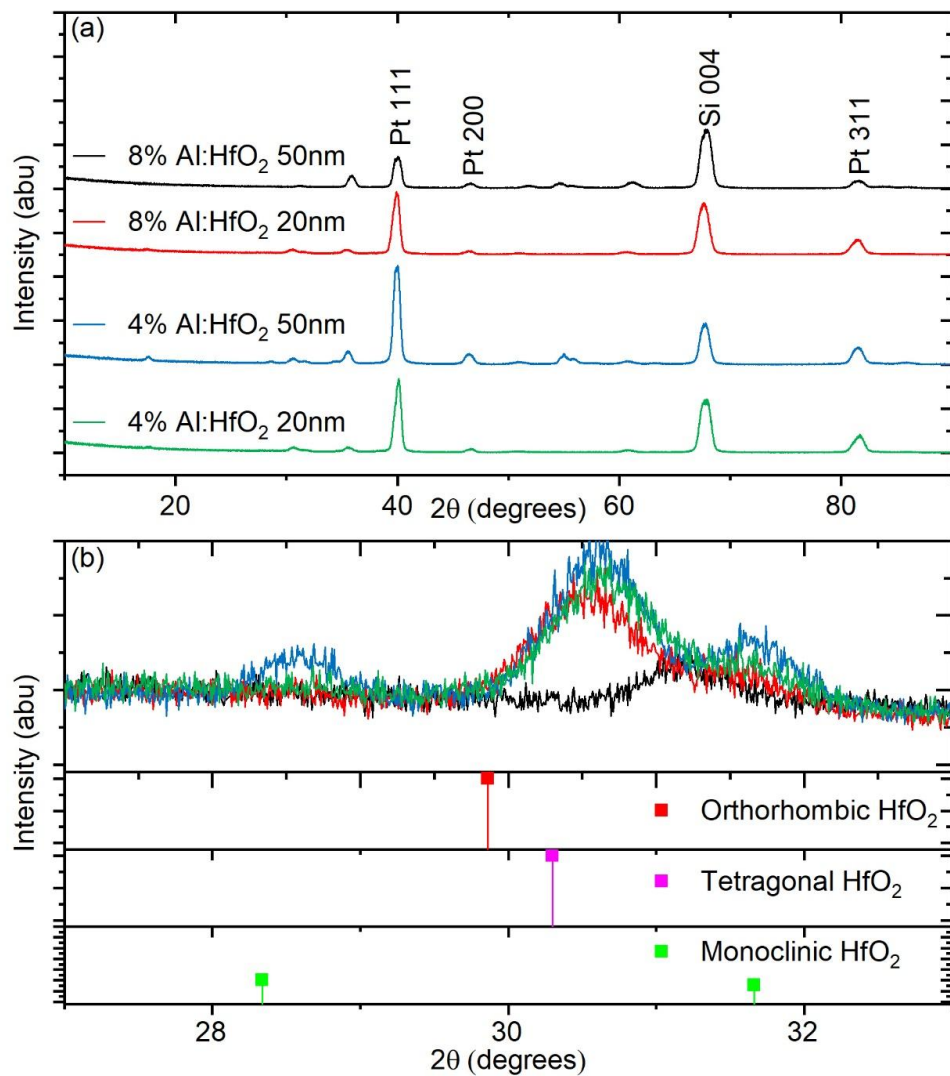


Figure 4.1. (a) GIXRD of all four Al:HfO<sub>2</sub> compositions, (b) around largest intensity orthorhombic/tetragonal peak and monoclinic peaks between 27°-33°.

#### 4.1.3. Energy Storage Density and Efficiency

Electrical characterization of the capacitors was performed using a *Radiant Technologies Precision Premier II*. Figure 4.2a. shows the pristine polarization vs. electric field (PE) loops for the sample set. The maximum electric field applied was 75% of breakdown ( $0.75E_{BD}$ ) at a frequency of 2 kHz. Thus, for the 4 at% Al:HfO<sub>2</sub> films voltages of 4 V and 10.8 V were applied

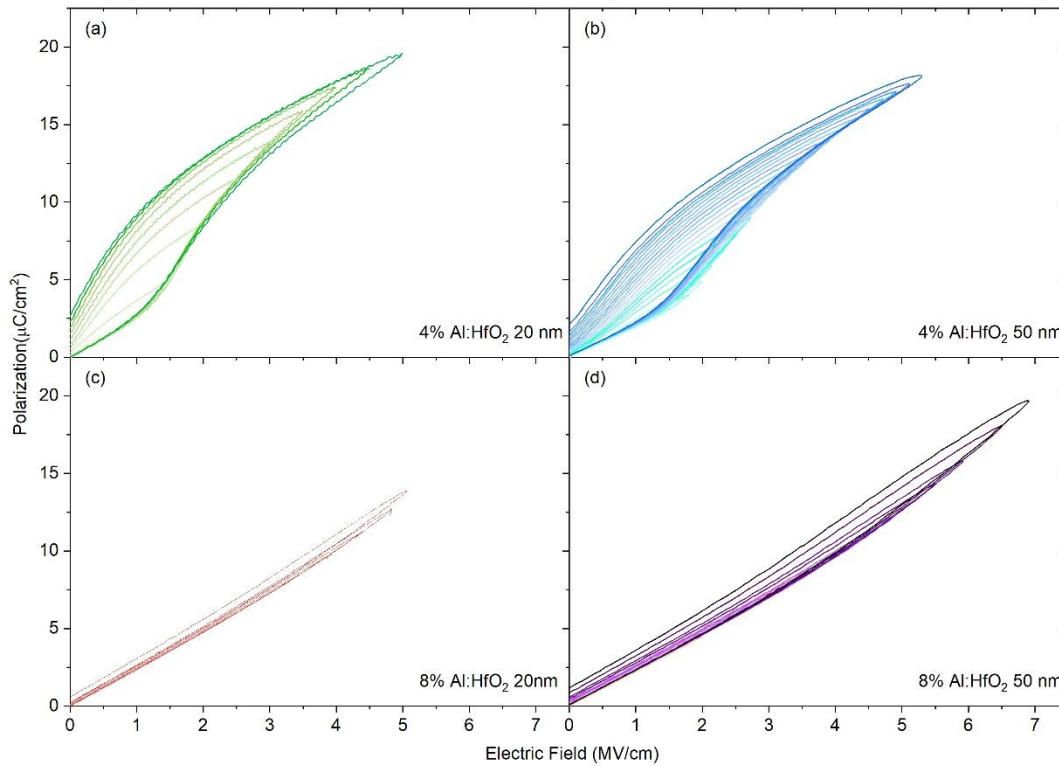


Figure 4.2. Monopolar loops taken at increasing fields for (a) 4 at% Al:HfO<sub>2</sub> 20 nm (b) 4 at% Al:HfO<sub>2</sub> 50 nm (c) 8 at% Al:HfO<sub>2</sub> 20 nm (d) 8 at% Al:HfO<sub>2</sub> 50 nm for the calculation of energy storage density values (d) shows only intermittent loops due significantly overlapping curves.

to the 20 nm thin film and 50 nm thin film respectively. The 8 at% Al:HfO<sub>2</sub> 20 nm thin films had 4.4 V applied, and the 8 at% 50 nm thin films had 14 V applied. Each ESD was calculated from a series of monopolar P-E loops (Figure 4.2.), each loop was taken at sequentially increasing fields until the device experienced breakdown. A monopolar loop was used instead of the typical bipolar loop as it is more relevant to high output power applications such as pulsed power technology. The shape of the loop plays a significant role in the ESD and  $\eta$  values of the thin films. The 8 at% Al:HfO<sub>2</sub> P-E loops shown in Figure 4.3a. reach similar maximum polarization values as the 4 at% Al:HfO<sub>2</sub> loops while staying slimmer than the 4 at% Al:HfO<sub>2</sub> loops at those high fields. This leads to an increase in both ESD and efficiency for the slimmer loop 8 at%

Al:HfO<sub>2</sub> samples compared to their 4 at% Al doped counterparts. With the 4 at% Al:HfO<sub>2</sub> 20 nm thin films, the efficiency dips and then rises again due the maximum polarization increasing faster than remanent polarization in the range of 2-5MV/cm (Figure 4.3b.).

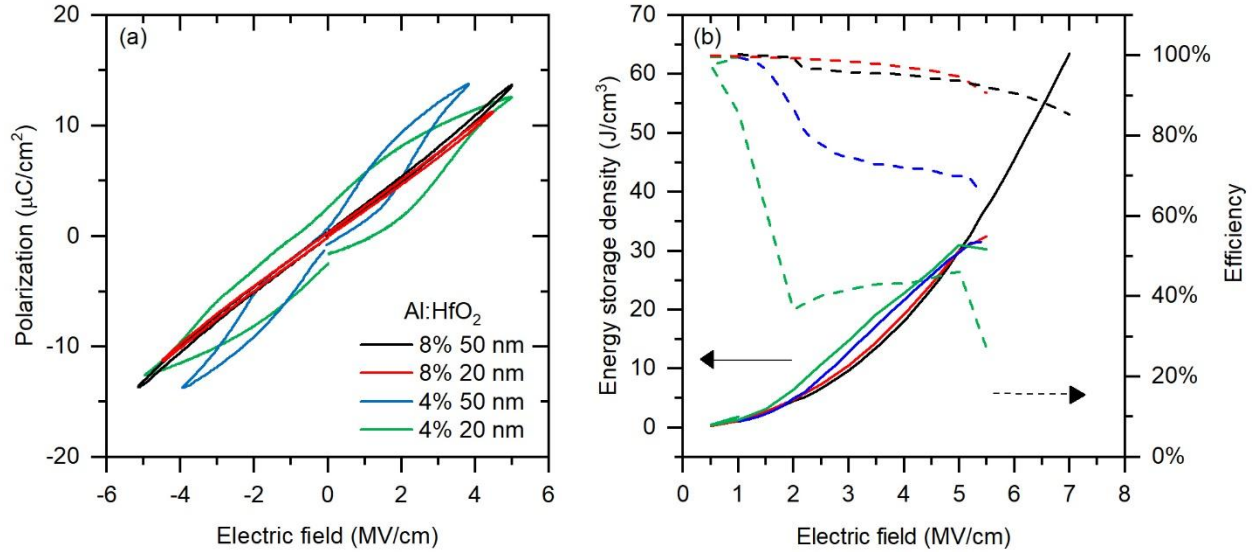


Figure 4.3. (a) Polarization versus electric field loops of thin film Al:HfO<sub>2</sub> of various compositions and thicknesses at 75% $E_{BD}$  and (b) ESD and  $\eta$  calculations with increasing applied field.

Unexpectedly, an increase in thickness yielded higher breakdown fields for both compositions, resulting in higher ESD potential. This is likely due to a reduction in the number of through thickness grain boundaries, as the 20 nm thin films could be nominally 1 grain thick,<sup>36</sup> while the 50 nm samples have more grains resulting in less through thickness grain boundaries.

The relative importance of  $\eta$  versus ESD should be re-evaluated when considering the application perspective. The energy lost in the system will dissipate as heat, which could pose as a challenge for many applications. Consider the record high energy density of 450  $\mu\text{J}/\text{cm}^2$  obtained by Kühnel et al. for an area-enhanced AFE Si:HfO<sub>2</sub> film was 67% efficient<sup>3</sup>. Supposing the capacitor is used in a pulsed power application and is providing power pulses at 10 kHz, it will have to dissipate  $\sim 15 \text{ W}/\text{cm}^2$  at minimum which means device-level energy density will be

reduced by some volume dedicated to thermal management. For capacitors which are heat-sunked to a Si substrate this cooling requirement is not an issue, but in a device where the energy storage material makes up a sizeable fraction of the total volume, thermal changes will arise. Thermal requirements will scale linearly with frequency which could go to MHz levels for radio applications. The 8 at% Al:HfO<sub>2</sub> compositions have lower energy storage densities at a given voltage, but the extremely slim, efficient hysteresis loops could prove to be higher performance from an application perspective.

#### 4.1.4. Operating Voltage, Breakdown Voltage, Reliability

Figure 4.4. describes the dielectric breakdown distribution within the tested sample set. The Weibull modulus ( $\beta$ ) refers to the reliability of the devices.<sup>38</sup> How the Weibull distribution is

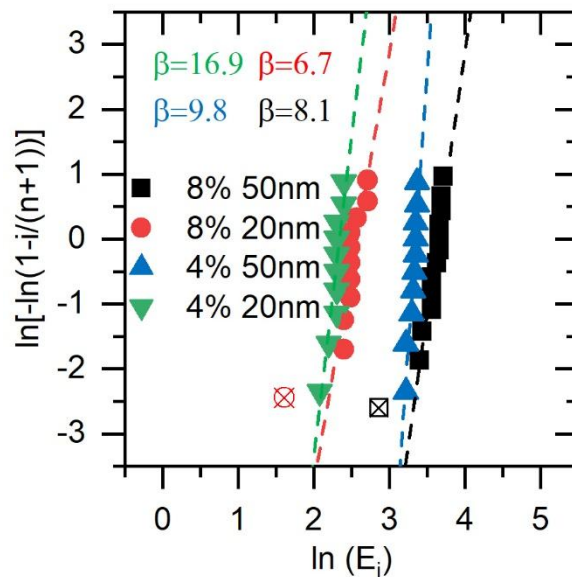


Figure 4.4. Weibull distribution of breakdown field for each Al:HfO<sub>2</sub> sample with the Weibull modulus listed for each one. The x'd data points were excluded from calculations as they suffered from early “infant mortality” failure.

calculated was previously defined in 2.2.7. At least 10 data points were taken for each film. The Weibull modulus ( $\beta$ ), is the slope of linear-fitted curves in the Weibull distribution and provides a metric of device reliability<sup>4</sup>. A high  $\beta$  indicates a narrow distribution of breakdown strengths

for a set of samples. Thus, high moduli are desired as they indicate that samples are more predictable and less likely to breakdown at lower voltages. The  $\beta$  values calculated in Figure 4.4. shows that 4 at% Al-doped HfO<sub>2</sub> samples have a narrower distribution of breakdown strengths than that of the 8 at% Al-doped HfO<sub>2</sub> samples, with moduli of 9.8 and 16.9 vs. 8.1 and 6.7. Full, cross wafer analysis would be needed to fully establish the reliability of the breakdown strength for the various compositions.

An operating voltage is assumed for each sample based on the general rule of thumb where  $V_{op} \sim 0.25 * E_{BD}$ . The ESD and  $\eta$  for the  $V_{op}$  are shown in Table 4.2. The  $V_{BD}$  for the thin films are listed as well. Comparing these thin films at theoretical operating voltages shows that their energy storage efficiencies would all be above 89%. The higher  $V_{BD}$  of the 8 at% Al:HfO<sub>2</sub> results in it having the highest theoretical  $V_{op}$  and subsequently the highest ESD values at operating voltage while still maintaining a higher  $\eta$  than either 4 at% Al-doped samples at  $V_{op}$ . Subsequent characterizations are performed above the estimated  $V_{op}$  showing the reliability of these devices even at higher levels.

Table 4.2. Electrical characteristics of Al:HfO<sub>2</sub> Capacitors

Sample	$V_{BD}$ [V]	$V_{op}$ [V]	ESD @ $V_{op}$ [J cm <sup>-3</sup> ]	$\eta$ @ $V_{op}$
4 at% Al:HfO <sub>2</sub> 20 nm	10	2	1.306	89%
4 at% Al:HfO <sub>2</sub> 50 nm	27	6	1.419	99%
8 at% Al:HfO <sub>2</sub> 20 nm	11	2	1.166	100%
8 at% Al:HfO <sub>2</sub> 50 nm	35	8	2.865	100%

The thin films underwent endurance cycling at 10 kHz at 40%  $E_{BD}$  and no wake-up effect was observed up to  $10^7$  cycles for the 4 at% 50 nm Al:HfO<sub>2</sub> and the 8 at% Al:HfO<sub>2</sub> samples. The  $P_r$  as well as  $P_{max}$  should little to no change with cycling with a triangular waveform as shown in Figure 4.5. However, the 4 at% 20 nm Al:HfO<sub>2</sub> sample had a significantly higher  $P_r$  upon initial measurement, which continued to increase with cycling, it also only endured  $10^6$  cycles at 10 kHz at 40%  $E_{BD}$ .

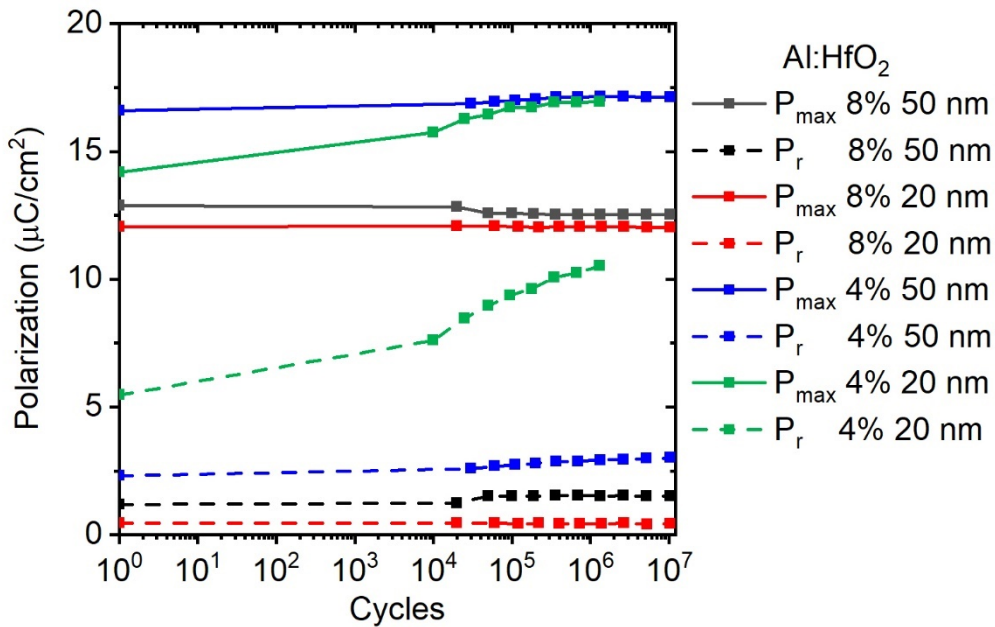


Figure 4.5. The endurance of the Al:HfO<sub>2</sub> films cycled at 40% of  $E_{BD}$  up to  $10^6$ - $10^7$  cycles with a triangular waveform. How the  $P_r$  (dashed) and  $P_{max}$  (solid) change over this range of cycling is shown.

Permittivity and loss tangent were measured with bias and frequency using a small AC signal set up using a Keysight/Agilent 4192A LF Impedance Analyzer. The bias dependence in Figure 4.6a. shows the loss tangent remains below 2% for all samples under varying field. A positive slope of  $d\epsilon_r/dE$  can be observed for both 8 at% Al-doping samples, with the 50 nm showing a double loop, confirming AFE-like behavior. Figure 4.6b. shows the frequency

dependence ranging from 100 Hz to 100 kHz revealing flat permittivity and low loss through the range of tested frequencies.

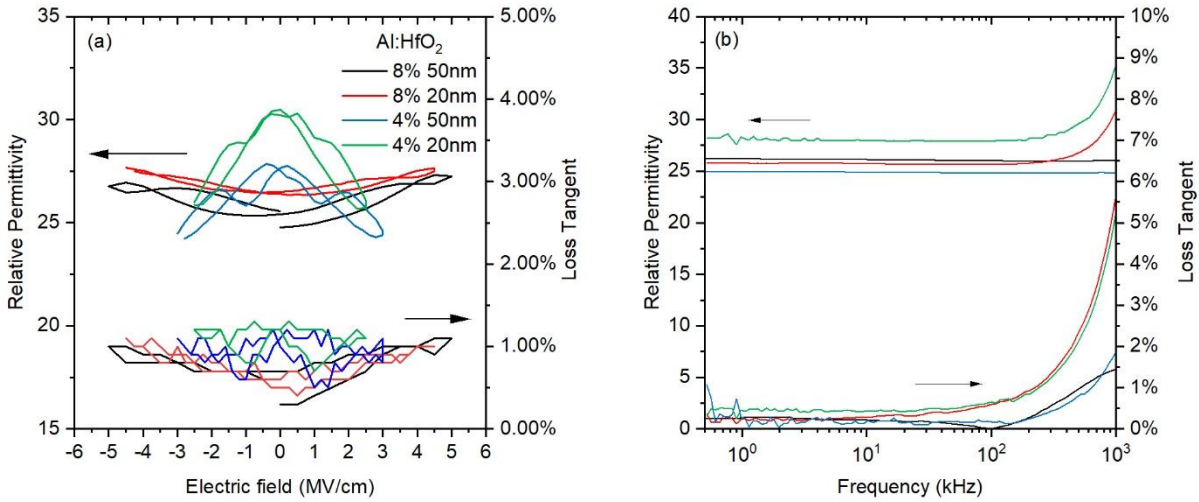


Figure 4.6. The relative dielectric permittivity and loss tangent vs. electric field (a) and frequency(b) for the Al:HfO<sub>2</sub> thin films.

An explanation for the low loss tangent values in the Al:HfO<sub>2</sub> thin films could be due to a low concentration of defects. Many Hf-based thin films on initial application of electric field exhibit a pinched P-E loop. However, upon further cycling the  $P_r$  increases, this phenomenon is known as the wake-up effect<sup>5-9</sup>. Lomenzo et al. and Zhou et al. both attributed the wake-up effect in Si:HfO<sub>2</sub> to the movement oxygen vacancies, which are believed to act as pinning sites for domain wall motion<sup>5,6</sup>. Furthermore, these vacancies were thought to have been induced by the oxidation of the TiN bottom electrode during growth<sup>5,6</sup>. Zhang et al. showed Al:HfO<sub>2</sub> thin films with TiN electrodes also experience wake-up and an irradiated set of films experienced an even faster wake up due to radiation induced defects, predominantly oxygen vacancies<sup>10</sup>. The effect electrodes have on oxygen vacancy concentration in undoped HfO<sub>2</sub> has also been explored, with Pt electrodes showing to induce less than TiN<sup>11</sup>. This is due to Pt having a lower oxygen affinity than TiN. The bottom electrodes for the samples in this work were Pt. The  $P_r$  values not showing

increases over  $1 \mu\text{C}/\text{cm}^2$  for up to  $10^4$  cycles give credence to a lower oxygen vacancy concentration, resulting in the low loss tangent values. Another parameter shown to depend on defect concentration is leakage current<sup>12,13</sup>. The leakage current of our thin films being measured to be  $< 10 \mu\text{A}/\text{cm}^2$  up to  $3 \text{ MV}/\text{cm}$  for each composition, again suggests a low defect concentration in the Al:HfO<sub>2</sub> thin films.

In conclusion, Al-doped HfO<sub>2</sub> thin films with Pt electrodes of varying dopant concentration (4 at% or 8 at%) and varying thickness (20 nm or 50 nm) were studied using an energy storage application driven methodology. The P-E loops of the Al:HfO<sub>2</sub> thin films revealed the 8 at% Al-doped samples had slimmer loops than that of the 4 at% Al:HfO<sub>2</sub> thin films. Thus, the 8 at% Al:HfO<sub>2</sub> samples had higher  $\eta$  values at equal applied fields than the 4 at% Al:HfO<sub>2</sub> samples. The 8 at% Al:HfO<sub>2</sub> samples could also withstand higher fields resulting in a maximum value of  $63 \text{ J}/\text{cm}^3$  with an efficiency of 85% for the 50 nm sample. As much as ESD values are reported, this study shows that considerations must be made not only to ESD, but also to  $E_{BD}$  and equally to  $V_{op}$ . In considering the eventual commercial use of these devices, the 8 at% Al:HfO<sub>2</sub> 50 nm sample showed the most promise with its ability withstand higher voltages and thus have higher ESD ( $2.865 \text{ J}/\text{cm}^3$ ) and  $\eta$  (100%) at  $V_{op}$  (8 V). The loss tangent values of our Al-doped HfO<sub>2</sub> thin films were the lowest recorded to date for HfO<sub>2</sub>-based thin films at under 2%. The loss tangent also remained below 2% over a frequency range of 4 orders of magnitude (100 Hz to 100 kHz). The reliability study of the  $E_{BD}$  of the samples showed the  $E_{BD}$  of the 4 at% Al:HfO<sub>2</sub> thin film was more consistent from device to device than the 8 at% Al:HfO<sub>2</sub> thin films. However, the 8 at% Al:HfO<sub>2</sub> still had narrow spreads of  $E_{BD}$  as indicated by  $\beta \geq 6$ . A holistic consideration of energy storage density and efficiency, combined with rarely measured loss

tangent values provide guidance for materials in energy storage applications, highlighting the potential of high at% Al:HfO<sub>2</sub>.

## **4.2. Thermal Stability of AFE-like Al:HfO<sub>2</sub> with Pt or TiN electrodes**

### **4.2.1 Polarization Electric Field Loops vs. Temperature**

As previously noted in 2.2.7, as much as HfO<sub>2</sub>-based thin films are experiencing initial commercial success, the temperature sensitivity of the electrical properties such as the loss tangent and leakage current remain unreported. However, initial temperature studies of these materials have revealed AFE HfO<sub>2</sub> -based thin films to have promising thermal stability<sup>2,14</sup> in comparison to other model AFE thin film materials<sup>15,16</sup>. reported. Prior works have also not considered the effect of electrode material on the temperature stability of HfO<sub>2</sub> based thin films. Yet, the applicability of numerous other electrodes to HfO<sub>2</sub> thin films have been demonstrated such as HfN<sup>17</sup>, TaN<sup>5,18</sup>, as well as metals such as Ni<sup>19</sup>, Pd<sup>19</sup>, and Pt<sup>1,19</sup>, resulting in variations in properties such as  $P_r$  and phase composition. Newly reported results of the temperature stability of the loss tangent and leakage current using alternative electrodes, such as Pt, would further expand the design options for device architectures in which these films can be utilized. Not only would such measurements validate the ability of these materials to maintain low leakage current and loss tangent values at high temperatures, new investigations of the dielectric losses versus temperature could also broaden the understanding of the driving mechanism for the AFE-like response that is realized in certain types of HfO<sub>2</sub> thin films.

The samples compared in this section are a Si/SiO<sub>2</sub>/TiO<sub>2</sub>/Pt/ 50 nm 4 at% Al:HfO<sub>2</sub>/Pt, the production of which was previously described in 4.1.1 and a Si/TiN/ 50 nm 4 at% Al:HfO<sub>2</sub>/TiN. the production was previously described in 3.2.3. The P-E loops and leakage current were measured using a *Radiant Technologies Precision Premier II*. The samples were mounted in a

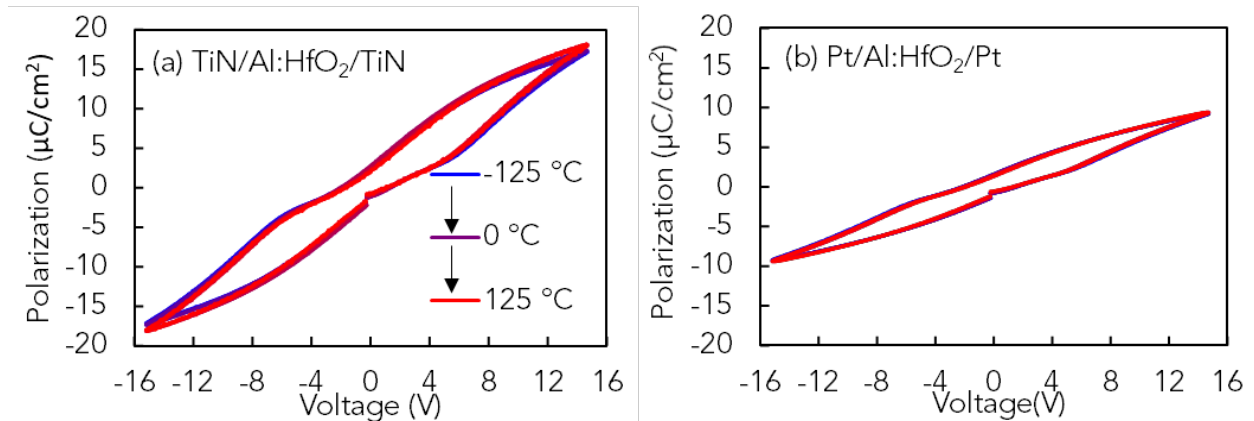


Figure 4.7. P-E loops of (a) TiN/ 50 nm 4 at % Al:HfO<sub>2</sub>/TiN and (b) Pt/ 50 nm 4 at% Al:HfO<sub>2</sub>/Pt from -125 °C to 125 °C at 25 °C steps.

Lake Shore PS-100 tabletop probe station with a liquid nitrogen cooled temperature-controlled stage. The samples were mounted to the stage using thermal grease. The samples were cooled to -125 °C and individual P-E loop measurements, ESD measurements, as well as leakage current measurements were made every 25 °C up to 125 °C. A 15 V bipolar P-E loop was measured at 1 kHz, a monopolar hysteresis loop was measured at 1 kHz to calculate ESD and efficiency of the device at 15 V, and the current-voltage (IV) measurement was conducted using a 5 V switched linear waveform with 1000 ms soak time. The resultant P-E loops at increasing temperature are presented in Figure 4.7. The  $P_r$  and maximum polarization ( $P_{max}$ ) remain stable with increasing temperature. The  $P_{max}$  at positive voltage of the TiN/Al:HfO<sub>2</sub>/TiN increased by 0.97  $\mu\text{C}/\text{cm}^2$  from -125 °C to 125 °C,  $P_r$  decreased by 0.87  $\mu\text{C}/\text{cm}^2$  from -125 °C to 125 °C. The  $P_{max}$  of Pt/Al:HfO<sub>2</sub>/Pt increased by 0.24  $\mu\text{C}/\text{cm}^2$  and the  $P_r$  decreased by 0.27  $\mu\text{C}/\text{cm}^2$  from -125 °C to 125 °C. The stable  $P_r$  in both samples suggest that the driving mechanism for the AFE-like response in these samples is not affected by temperature. This result differs from prior work on Si:HfO<sub>2</sub> samples which demonstrated a more significant increase in  $P_r$  with decreasing temperature<sup>20,21</sup>. The authors of those prior works attributed the increase in  $P_r$  to an increase in

the orthorhombic phase<sup>20,21</sup>. Here, both Pt/Al:HfO<sub>2</sub>/Pt and TiN/Al:HfO<sub>2</sub>/TiN capacitors do not exhibit a substantial increase in  $P_r$  with decreasing temperature, suggesting that the orthorhombic phase fraction does not change as a function of decreasing temperature.

#### 4.2.2. GIXRD Patterns

While both samples demonstrate similar temperature stability, there is a clear difference in the  $P_{max}$  that is achieved between the Pt/Al:HfO<sub>2</sub>/Pt capacitors and the TiN/Al:HfO<sub>2</sub>/TiN capacitors which can be explained by considering the effect of the bottom electrode on the ferroelectric layer. Park et al. found that the use of (111)-textured Pt bottom substrates resulted in the formation of (111)-textured Hf<sub>0.5</sub>Zr<sub>0.5</sub>O<sub>2</sub>(HZO)<sup>22</sup>. (111)-textured HZO was found to suppress the phase transformation from tetragonal to orthorhombic due to unfavorable orientation of the tetragonal cell during annealing. Such an orientation caused an equivalent tensile strain state across a-, b-, and c- axes which did not promote the formation of the orthorhombic phase. The larger o111/t011 peak intensity of the TiN/Al:HfO<sub>2</sub>/TiN capacitors relative to that of the

Pt/Al:HfO<sub>2</sub>/Pt capacitors in the GIXRD pattern, Figure 4.8., suggests that the TiN/Al:HfO<sub>2</sub>/TiN

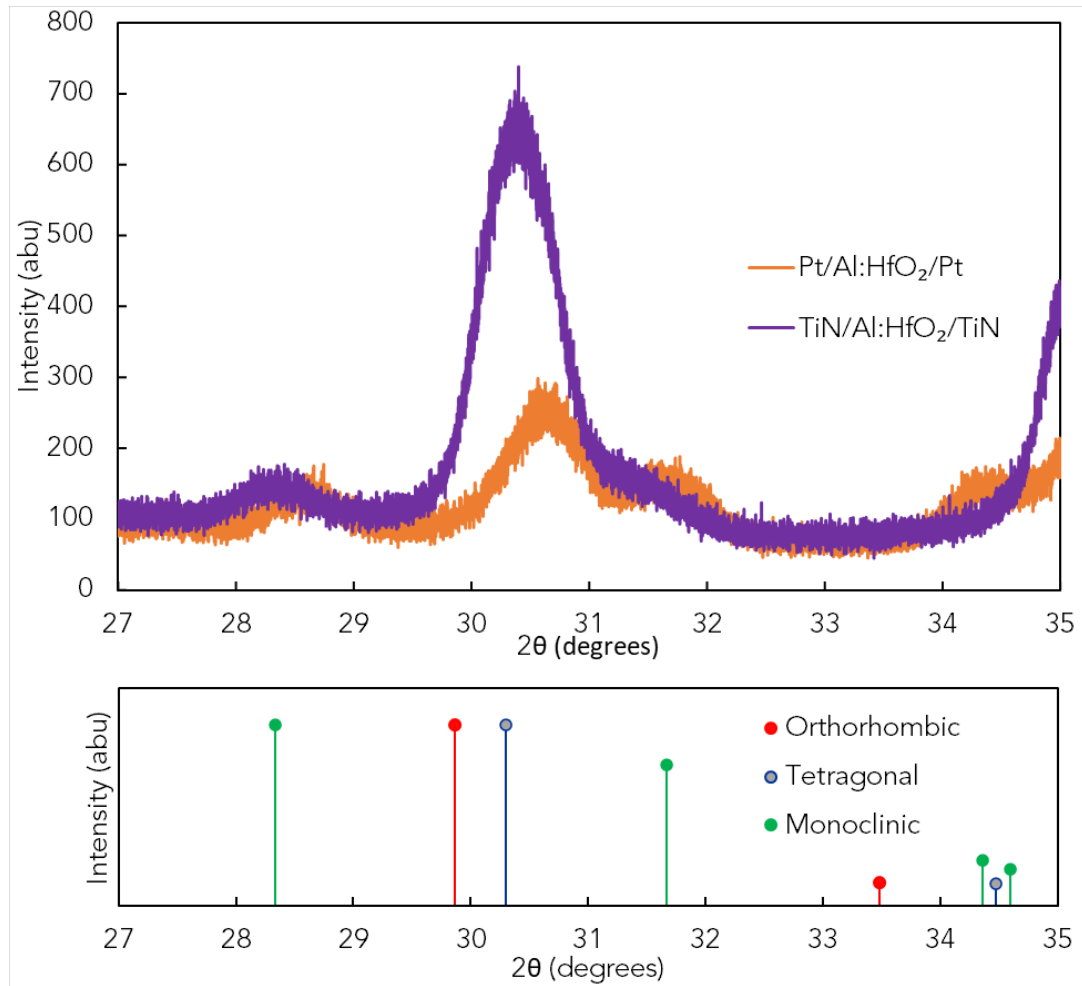


Figure 4.8. GIXRD patterns of TiN/ 50nm 4 at% Al:HfO<sub>2</sub>/TiN and Pt/ 50nm 4 at% Al:HfO<sub>2</sub> with reference XRD patterns for the orthorhombic phase (PDF 04-005-559), the tetragonal phase (04-011-882), and the monoclinic phase (PDF 00-034-0104) shown below.

capacitors have a higher orthorhombic phase fraction than the Pt/Al:HfO<sub>2</sub>/Pt capacitors. Prior work showed the TiN/Al:HfO<sub>2</sub>/TiN capacitors fabricated via SNAP have a clean chemical interface with a diminished TiO<sub>x</sub>N<sub>y</sub> layer and carbon impurities at the electrode interfaces

leading to enhanced  $P_{max}$  values<sup>23</sup>. The  $TiO_xN_y$  layer typically acts as a dead layer that reduces the ferroelectric response of a material.

#### 4.2.3. ESD, Efficiency, and Losses

The stability of the ESD and efficiency of the samples vs. temperature is shown in Figure 4.9. with the  $TiN/Al:HfO_2/TiN$  capacitor having a higher ESD at  $18.17 \pm 0.79 \text{ J/cm}^3$  than the

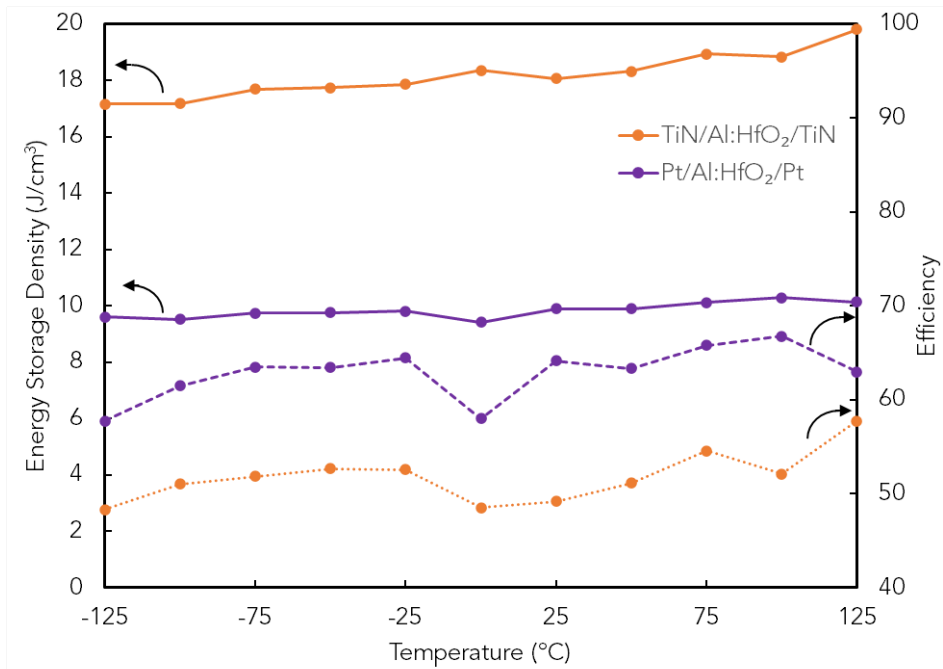


Figure 4.9. ESD and efficiency values measured calculated from 15 V monopolar hysteresis loops taken every 25 °C from -125 °C to 125 °C.

$Pt/Al:HfO_2/Pt$  at  $9.83 \pm 0.26 \text{ J/cm}^3$ . However, due to the larger hysteresis of P-E loop of  $TiN/Al:HfO_2/TiN$ , it exhibits efficiency of  $51.79 \pm 2.75\%$ , which is ~10% lower at all

temperatures relative to the Pt/Al:HfO<sub>2</sub>/Pt of  $62.87 \pm 3.00\%$ . Figure 4.10. shows the leakage

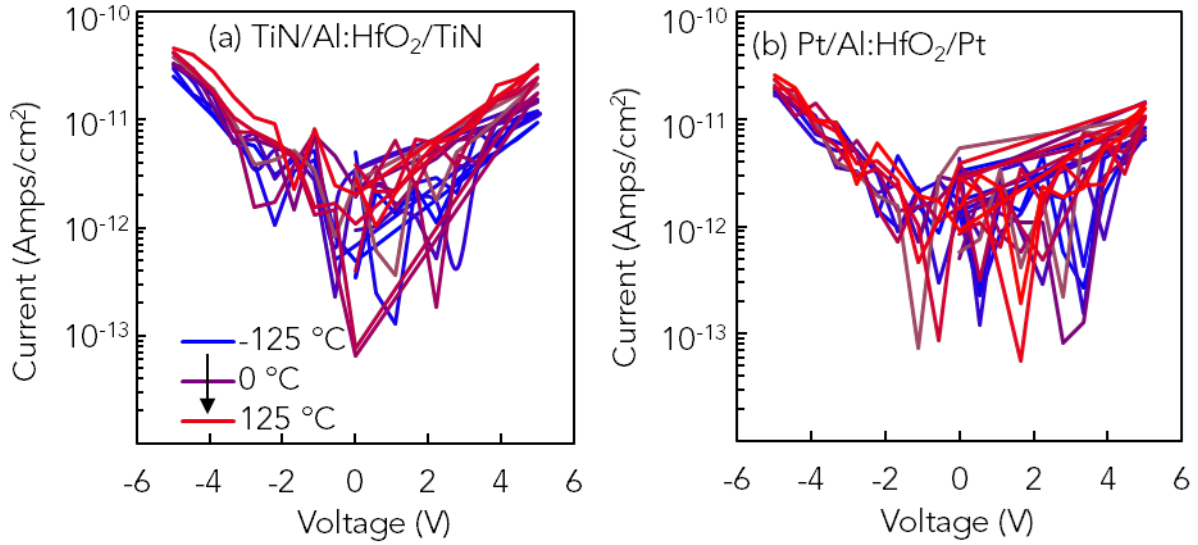


Figure 4.10. Leakage current measurements of (a) TiN/50 nm 4 at% Al:HfO<sub>2</sub>/TiN sample and (b) Pt/50 nm 4 at% Al:HfO<sub>2</sub>/Pt at temperatures from -125 °C to 125 °C at 25 °C intervals.

current of both samples with increasing temperature. The leakage current values of  $10^{-13}$ - $10^{-10}$  A/cm<sup>2</sup> are lower than values previously reported for other AFE thin films such as PZO ( $10^{-3}$  A/cm<sup>2</sup>)<sup>24</sup>, (Pb<sub>0.92</sub>La<sub>0.08</sub>)(Zr<sub>0.65</sub>Ti<sub>0.35</sub>)O<sub>3</sub> ( $10^{-4}$  A/cm<sup>2</sup>)<sup>25</sup>, and our own PHO ( $10^{-8}$  A/cm<sup>2</sup>)<sup>16</sup>. The thermal stability of the leakage current densities of the Al:HfO<sub>2</sub> capacitors also provides a significant benefit over current bulk capacitors such as tantalum capacitors and multilayer

ceramic capacitors (MLCCs) which are known to have increases of two orders of magnitude or more in leakage current over the full military temperature range (-55 °C to 125 °C).<sup>26</sup>

The capacitance and loss tangent values were also measured from -125 °C to 125 °C at 25 °C intervals using an HP4192a Impedance Analyzer with the Lakeshore probe station with temperature-controlled stage and is shown in Figure 4.11. The loss tangent is a measure of the

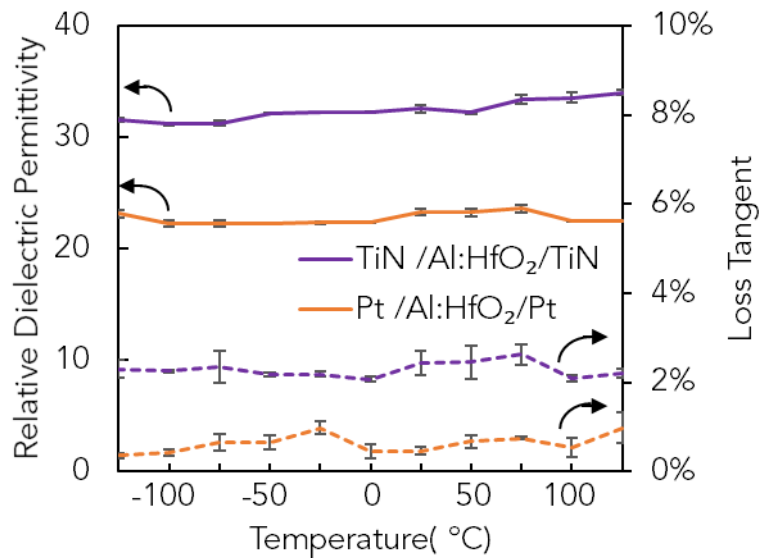


Figure 4.11. Relative permittivity and loss tangent values of TiN/ 50 nm 4 at% Al:HfO<sub>2</sub>/TiN and Pt/ 50 nm 4 at% Al:HfO<sub>2</sub>/Pt from -125 °C to 125 °C at 25 °C steps.

alternative current (AC) losses in a material due to the movement of atoms or molecules. The loss values remained below 0.03 for both TiN/Al:HfO<sub>2</sub>/TiN and Pt/Al:HfO<sub>2</sub>/Pt at all measured temperatures. The capacitance measurements were used to calculate the relative dielectric permittivities, as well as determine the temperature coefficient of capacitance (TCC) for each of the samples. The TCC was calculated from the slope of the linear fit of the data. The Pt/Al:HfO<sub>2</sub>/Pt capacitor proved to have a lower relative dielectric permittivity of 23.30 at 25 °C but also a lower TCC of 78 ±86 ppm/ °C. The TiN/Al:HfO<sub>2</sub>/TiN capacitor had a relative dielectric permittivity of 33.70 with a larger TCC of 320 ppm/°C. Figure 4.11. shows an average

of four measurements taken every 25 °C at 10 kHz with an AC signal of 0.1 V with 0 V bias. A series of capacitance vs. frequency measurements were also made every 25 °C. The relative dielectric permittivity calculated from frequencies ranging from 1 kHz to 1000 kHz with increasing temperature is shown in Figure 4.12. The capacitance of TiN/Al:HfO<sub>2</sub>/TiN varied less

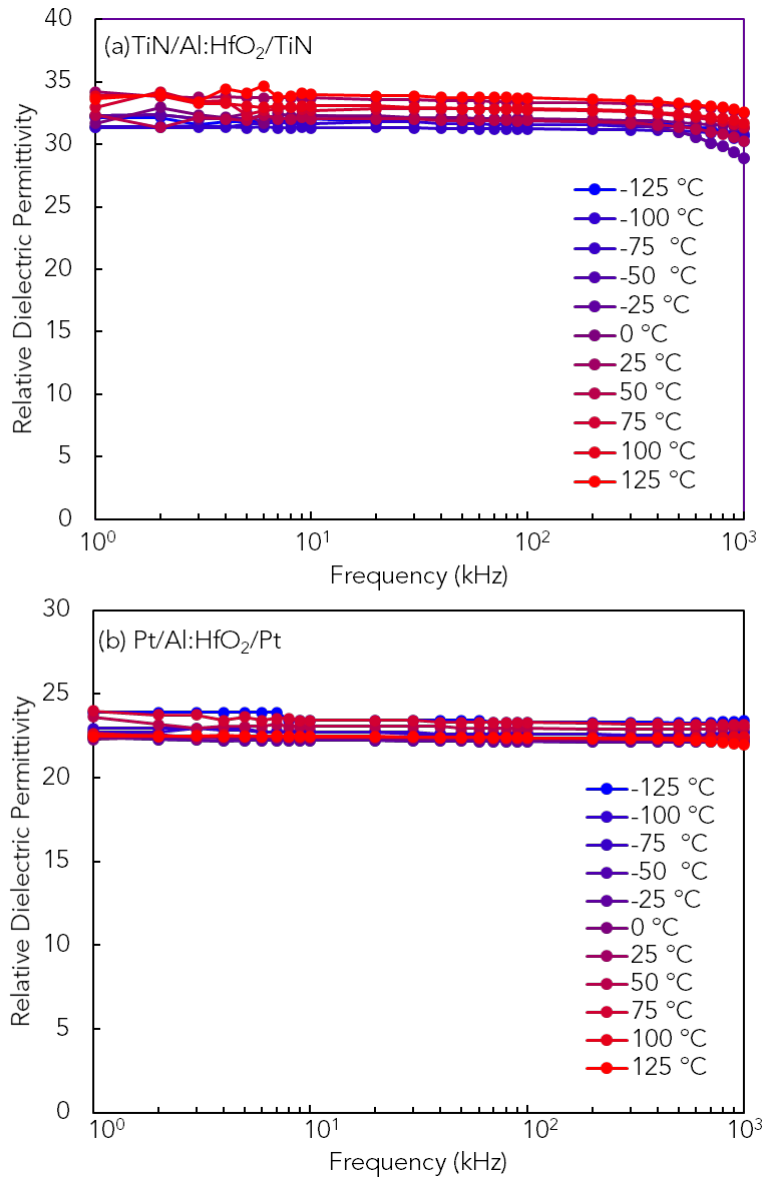


Figure 4.12. Dielectric permittivity vs. frequency of (a) TiN/50 nm 4 at% Al:HfO<sub>2</sub>/TiN sample and (b) Pt/50 nm at% Al:HfO<sub>2</sub>/Pt taken every 25 °C from -125 °C to 125 °C.

than 6% at all frequencies and temperatures, while the capacitance of the Pt/Al:HfO<sub>2</sub>/Pt capacitor varied less than 5% for all frequencies and temperatures measured.

#### 4.2.4. Endurance Cycling

Endurance cycling measurements using a 15 V square waveform at 5 kHz were conducted on individual capacitors at -125 °C, 25 °C, and 125 °C. The variability in the starting  $P_r$  at each respective temperature is attributed to the variability from capacitor to capacitor. A P-E loop and a leakage current measurement was taken before and after the endurance cycling. The

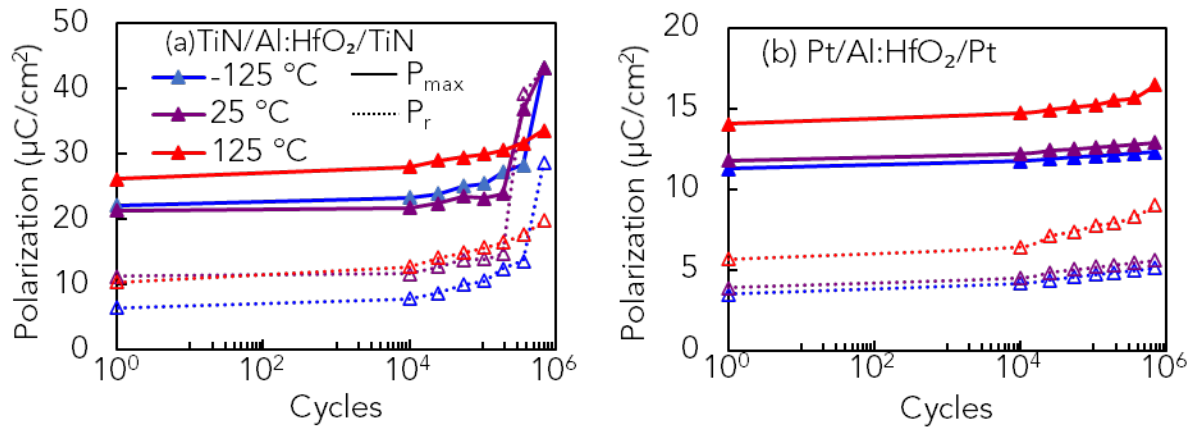


Figure 4.13. Remanent polarization ( $P_r$ ) and maximum polarization ( $P_{max}$ ) vs. number of cycles for (a) TiN/ 50 nm 4 at% Al:HfO<sub>2</sub>/TiN and (b) Pt/ 50 nm 4 at% Al:HfO<sub>2</sub>/Pt at -125 °C, 25 °C, and 125 °C.

change in  $P_r$  per electric field cycle,  $dP_r/dN$ , increases sharply in both samples after  $10^4$  cycles as shown in Figure 4.13., demonstrating that each of these samples experienced wake-up. The pre- and post- endurance cycling P-E loops and leakage current measurements are shown in Figure 4.14., and both samples transitioned from AFE-like to FE response with endurance cycling. The pre- and post-wake-up leakage current did not change significantly between pre- and post-endurance cycling as is shown in Figure 4.15. A measurement of the capacitance of

both the Pt/Al:HfO<sub>2</sub>/Pt and the TiN/Al:HfO<sub>2</sub>/TiN capacitors pre and post wake-up at room temperature also showed no change after wake-up.

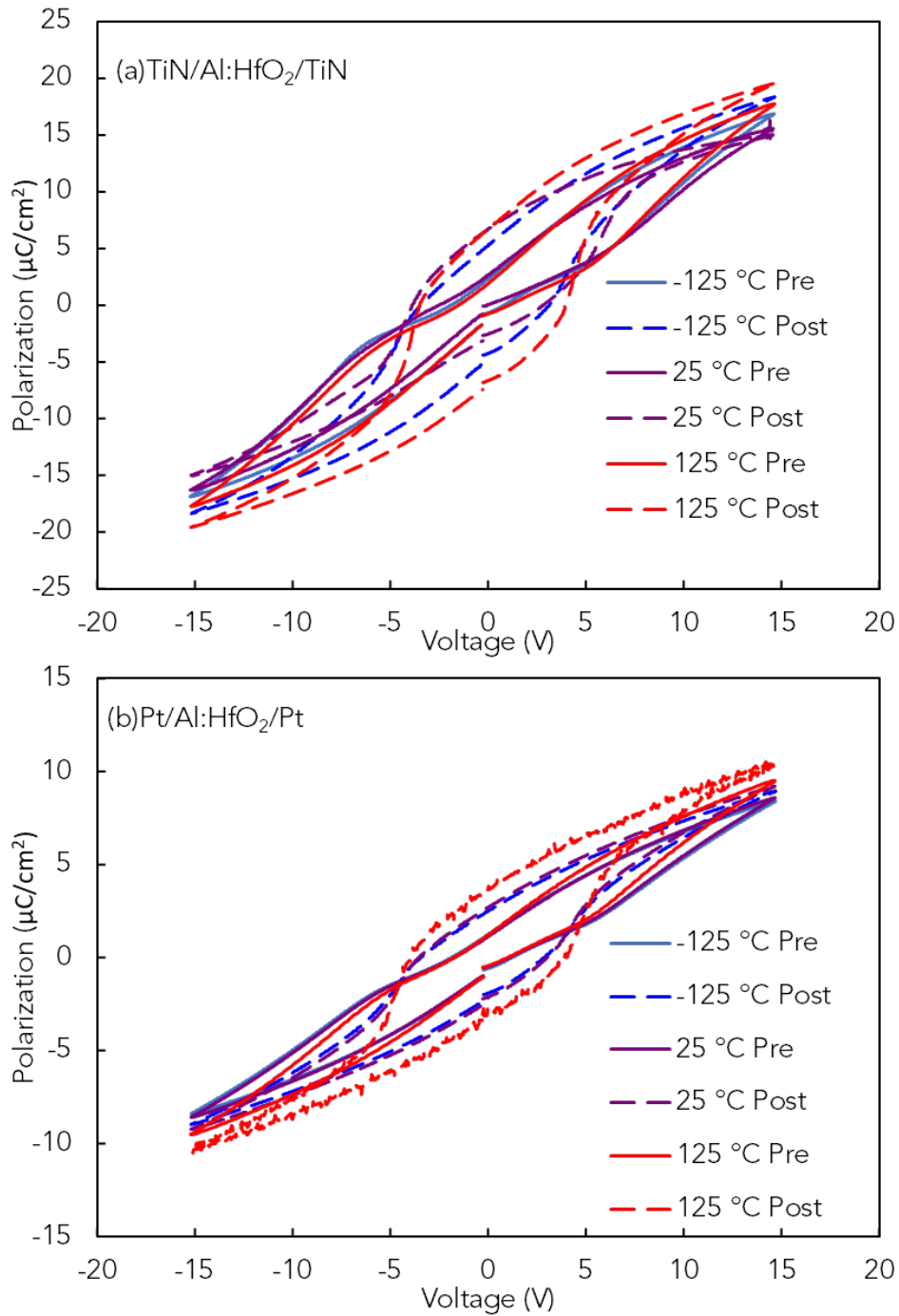


Figure 4.14. Pre and post endurance cycling PE loops at -125 °C, 25 °C, and 125 °C for (a) TiN/50 nm 4 at% Al:HfO<sub>2</sub>/TiN sample and (b) Pt/50 nm at% Al:HfO<sub>2</sub>/Pt.

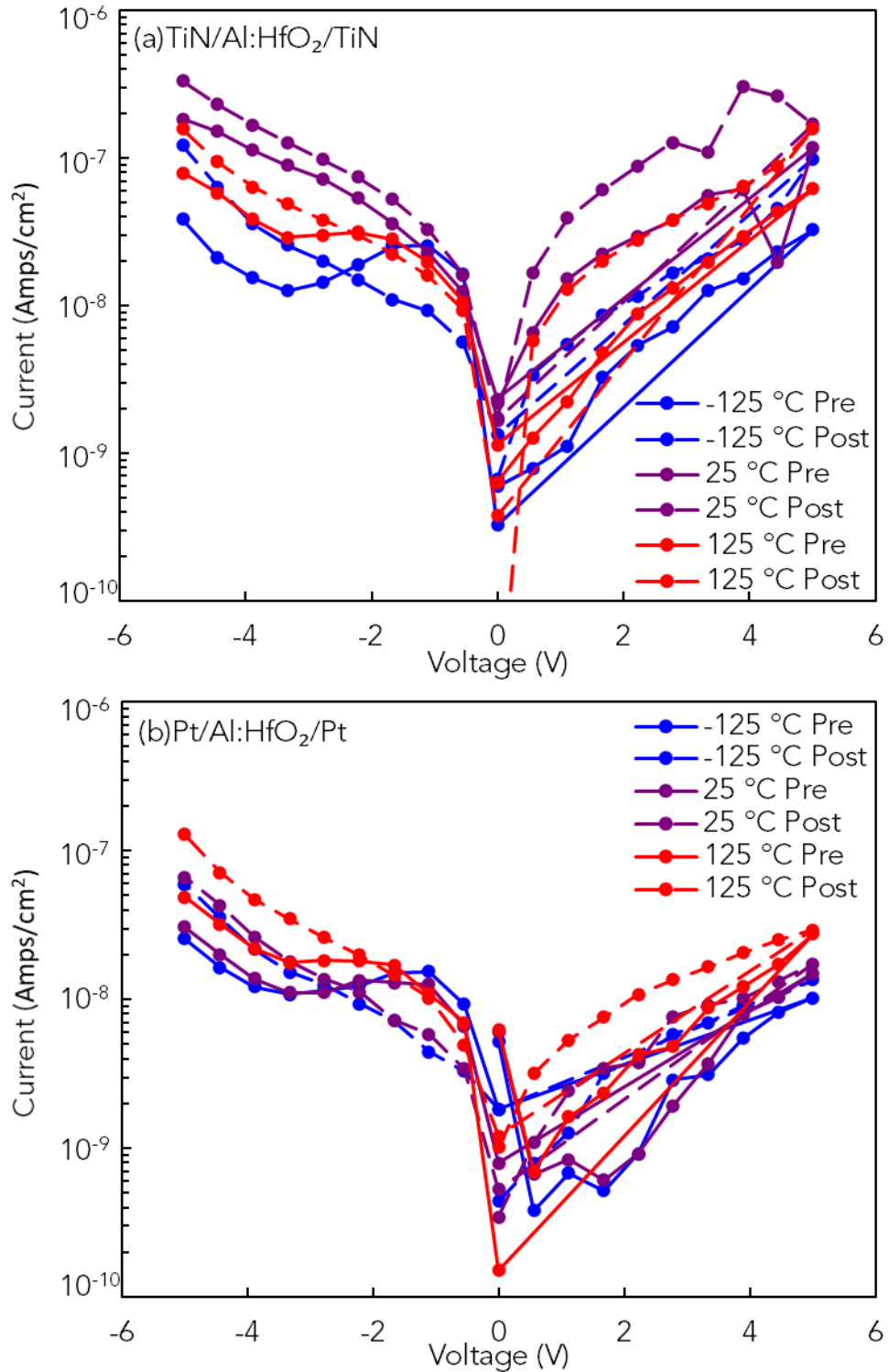


Figure 4.15. Pre and post endurance cycling leakage current measurements at -125 °C, 25 °C, and 125 °C for (a) TiN/50 nm 4 at% Al:HfO<sub>2</sub>/TiN sample and (b) Pt/50 nm at% Al:HfO<sub>2</sub>/Pt.

As previously stated, the stability in the P-E loops of these samples between -125 °C and 125 °C suggests that the driving mechanism for the AFE-like response in the TiN/Al:HfO<sub>2</sub>/TiN sample and the Pt/Al:HfO<sub>2</sub>/Pt sample is fairly temperature insensitive. This suggests that the driving mechanism for the AFE-like response in this material is unlikely to be caused by an electrically induced phase transition from tetragonal phase to orthorhombic phase since the tetragonal phase is the high temperature phase. The lack of a change in the permittivity of the material pre- and post-endurance cycling further suggests that the driving mechanism for wake-up in these samples is likely not a change in phase composition. The permittivity of the orthorhombic phase for HfO<sub>2</sub> has been previously reported as 30<sup>27</sup>, while the tetragonal phase has been reported as 35-40<sup>28</sup>. The lack of a shift in the permittivity suggests that an electric-field induced phase transition is likely not the main driving mechanism for the AFE-like response. Instead, the driving mechanism could be due to the ferroelectric/ferroelastic reorientation of orthorhombic domains' polar axis with endurance cycling<sup>29</sup>. The Pt/Al:HfO<sub>2</sub>/Pt capacitor and the TiN/Al:HfO<sub>2</sub>/TiN capacitor both experience different amplitudes of  $dP_r/dN$ . However, larger values of  $dP_r/dN$  can be seen after 10<sup>4</sup> cycles for both capacitors. Though the TiN/Al:HfO<sub>2</sub>/TiN capacitor experienced a larger  $dP_r/dN$  than that of the Pt/Al:HfO<sub>2</sub>/Pt capacitor after 10<sup>4</sup> cycles. The  $dP_r/dN$  of Pt/Al:HfO<sub>2</sub>/Pt is affected by temperature, with the quickest  $dP_r/dN$  occurring at 125 °C. Temperature dependent wake-up has also been previously noted in Y:HfO<sub>2</sub>, with both  $P_r$  prior to electric field cycling and  $P_r$  post electric field cycling increasing with temperature.<sup>30</sup> The increase in  $dP_r/dN$  was attributed to mobile charge defects, specifically oxygen vacancies<sup>30</sup>. Thus, the higher  $dP_r/dN$  in the TiN/Al:HfO<sub>2</sub>/TiN and Pt/Al:HfO<sub>2</sub>/Pt capacitors could be understood by increased movement of charged defects at higher temperatures. The hypothesis of

increased defects at higher temperatures is also supported by a small but distinctive increase in the leakage current from pre- to post-wake-up.

In conclusion, Al:HfO<sub>2</sub> thin films with either TiN electrodes or Pt electrodes are promising AFE-like architectures that exhibit enhanced temperature stability relative to other AFE materials. Their leakage current remains between 10<sup>-13</sup>-10<sup>-10</sup> A/cm<sup>2</sup> from -125 °C to 125 °C. The ESD and efficiencies are also temperature-stable between -125 °C and 125 °C. The TiN/Al:HfO<sub>2</sub>/TiN had the highest relative dielectric permittivity, ranging from 31.56 at -125 °C to 34.00 ± 0.48 at 125 °C and a TCC of 322 ± 41 ppm/°C, as well as the highest ESD value of 18.17 ± 0.79 J/cm<sup>3</sup>. The Pt/Al:HfO<sub>2</sub>/Pt had a more stable capacitance versus temperature with a TCC of only 78 ± 86 ppm/°C and a lower relative dielectric permittivity of 23.30 ± 0.25 at 25 °C. The endurance cycling of these capacitors at various temperatures revealed a wake-up effect in the  $P_r$ . The changes in leakage current and the increased  $dP_r/dN$  of wake-up for the TiN/Al:HfO<sub>2</sub>/TiN capacitors indicate the movement of charged defects was the mechanism driving the wake-up phenomenon. The low leakage current values and loss tangent values along with the low TCC values of the TiN/Al:HfO<sub>2</sub>/TiN and Pt/Al:HfO<sub>2</sub>/TiN devices highlight the potential of these thin films for commercial devices which require superior temperature stability.

## References

- 1 Alexis Payne, Owen Brewer, Asher Leff, Nicholas A. Strnad, Jacob L. Jones, and  
Brendan Hanrahan, *Applied Physics Letters* **117** (22), 221104 (2020).
- 2 Patrick D. Lomenzo, Ching-Chang Chung, Chuanzhen Zhou, Jacob L. Jones, and  
Toshikazu Nishida, *Applied Physics Letters* **110** (23), 232904 (2017).
- 3 Kati Kühnel, Malte Czernohorsky, Clemens Mart, and Wenke Weinreich, *Journal of  
Vacuum Science & Technology B* **37** (2), 021401 (2019).
- 4 J. D. Sullivan and P. H. Lauzon, *J Mater Sci Lett* **5** (12), 1245 (1986).
- 5 Patrick D. Lomenzo, Qanit Takmeel, Chuanzhen Zhou, Chris M. Fancher, Eric Lambers,  
Nicholas G. Rudawski, Jacob L. Jones, Saeed Moghaddam, and Toshikazu Nishida,  
*Journal of Applied Physics* **117** (13), 134105 (2015).
- 6 Dayu Zhou, Jin Xu, Qing Li, Yan Guan, Fei Cao, Xianlin Dong, Johannes Müller, Tony  
Schenk, and Uwe Schröder, *Applied Physics Letters* **103** (19), 192904 (2013).
- 7 Everett D. Grimley, Tony Schenk, Xiahan Sang, Milan Pešić, Uwe Schroeder, Thomas  
Mikolajick, and James M. LeBeau, *Advanced Electronic Materials* **2** (9), 1600173  
(2016).
- 8 U. Schröder, E. Yurchuk, J. Müller, D. Martin, T. Schenk, P. Polakowski, C. Adelman,  
M. I. Popovici, S. V. Kalinin, and T. Mikolajick, **53** (08LE02) (2014).
- 9 Tae Yoon Lee, Kyoungjun Lee, Hong Heon Lim, Myeong Seop Song, Sang Mo Yang,  
Hyang Keun Yoo, Dong Ik Suh, Zhongwei Zhu, Alexander Yoon, Matthew R.  
MacDonald, Xinjian Lei, Hu Young Jeong, Donghoon Lee, Kunwoo Park, Jungwon  
Park, and Seung Chul Chae, *ACS Appl. Mater. Interfaces* **11** (3), 3142 (2019).
- 10 W. L. Zhang, Y. H. Mao, L. Cui, M. H. Tang, P. Y. Su, X. J. Long, Y. G. Xiao, and S. A.  
Yan, *Phys. Chem. Chem. Phys.* **22** (38), 21893 (2020).
- 11 Wei Zhang, Ji-Zhou Kong, Zheng-Yi Cao, Ai-Dong Li, Lai-Guo Wang, Lin Zhu, Xin Li,  
Yan-Qiang Cao, and Di Wu, *Nanoscale Res Lett* **12** (1), 393 (2017).
- 12 Xianwu Tang, Linghua Jin, Jianming Dai, Xuebin Zhu, and Yuping Sun, *Journal of  
Alloys and Compounds* **695**, 2458 (2017).
- 13 Kyung-Hoon Cho, Chang-Hak Choi, Joo-Young Choi, Tae-Geun Seong, Sahn Nahm,  
Chong-Yun Kang, Seok-Jin Yoon, and Jong-Hee Kim, *Journal of the European Ceramic  
Society* **30** (2), 513 (2010).
- 14 Min Hyuk Park, Han Joon Kim, Yu Jin Kim, Taehwan Moon, Keum Do Kim, and Cheol  
Seong Hwang, *Advanced Energy Materials* **4** (16), 1400610 (2014).
- 15 Jiwei Zhai and Haydn Chen, *Applied Physics Letters* **82** (16), 2673 (2003).
- 16 Brendan Hanrahan, Cosme Milesi-Brault, Asher Leff, Alexis Payne, Shi Liu, Mael  
Guennou, and Nicholas Strnad, *APL Materials* **9** (2), 021108 (2021).
- 17 B. Zeng, W. Xiao, J. Liao, H. Liu, M. Liao, Q. Peng, S. Zheng, and Y. Zhou, *IEEE  
Electron Device Letters* **39** (10), 1508 (2018).
- 18 M. Hoffmann, U. Schroeder, T. Schenk, T. Shimizu, H. Funakubo, O. Sakata, D. Pohl,  
M. Drescher, C. Adelman, R. Materlik, A. Kersch, and T. Mikolajick, *Journal of  
Applied Physics* **118** (7), 072006 (2015).
- 19 Yuh-Chen Lin, Felicia Mcguire, and Aaron D. Franklina, 2017 (unpublished).
- 20 Min Hyuk Park, Ching-Chang Chung, Tony Schenk, Claudia Richter, Michael  
Hoffmann, Steffen Wirth, Jacob L. Jones, Thomas Mikolajick, and Uwe Schroeder,  
*Advanced Electronic Materials* **4** (4), 1700489 (2018).

21 Faizan Ali, Xiaohua Liu, Dayu Zhou, Xirui Yang, Jin Xu, Tony Schenk, Johannes  
Müller, Uwe Schroeder, Fei Cao, and Xianlin Dong, *Journal of Applied Physics* **122**  
(14), 144105 (2017).

22 Min Hyuk Park, Han Joon Kim, Yu Jin Kim, Taehwan Moon, and Cheol Seong Hwang,  
*Applied Physics Letters* **104** (7), 072901 (2014).

23 Younghwan Lee, H. Alex Hsain, Shelby S. Fields, Samantha T. Jaszewski, Madison D.  
Horgan, Patrick G. Edgington, Jon F. Ihlefeld, Gregory N. Parsons, and Jacob L. Jones,  
*Applied Physics Letters* **118** (1), 012903 (2021).

24 M. J. Chen, X. K. Ning, S. F. Wang, and G. S. Fu, *Nanoscale* **11** (4), 1914 (2019).

25 Buwei Sun, Mengyao Guo, Ming Wu, Zhuang Ma, Weiwei Gao, Haonan Sun, and  
Xiaojie Lou, *Ceramics International* **45** (16), 20046 (2019).

26 AVX Corporation, edited by Radovan Faltus (AVX Corporation), Vol. 2021.

27 Johannes Müller, Tim S. Börscke, Uwe Schröder, Stefan Mueller, Dennis Bräuhaus,  
Ulrich Böttger, Lothar Frey, and Thomas Mikolajick, *Nano Letters* **12** (8), 4318 (2012).

28 Min Hyuk Park, Han Joon Kim, Yu Jin Kim, Woongkyu Lee, Taehwan Moon, and Cheol  
Seong Hwang, *Applied Physics Letters* **102** (24), 242905 (2013).

29 Clemens Mart, Thomas Kämpfe, Raik Hoffmann, Sophia Eblinger, Sven Kirbach, Kati  
Kühnel, Malte Czernohorsky, Lukas M. Eng, and Wenke Weinreich, *Advanced*  
*Electronic Materials* **6** (3), 1901015 (2020).

30 S. Starschich, S. Menzel, and U. Böttger, *Applied Physics Letters* **108** (3), 032903  
(2016).

## Chapter 5: 3D Ferroelectric HfO<sub>2</sub> Thin Film Characterization

This chapter demonstrates the unique suite of materials and device characterizations made available from the 3D ferroelectric platform. These include electrical characteristics of AECs, the crystal structure of the sidewall of thin films, and the piezoelectric response of the thin film. The layer structure of all the devices described within this chapter were SiO<sub>2</sub>/TiN/4 at% Al:HfO<sub>2</sub>/TiN. The growth and deposition process of these thin film layers onto the 3D structured substrate are detailed in section 3.2.4.

### 5.1. Area-Enhanced Capacitor Electrical Measurements

One of the primary motivations for conformally-coating ferroelectric materials is the ability to increase the total capacitor area without increasing the device footprint through the use area enhancement via topography. In this work pillars, holes, trenches, and walls were all

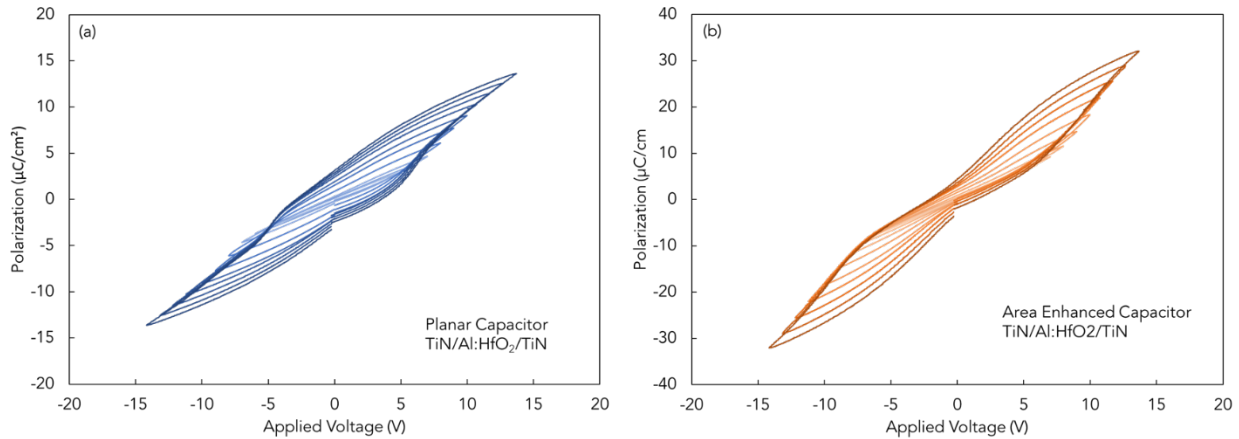


Figure 5.1. (a) P-E loops with increasing voltage of a planar capacitor (b) P-E loops with increasing voltage of AEC, specifically a trench capacitor that has twenty trenches that are 2 μm wide and 10 μm deep. The AEC has a surface area enhancement of 1.87 over the planar capacitor. Note the y axis scale difference (factor of 2) between (a) and (b).

fabricated to accomplish the area enhancements. The P-E field loops of planar and area enhanced trench capacitors with equal footprint areas of 0.00181 cm<sup>2</sup> were measured. The trench capacitor in Figure 5.1. contained twenty trenches that were 2 μm wide and 10 μm deep resulting in an

estimated 1.87 times estimated surface area enhancement over the planar capacitor.

Unexpectedly, the  $P_{max}$  for the planar sample was  $13.63 \mu\text{C}/\text{cm}^2$ , while for the AEC it was  $32.07 \mu\text{C}/\text{cm}^2$ , 2.35 times larger than the planar. It is clear from Figure 5.1. that more than just area enhancement is observed; the AEC exhibited a more AFE-like response, i.e. a lower  $P_r$  and “double-loop polarization”, than the planar capacitor. To understand the implications of this polarization response on the energy storage potential for the AEC devices, a series of monopolar P-E loop measurements with increasing voltage were taken and subsequent ESD and  $\eta$  values were calculated from Eq. (1 – 4). These are shown in Figure 5.2. It is important to note the ESD

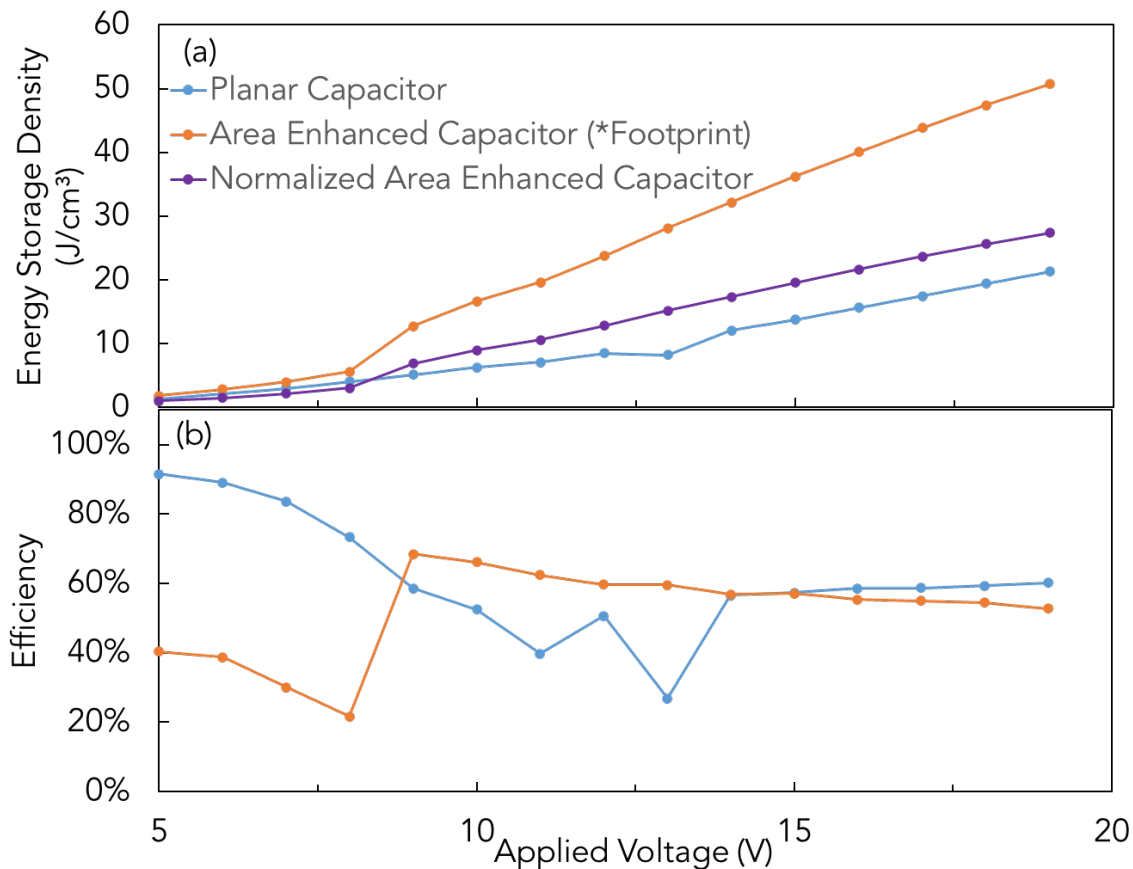


Figure 5.2. (a) ESD as a function of applied voltage for the AEC, containing twenty trenches that are  $2 \mu\text{m}$  wide and  $10 \mu\text{m}$  deep, using the foot print area of the AEC for the calculation, using the estimated surface area (up and over trenches) denoted as the normalized AEC, and the ESD of the planar capacitor, (b) efficiency of the AEC and the planar capacitor vs. applied voltage.

was calculated from Eq.1– 4 using the footprint area ( $0.00181 \text{ cm}^2$ ) for the AEC. A normalized ESD value for the AEC was also calculated, this was done by dividing by the 1.87 estimated surface area enhancement. This normalization shows the energy storage benefits of the polarization loop itself, discounting the area enhancement. Another explanation is that the surface area enhancement is underestimated, due to further area enhancement from the scalloping of the trench sidewalls from the DRIE process (Figure 3.9.). The  $V_{BD}$  of the planar capacitor was measured to be 28 V and thus has an estimated  $V_{op}$  of 7 V. Comparing the two capacitors at the theoretical  $V_{op}$ , it is surprising to note that the planar capacitor would be the better choice. The enhanced ESD at  $V_{op}$  is due to the capacitors having similar ESD values at 7V, but the planar capacitor maintaining a much higher value for  $\eta$ , 83.65% as compared 30.12%. The monopolar loops from which the ESD and  $\eta$  values were calculated and are shown in Figure 5.3. At lower applied fields, the planar capacitor has a slimmer hysteresis response as compared

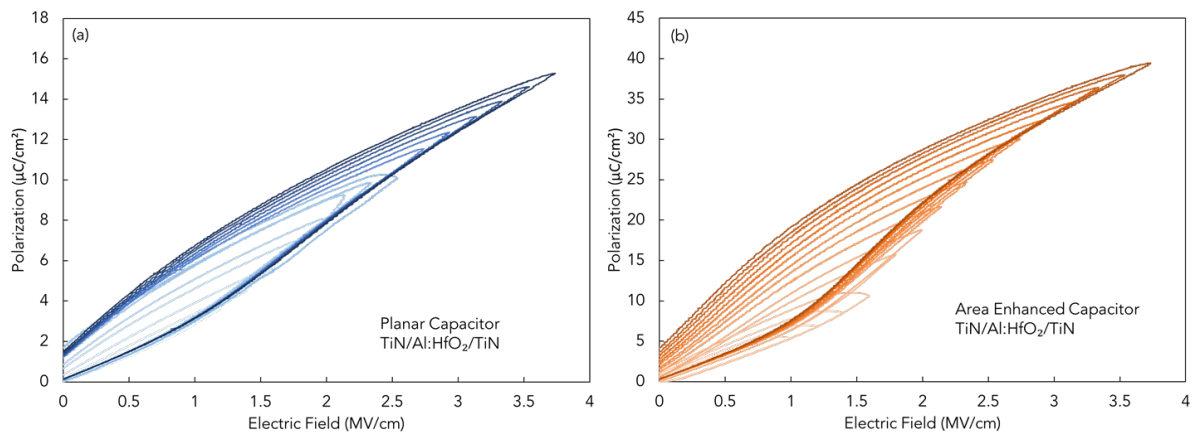


Figure 5.3. (a) monopolar P-E loops as a function of applied electric field for the planar capacitor used to calculate ESD and efficiency (b) monopolar P-E loops as a function of applied electric field for the AEC, containing twenty trenches that are  $2 \mu\text{m}$  wide and  $10 \mu\text{m}$  deep, the area used in calculating the polarization was the footprint of the AEC.

with the AEC low field monopolar loops, which gives rise to its higher calculated  $\eta$  values at low field. Leakage current density measurements were also taken for both the planar capacitor and

the AEC, these are shown in Figure 5.4. The leakage current densities of both were similar, within an order of magnitude of each other at all voltages measured.

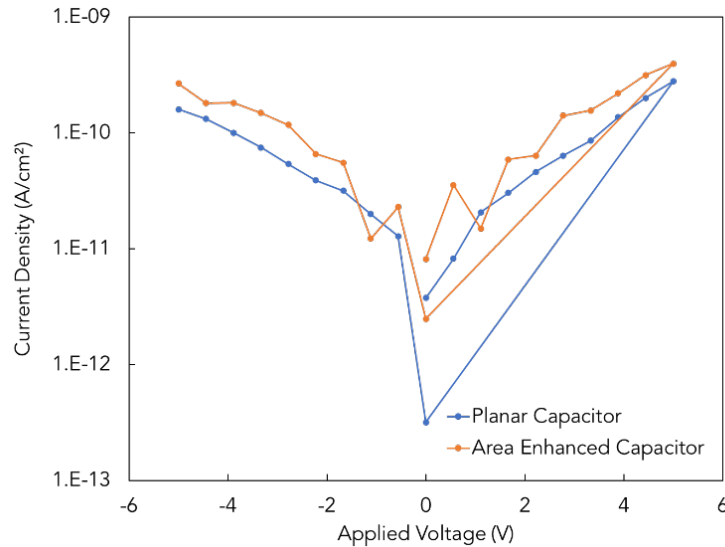


Figure 5.4. Leakage current density measurements for both the planar capacitor and the AEC capacitor containing twenty trenches that are 2  $\mu\text{m}$  wide and 10  $\mu\text{m}$  deep.

## 5.2. Sidewall Thin Film Crystal Structure

A high-density trench structure is patterned on the 3D characterization wafer to provide a large area for X-ray diffraction studies to elucidate any differences in observed properties between sidewall-active and planar structures, like the differences observed above. To understand the possible origin of the differences observed in the P-E loops of the planar capacitor versus that of the AEC, XRD patterns were obtained before and after ion-milling away the planar region of the trench capacitors so there are two scans: whole trench and sidewall-only. Bragg Brentano XRD patterns and a series of rocking curve measurements were taken using a Panalytical X'Pert3 MRD X-ray Diffraction System, using a PIXel<sup>3D</sup> detector and a parabolic

mirror on the source. A schematic denoting the different rotation axes with respect to the orientation of the trench structures is shown in Figure 5.5. The incident beam angle is

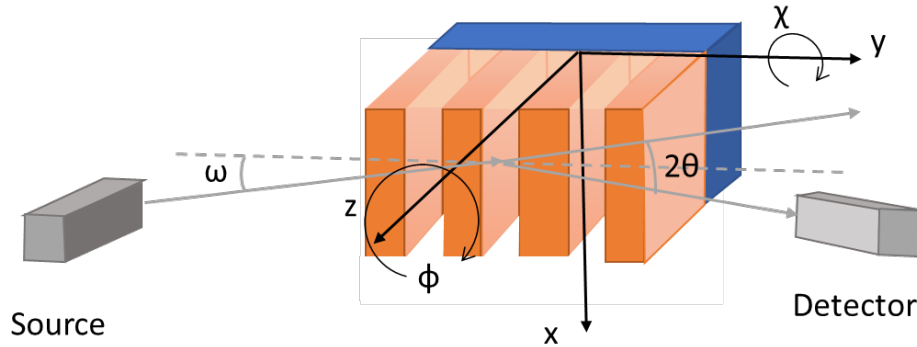


Figure 5.5. A schematic of the trench structures mounted with respect to the source and detector of the XRD source.  $\omega$  and  $2\theta$  represent the angle of the incident beam and reflected beam respectively,  $\chi$  represents the sample tilt angle, and  $\phi$  represents the sample spin angle.

denoted by  $\omega$  and the reflected beam angle is denoted by  $2\theta$ . The tilt angle of the sample is represented by  $\chi$  and the sample spin angle is denoted by  $\phi$ . The Bragg Brentano XRD patterns are shown in Figures 5.6., with a XRD pattern in the region of interest around the highest intensity  $\text{HfO}_2$  peak, a combination of the orthorhombic 111(o111) and the tetragonal 101 (t101) in Figure 5.7. The XRD Pattern shown in Figure 5.6. shows the full capacitor vs. that of the planar capacitor to be virtually identical. However, focusing in (Figure 5.7.) reveals a slight difference between the two patterns, in that the full AEC has a broader o111/t101  $\text{HfO}_2$  peak versus the o111/t101  $\text{HfO}_2$  peak from just the sidewalls. The difference in peak shape reveals there is a phase composition difference between the thin film deposited on just the sidewalls as

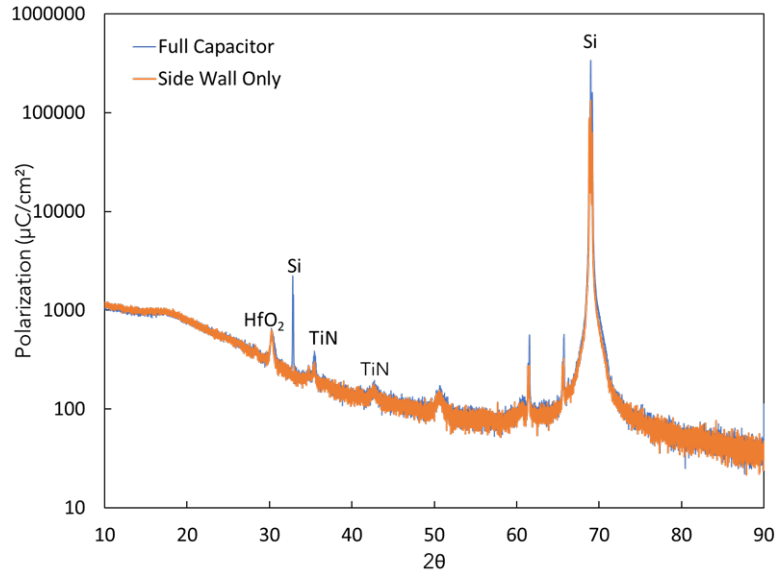


Figure 5.6. XRD Pattern of the full capacitor prior to being ion milled, and then the capacitor after being ion milled with only sidewall thin film remaining.

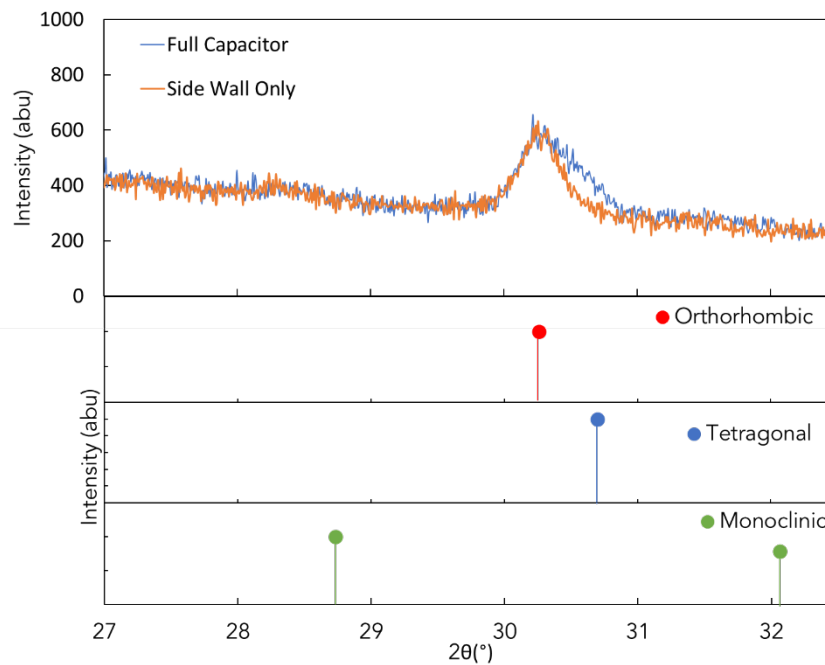


Figure 5.7. Bragg Brentano XRD Patterns from  $27^\circ$  to  $32.5^\circ$ , along with the peak positions for the o-phase (PDF 04-005-5597), t-phase (PDF 04-011-8820), and the m-phase (00-034-0104). The peak positions of the PDFs have been shifted from original positions to compensate for strain.

compared with the full capacitor. The full capacitor appears to have more tetragonal phase present than that of just the sidewalls. This is unexpected considering the bi-polar P-E loops

shown in Figure 5.1. revealed the planar sample to be less AFE-like than that of the AEC, and the AFE-like response in HfO<sub>2</sub>-based thin films associated with the tetragonal phase<sup>1,2</sup>. The mono-polar loops used for energy storage calculations, however, are as-expected with the AEC with higher tetragonal phase showing a lower P<sub>r</sub>. Combined, the difference in phase composition and the P-E loops suggest that there is a defect origin to the bi-polar response which requires reverse-bias to observe, not something crystallographic. These defects could come from differences in thermal history from top-down RTA annealing. The rocking curve measurements were taken around the 0111/t101 HfO<sub>2</sub> peak ~30°. There was an ω-rocking curve measurement, a χ-rocking curve measurement, and a φ rocking curve measurement, which are shown in Figure 5.8. None of the rocking curves contained a clear peak, demonstrating that the thin films were predominantly randomly oriented.

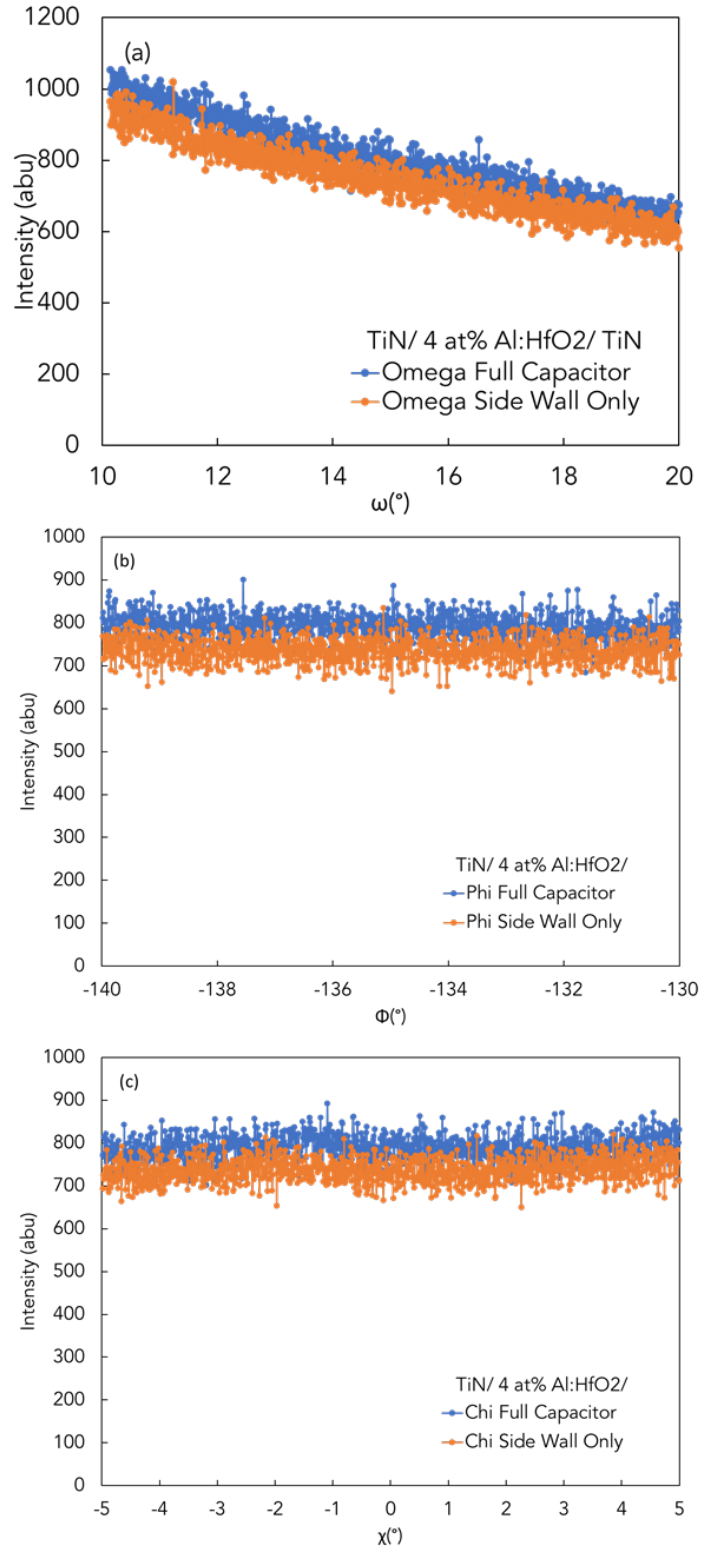


Figure 5.8. (a)  $\omega$ -rocking curve, (b)  $\Phi$ -rocking curve, (c)  $\chi$ -rocking curve around  $0111/t101$   $\text{HfO}_2$  peak.

### 5.3. Piezoelectric Response

Piezoelectric response is a critical material property that is currently almost absent from literature for the fluorite ferroelectrics<sup>3-6</sup>. The 3D characterization wafer included a number of released structures to be used for piezoelectric analysis. The voltage-driven displacement of a 175  $\mu\text{m}$  M-cantilever, was measured using a Polytec OFV-5000 Modular Vibrometer. A bipolar 14 V sine waveform was applied to the M-cantilever at 200 Hz, the measurement averaged 10 measurements each 6.4 ms in length. Due to the strain state of the layers making up the M-cantilever, 500 nm  $\text{SiO}_2$ /50 nm TiN/ 50 nm 4 at% Al:HfO<sub>2</sub>/ 50 nm TiN, the cantilever curled upon release (shown in a schematic representation in Figure 5.9a.). In Figure 5.9b., a top down optical microscope image of the M-cantilever measured is shown. The laser from the LDV

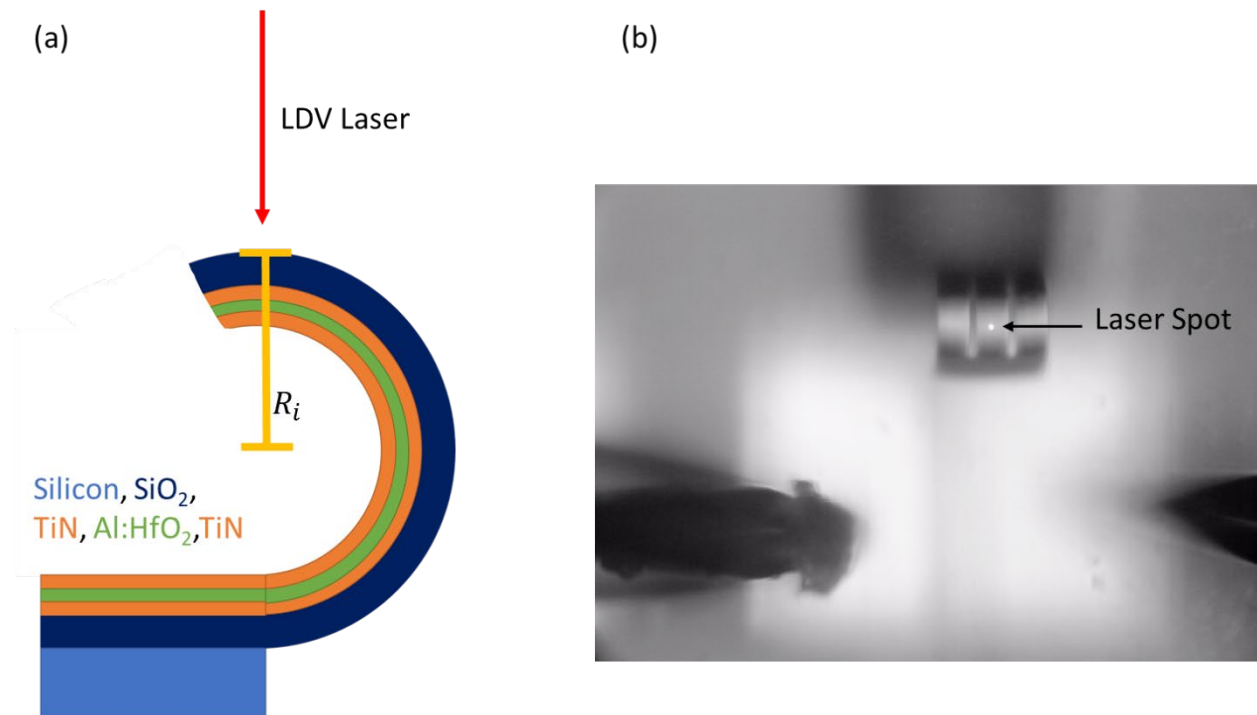


Figure 5. 9. (a) Schematic representing the M-cantilever upon release with the position of the laser from the LDV denoted as well as the initial radius,  $R_i$ , (b) an optical microscope image of the M-cantilever as measured by the LDV, with the laser spot showing up as a white dot on the backside of the curled M-cantilever.

reflects off the top-most part of the cantilever as shown in Figure 5.9. The initial height, and subsequent radius of curvature, measured using an OLYMPUS LEXT OLS4000 Industrial Laser Measuring Microscope as  $106.3 \mu\text{m}$ , thus  $R_i$  was  $53.15 \mu\text{m}$ . As a positive voltage was applied to the beam the radius of curvature increased, the displacement versus electric field plot is shown in Figure 5.10. The maximum displacement measured of the top of the M-cantilever from its initial position was  $963 \text{ nm}$ .

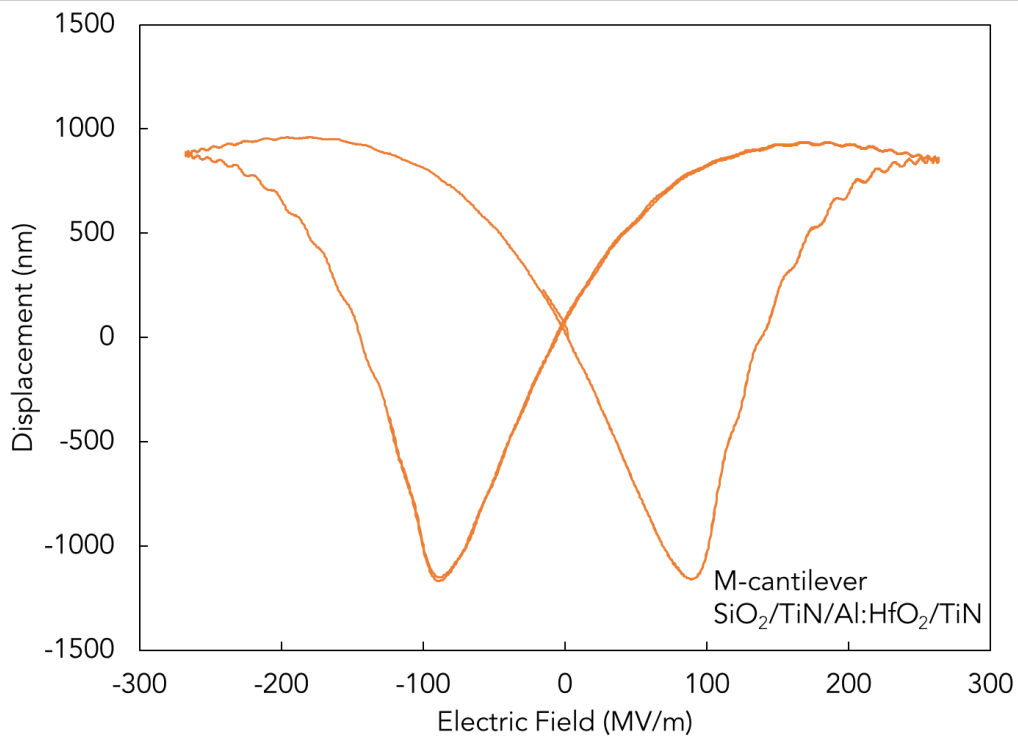


Figure 5.10. Plot of displacement of top of M-cantilever versus applied electric field.

The field induced in-plane displacements in the 4 at% Al:HfO<sub>2</sub> thin film were calculated, if these displacements were piezoelectric in nature the transverse piezoelectric coefficient could be calculated,  $e_{31,f}$ . However, since we suspect other contributions in addition to the piezoelectric, it is referred to here as  $e_{31,f}^*$ . In this calculation the stress distribution within in layer is assumed to be constant. Every layer of the cantilever had affects the measured response,

and thus the volume of each layer,  $v_{layer}$ , along with weighted total beam volume,  $v_{beam}$ , was first calculated, Eqs. (5 – 1) and (5 – 2):

$$v_{layer} = t_{layer}w_{layer}l_{layer} \quad (5 - 1)$$

$$v_{beam} = \sum v_{layer} \quad (5 - 2)$$

$t_{layer}$ ,  $w_{layer}$ , and  $l_{layer}$  are the thickness, width, and length of each layer respectively. The Young's modulus of the beam,  $Y_{beam}$ , is the summation of the Young's modulus of each respective layer,  $Y_{layer}$ , multiplied by the volume fraction of that layer of the composite stack, shown in Eq. (5 – 3)<sup>7</sup>:

$$Y_{beam} = \sum \left( Y_{layer} * \left( \frac{v_{layer}}{v_{beam}} \right) \right) \quad (5 - 3)$$

The neutral axis of the beam,  $y_{beam}$ , is calculated by dividing the product of the cross-sectional area of each layer and the vertical center of that layer with respect to the bottom of the beam,  $y_{layer}$ , by sum of the cross sectional areas of each layer, which is then weighted by multiplying by the  $Y_{layer}$  divided by the  $Y_{SiO_2}$ , as shown in Eq. (5 – 4)<sup>7</sup>:

$$y_{beam} = \frac{\sum t_{layer}w_{layer}y_{layer} \left( \frac{Y_{layer}}{Y_{SiO_2}} \right)}{\sum t_{layer}w_{layer}} \quad (5 - 4)$$

The area moment of inertia for each layer is also calculated and weighted by multiplying the  $Y_{layer}$  divided by the  $Y_{SiO_2}$ , shown in Eq. (5 – 5)<sup>8</sup>:

$$I_{layer} = \frac{w_{layer}t_{layer}^3}{12} \frac{Y_{layer}}{Y_{SiO_2}} \quad (5 - 5)$$

The area moment of inertia of the beam is similar to the Young's modulus of the beam in that it is the sum of the moment of inertia of the individual layers and the product of the cross-sectional

area of each layer and the distance from the center of the layer to the neutral axis of the beam stack,  $y_{offset}$ , squared as shown in Eq. (5 – 6)<sup>7</sup>:

$$I_{beam} = \sum \left( I_{layer} + \frac{t_{layer} w_{layer} Y_{layer}}{Y_{SiO_2}} y_{offset}^2 \right) \quad (5 - 6)$$

$Y_{beam}$  and  $I_{beam}$  both are used to compute the stack constant,  $\beta$ , for the cantilever, shown in Eq. (5 – 7)<sup>9</sup>:

$$\beta = \frac{Y_{beam} I_{beam}}{t_p w_p y_p} \quad (5 - 7)$$

Where  $t_p$  is the thickness of the piezoelectric thin film,  $Y_p$  is the Young's modulus of the piezoelectric thin film,  $w_p$  is the width of the piezoelectric thin film, and  $y_p$  is the distance of the center of the piezoelectric thin film from the neutral axis of the beam. Eq. (5 – 8) is a calculation of the cantilever tip angle,  $\theta$ :

$$\theta = \frac{l_{beam}}{R} \quad (5 - 8)$$

Where  $l_{beam}$  is the length of the cantilever and  $R$  is the radius of curvature. The relationship between the displacement of the cantilever and the change in  $\theta$  is given by Eq. (5 – 9):

$$\theta = \frac{M_{beam} l_{beam}}{Y_{beam} I_{beam}} \quad (5 - 9)$$

Where  $M_{beam}$  is the bending moment of the beam. Combining Eqs. (5 – 8) and (5 – 9), a relationship between the change in radius of curvature and the change in moment applied to the beam is formed, which is shown in Eq. (5 – 10):<sup>7,9</sup>

$$\left( \frac{1}{R_f - R_i} \right) = \frac{\Delta M_{beam}}{Y_{beam} I_{beam}} \quad (5 - 10)$$

Where  $R_i$  and  $R_f$  are the initial and final radius of curvature, respectively. Another way of calculating the bending moment is shown in Eq. (5 – 11):

$$M_{beam} = F_p y_p = t_p w_p \sigma y_p \quad (5 - 11)$$

Where  $F_p$  is the force applied by the piezoelectric thin film and  $\sigma$  is the stress. Plugging, Eq. (5 – 11) into Eq. (5 – 10):

$$\left( \frac{1}{R_f - R_i} \right) = \frac{t_p w_p y_p \Delta(e_{31} E)}{Y_{beam} I_{beam}} \quad (5 - 12)$$

Which when combined with Eq. (5 – 11):

$$\left( \frac{1}{R_f - R_i} \right) \beta = \Delta e_{31,f}^* \left( \frac{V}{t_p} \right) \quad (5 - 13)$$

Where  $V$  is the applied voltage. However,  $e_{31,f}^*$  is actually non-linear and a function of the applied field,  $E$ , and thus the relationship between  $e_{31,f}^*$  and the change in curvature can be calculated using Eq. (5 – 14):

$$\beta \frac{\partial}{\partial E} \left( \frac{1}{R} \right) = e_{31,f}^*(E) \quad (5 - 14)$$

The values used for the film thickness of each layer, the width of each layer, the length of each layer, and Young's moduli of each layer are shown in Table 5.1.

Table 5.1. Thickness, width, length, and Young's modulus of each layer of the cantilever.

<b>Layer</b>	<b>Thickness (nm)</b>	<b>Width (<math>\mu\text{m}</math>)</b>	<b>Length (<math>\mu\text{m}</math>)</b>	<b>Young's Modulus (GPa)</b>
<b>SiO<sub>2</sub></b>	500	23	175	72.3 <sup>10</sup>
<b>TiN (bottom electrode)</b>	50	23	175	250 <sup>11</sup>
<b>Al:HfO<sub>2</sub></b>	50	23	175	204 <sup>12</sup>
<b>TiN (top electrode)</b>	50	16	175	250 <sup>11</sup>

A derivate was used to calculate  $\partial E$  and  $\frac{\partial}{\partial E} \left( \frac{1}{R} \right)$  from the displacement data, which in turn was used to calculate  $e_{31,f}^*$  versus electric field shown in Figure 5.11. This is different than standard low oscillation field measurements typical for calculating weak-field  $e_{31}$ .

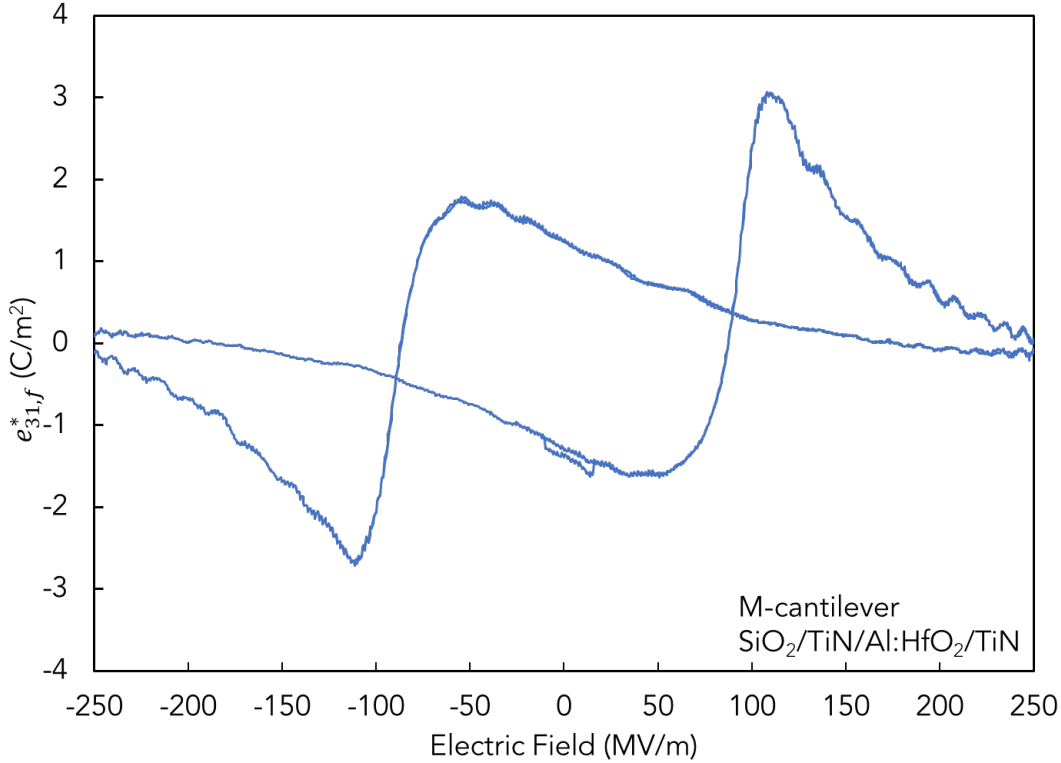


Figure 5.11. Plot of versus electric field for the SiO<sub>2</sub>/TiN/Al:HfO<sub>2</sub>/TiN M-cantilever.

The maximum values of  $e_{31,f}^*$  measured are due to ferroelectric domain switching, however, the 0 field value of  $e_{31,f}^*$  was 1.38 C/m<sup>2</sup>, which is extremely close in magnitude to theoretical  $e_{31}$  of -1.49 C/m<sup>2</sup> predicted by Materlik<sup>13</sup>. This value has also been calculated by Dutta *et al.* using Vienna Ab-initio Simulation Package as -1.31 C/m<sup>2</sup> and ABINIT as -1.53 C/m<sup>2</sup>.<sup>14</sup> Surprisingly though, the  $e_{31,f}^*$  has the opposite sign of what is predicted theoretically. Ferroelectric materials are known to have negative  $e_{31,f}$  values, while antiferroelectric materials are known to have positive  $e_{31,f}$ <sup>15</sup>. In PZO, a classic antiferroelectric material, as the c-axis of

the unit cell elongates, the polarization of the material increases along the a-axis, thus it has a positive  $e_{31,f}$ <sup>14</sup>. While ferroelectric PZT is known to have a negative  $e_{31,f}$  as the c-axis of the unit cell elongates the polarization along the a-axis decreases<sup>14</sup>. Thus, a positive  $e_{31,f}^*$  could be indicative of an AFE response and not just an AFE-like response. In other words, the material could have some classic AFE phase present in the material, where the polarization of the unit cells were aligned in antiparallel<sup>16</sup>. The positive  $e_{31,f}^*$  could also be explained by a field induced phase transition from AFE to FE, i.e. t-phase to o-phase. The unit cell volume for the t-phase, 131.1 Å<sup>3</sup>, is smaller than the unit cell volume of 133.5 Å<sup>3</sup> for the o-phase<sup>16</sup>. This volumetric expansion in all directions would explain the positive  $e_{31,f}^*$  measured. Another possible reason for the positive transverse piezoelectric coefficient, could be due to the fact that the material has been measured to have a negative longitudinal piezoelectric coefficient,  $d_{33,f}$ <sup>17</sup>. This is opposite of a ‘normal’ ferroelectric like PZT, which has a positive  $d_{33,f}$  with a negative  $d_{31,f}$ . Opposite signs of  $e_{33,f}$  and  $e_{31,f}$  would mean one dimension of the unit cell expands while the other contracts. However, Böske *et al.*,<sup>3</sup> Kirbach *et al.*<sup>18</sup>, Starschich *et al.*<sup>19</sup>, have all measured positive  $d_{33,f}$  values in their HfO<sub>2</sub>-based ferroelectric thin films. Kirbach *et al.* contributed the positive  $d_{33,f}$  value to be due to the ferroelectric/ferroelastic reorientation of the orthorhombic unit cell<sup>18</sup>. The signs of  $e_{33,f}$  and  $e_{31,f}$  being the same would indicate the material is an electrical analog to auxetic materials, i.e. a material that contracts or expands in all directions in response to an applied electric field, which Liu *et al.* have used *ab-initio* calculations to suggest ferroelectric HfO<sub>2</sub>-based thin films could be<sup>20</sup>. Further, Dutta *et al.* have calculated from first principles that the sign of  $e_{33,f}$  could change as a function of epitaxial strain for ferroelectric HfO<sub>2</sub>-based thin films, which could help explain both positive and negative values of  $d_{33,f}$  being reported for the thin films.

To the best of the author's knowledge, there have been no other reported values for  $e_{31,f}$  calculated from actuating a ferroelectric HfO<sub>2</sub>-based thin film. For PZT thin films,  $e_{31}$  values have been continuously increasing over the last 20 years, reaching values between -15 and -20 C/m<sup>2</sup> as a result of processing and material refinement<sup>21</sup>. Ba<sub>x</sub>Sr<sub>1-x</sub>TiO<sub>3</sub> thin films were deposited via chemical solution deposition at 200 nm thick and demonstrated maximum  $e_{31}$  of -3.0 C/m<sup>2</sup><sup>22</sup>. All of these values demonstrate that the positive  $e_{31,f}^*$  of released Al:HfO<sub>2</sub> is smaller than values typical of other piezoelectric thin films, but it is a positive value measured on a much thinner thin film than the Pb-based and BaTiO<sub>3</sub>-based thin films. These two factors combined with the indirect piezoelectric coefficient measured will enable Al:HfO<sub>2</sub> thin films to be considered for new and exciting piezoMEMS applications.

An initial LDV measurement was taken of another 175  $\mu\text{m}$  M-cantilever using a 14 V bipolar sine waveform at 200 Hz, each individual measurement collected data for 1.6 ms, and ten individual measurements were averaged in the data shown in Figure 5.12. The cantilever was

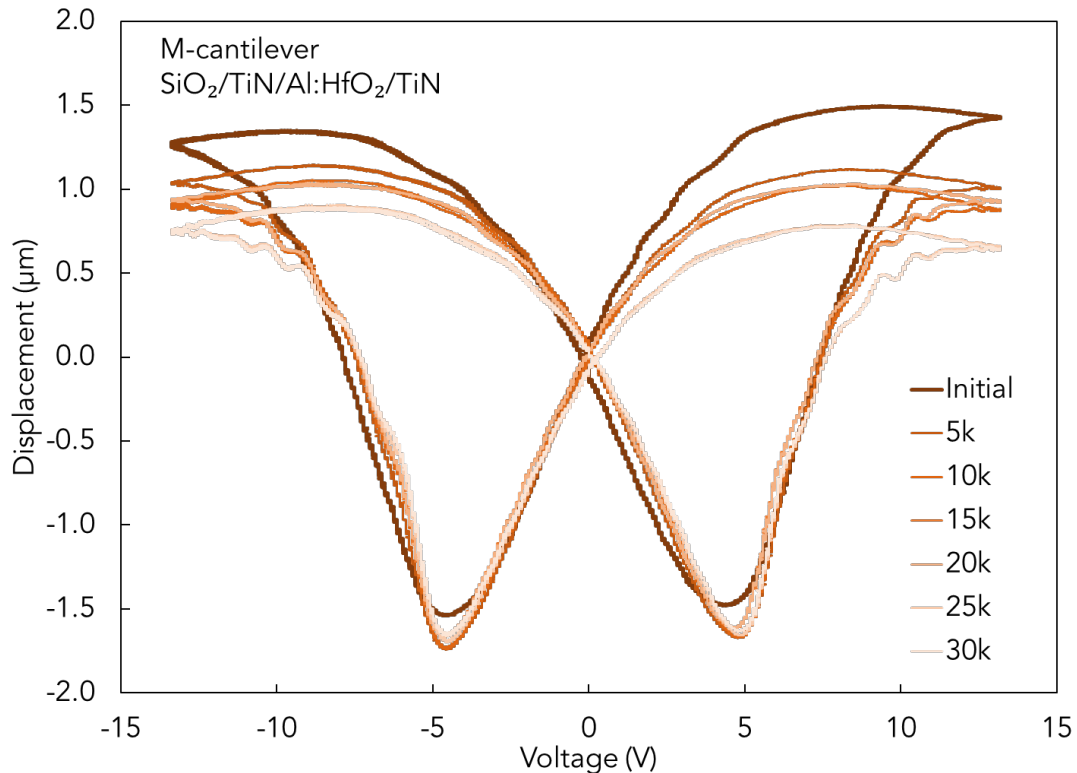


Figure 5.12. A displacement versus applied voltage plot after increasing number of electric field cycles was applied to a 175  $\mu\text{m}$  M-cantilever, consisting of  $\text{SiO}_2/\text{TiN}/\text{Al}:\text{HfO}_2/\text{TiN}$ .

then fatigued using a bipolar 14 V square waveform at 5 kHz for 1 second, then another LDV measurement was taken. This was repeated for up to 30k cycles. With an increasing number of cycles the maximum positive displacement keeps decreasing, however, the negative displacement remains consistent after 5k. Fatigue of an antiferroelectric 900 nm thick  $(\text{Pb}_{0.97}\text{La}_{0.02})(\text{Zr}_{0.90}\text{Sn}_{0.05}\text{Ti}_{0.05})\text{O}_3$  (PLZST) thin films cantilevers has been reported previously with the displacement decreasing to 80% of its initial value by  $10^8$  cycles<sup>23</sup>, however, the details of the applied waveform were unreported. Kirbach *et al.* calculated the piezoelectric coefficient,  $d_{33,f}$ , of an unreleased 2.7 cat% Si:HfO<sub>2</sub> thin film using a double beam laser interferometry

(DBLI) as 17.9 pm/V, but it rapidly decreased to 0 pm/V after 60k of electric field cycles at 3MV/cm<sup>18</sup>. The work conducted by Kirbach *et al.* suggests that the fatigue experienced by the Al:HfO<sub>2</sub> thin film cantilever in this work could be improved upon with fine tuning the dopant concentration.

## References

- 1 Choong-Ki Lee, Eunae Cho, Hyo-Sug Lee, Cheol Seong Hwang, and Seungwu Han, *Phys. Rev. B* **78** (1), 012102 (2008).
- 2 Min Hyuk Park, Young Hwan Lee, Han Joon Kim, Yu Jin Kim, Taehwan Moon, Keum Do Kim, Johannes Müller, Alfred Kersch, Uwe Schroeder, Thomas Mikolajick, and Cheol Seong Hwang, *Advanced Materials* **27** (11), 1811 (2015).
- 3 T. S. Böske, J. Müller, D. Bräuhaus, U. Schröder, and U. Böttger, *Applied Physics Letters* **99** (10), 102903 (2011).
- 4 Dominik Martin, Johannes Müller, Tony Schenk, Thomas M. Arruda, Amit Kumar, Evgheni Strelcov, Ekaterina Yurchuk, Stefan Müller, Darius Pohl, Uwe Schröder, Sergei V. Kalinin, and Thomas Mikolajick, *Advanced Materials* **26** (48), 8198 (2014).
- 5 S. Kirbach, K. Kühnel, and W. Weinreich, presented at the 2018 IEEE 18th International Conference on Nanotechnology (IEEE-NANO), 2018 (unpublished).
- 6 Clemens Mart, Thomas Kämpfe, Raik Hoffmann, Sophia Eßlinger, Sven Kirbach, Kati Kühnel, Malte Czernohorsky, Lukas M. Eng, and Wenke Weinreich, *Advanced Electronic Materials* **6** (3), 1901015 (2020).
- 7 Jeffrey S. Pulskamp, Alma Wickenden, Ronald Polcawich, Brett Piekarski, Madan Dubey, and Gabe Smith, *Journal of Vacuum Science & Technology B: Microelectronics and Nanometer Structures Processing, Measurement, and Phenomena* **21** (6), 2482 (2003).
- 8 J. M. Gere and S. P. Timoshenko, *Mechanics of materials*. (PWS Publishing Company, Boston, 1997).
- 9 Manuel Rivas, Ryan Q. Rudy, Bradley Sanchez, Milena B. Graziano, Glen R. Fox, Paul Sunal, Latha Nataraj, Emil Sandoz-Rosado, Asher C. Leff, Bryan D. Huey, Ronald G. Polcawich, and Brendan Hanrahan, *Journal of Materials Science* **55** (24), 10351 (2020).
- 10 Young S. Kang, Shashi K. Sharma, Jeffrey H. Sanders, and Andrey A. Voevodin, *Tribology Transactions* **51** (6), 817 (2008).
- 11 Nathan Nelson-Fitzpatrick, Csaba Guthy, Somayyeh Poshtiban, Eric Finley, Kenneth D. Harris, Brian J. Worfolk, and Stephane Evoy, *Journal of Vacuum Science & Technology A* **31** (2), 021503 (2013).
- 12 Hyun-Ju Choi and Yongseong Kim, *Bulletin of the Korean Chemical Society* **38** (10), 1246 (2017).
- 13 R. Materlik, TU Dresden, 2019.
- 14 S. Dutta, Pratyush, B., Glinsek, S., Richter, C., Aramberri, H., Lu, H., Schroeder, U., Defay, E., Gruverman, A., Iniguez, J., *Condensed Matter* (2021).
- 15 Wuyi Pan, Qiming Zhang, Amar Bhalla, and Leslie E. Cross, *Journal of the American Ceramic Society* **72** (4), 571 (1989).
- 16 R. Materlik, C. Künneth, and A. Kersch, *Journal of Applied Physics* **117** (13), 134109 (2015).
- 17 J. Liu, S. Liu, L. H. Liu, B. Hanrahan, and S. T. Pantelides, *Physical Review Applied* **12** (3), 034032 (2019).
- 18 S. Kirbach, M. Lederer, S. Eßlinger, C. Mart, M. Czernohorsky, W. Weinreich, and T. Wallmersperger, *Applied Physics Letters* **118** (1), 012904 (2021).
- 19 Sergej Starschich, David Griesche, Theodor Schneller, and Ulrich Böttger, *ECS Journal of Solid State Science and Technology* **4** (12), P419 (2015).

- 20 Jian Liu, Shi Liu, Jia-Yue Yang, and Linhua Liu, *Phys. Rev. Lett.* **125** (19), 197601  
(2020).
- 21 Paul Muralt, *Journal of the American Ceramic Society* **91** (5), 1385 (2008).
- 22 L. M. Garten and S. Trolier-McKinstry, *Applied Physics Letters* **105** (13), 132905  
(2014).
- 23 Meysam Sharifzadeh Mirshekarloo, Lei Zhang, Kui Yao, and Thirumany Sritharan,  
*Sensors and Actuators A: Physical* **187**, 127 (2012).

## Chapter 6: Conclusions and Future Outlook

### 6.1. Conclusions

The contributions from the studies conducted for this dissertation include the design of a characterization platform for 3D ferroelectric thin films and demonstration of the device characterizations made available by the platform through the measurement of an AFE-like 4 at% Al:HfO<sub>2</sub> thin film. From a single ALD growth, electrical characteristics of AECs were measured, the crystal structure of the sidewall thin film was analyzed, and the piezoelectric response of the thin film was also measured. This work included the first ever measured value for the indirect transverse piezoelectric coefficient,  $e_{31,f}^*$ , for a ferroelectric HfO<sub>2</sub> based thin film, and it was positive. The positive nature of the transverse piezoelectric coefficient was opposite of what was predicted by first-principles calculations<sup>1</sup>, indicating that the Al:HfO<sub>2</sub> thin film would expand in response to an applied electric field<sup>2</sup>. Prior to the deposition of the 3D ferroelectric thin film, this work also established the temperature sensitivity of the loss tangent and leakage current values for AFE-like HfO<sub>2</sub>-based thin films, which are two often underreported values that are critical to the implementation of these materials in commercial devices.

In Chapter 3, the structures that the 3D ferroelectric thin film characterization platform contains are outlined in detail. The substrate contains arrays of planar capacitors to conduct electrical measurements on, such as P-E loop measurements or leakage current density measurements. Measuring many planar devices enables the evaluation of the consistency of the response of the material from device to device, as well as the calculation of some reliability metrics, such as the Weibull modulus of the breakdown voltage. AECs consisting of trenches, holes, or pillars of various density and aspect ratio were also designed onto the platform. These structures enable the evaluation of the ability of the ALD grown thin film to conformally coat

structures with different aspect ratios. The AECs can also be evaluated for energy storage applications. Dense large arrays of trenches were incorporated to facilitate the XRD characterization of the sidewall thin film. Cantilever structures of various types and lengths were designed onto the platform in order to enable the calculation of the indirect piezoelectric coefficient for the thin films. These thin films are increasingly being considered for piezoMEMS applications and for bulk acoustic resonators, thus, various actuators such as chevron actuators and resonators are included on the substrate as well.

Chapter 3 also outlines the process flow and use of the 5 optical masks to create the 3D structured substrate. The process requires the capability to spin coat and spray coat on photoresist in a conventional photolithography process, a deep reactive ion etcher to create the AECs, an ion mill for defining top and bottom electrodes, the use of XeF<sub>2</sub> to release the cantilever structures, and the capabilities of growing the electrodes and ferroelectric thin film via ALD.

A necessary step in the development of the 3D ferroelectric Al:HfO<sub>2</sub> thin film was the creation and analysis of planar Al:HfO<sub>2</sub> thin films. In Chapter 4, a comparison study of the ESD and  $\eta$  at theoretical  $V_{op}$  of Al:HfO<sub>2</sub> thin films with either 4 at% or 8 at% doping concentration and at either 20 nm or 50 nm thick was conducted. The very slim P-E loop of the Pt/50 nm 8 at% Al:HfO<sub>2</sub>/Pt capacitor resulted in the capacitor maintaining high  $\eta$  even at high fields. As much as ESD values are reported, the study revealed that  $V_{op}$  and  $V_{BD}$  should also be considered when testing and developing thin film capacitors as well as parameters such as loss tangent. These samples had the lowest reported loss tangents to date for ferroelectric HfO<sub>2</sub>-based thin films, remaining under 2% even over a frequency range of 4 orders of magnitude.

In the second half of Chapter 4, a study comparing the effect electrodes, Pt and TiN, can have on the electrical response of 50 nm 4 at% Al:HfO<sub>2</sub> thin films along with their temperature and frequency stability was reported. Despite having different electrode materials, which was expected to induce different defect chemistries in the thin films<sup>3,4</sup>, both the Pt/50 nm 4 at% Al:HfO<sub>2</sub>/Pt capacitors as well as the TiN/50 nm 4 at% Al:HfO<sub>2</sub>/TiN capacitors had extremely temperature stable P-E loops, relative dielectric permittivities, and loss tangents from -125 °C to 125 °C. The main difference in the two types of capacitors was their  $P_{max}$  values, with the TiN/50 nm 4 at% Al:HfO<sub>2</sub>/TiN capacitors obtaining a  $P_{max}$  value higher than that of the Pt/50 nm 4 at% Al:HfO<sub>2</sub>/Pt capacitors. GIXRD patterns suggested this was due to the TiN/ 50 nm 4 at% Al:HfO<sub>2</sub>/TiN capacitors having a higher orthorhombic phase fraction than the Pt/50 nm 4 at% Al:HfO<sub>2</sub>/Pt capacitors. The stable  $P_r$  in both samples, from -125 °C to 125 °C, suggests that the driving mechanism for the AFE-like response in these samples was not affected by temperature. However, both types of capacitors experienced wake-up with electric field cycling with the both types of capacitors demonstrating a higher  $dP_r/dN$  per electric at 125 °C versus 25 °C or -125 °C. This increased  $dP_r/dN$  with increasing temperature suggests the driving mechanism for the AFE-like response in the materials to be due to charged defects, which become more mobile at higher temperatures.

In Chapter 5, the unique suite of device characterization measurements enabled by the 3D structured characterization platform is demonstrated using a thin film stack consisting of SiO<sub>2</sub>/TiN/ 50 nm 4 at% Al:HfO<sub>2</sub>/TiN. An AEC was demonstrated to have increased  $P_{max}$  and ESD over its planar counterpart and even greater than the estimated surface area enhancement would have predicted. XRD measurements were conducted on a large arrays of trenches, first prior to ion milling the trench capacitor, yielding a pattern of the full trench capacitor, then after

the trench structure was ion milled, resulting in an XRD pattern from just the sidewall thin films. These XRD patterns revealed a distinct difference in o111/t101 HfO<sub>2</sub> peak between the full capacitor, containing planar and sidewall thin film, and just the sidewall thin film. The full capacitor had a broader peak, demonstrating a higher concentration of tetragonal phase present in the full capacitor than in simply the sidewall thin film. The first reported actuation of a ferroelectric HfO<sub>2</sub>-based cantilever was also detailed. The  $e_{31,f}^*$  at 0 field calculated for the material was 1.38 C/m<sup>2</sup>, which was extremely close but opposite in sign of values calculated for ferroelectric HfO<sub>2</sub>-based thin films from first principles<sup>1,2</sup>. This opposite sign could indicate a volume expansion of the unit cell with increasing electric field, indicative of a phase transition from t-phase to o-phase. The positive nature could also indicate the material has at least some classic AFE phase present in the material, i.e. the polarization of unit cells are aligned antiparallel to one another<sup>5</sup>. The  $e_{31,f}^*$  might naturally be positive if the material has a negative  $e_{33,f}$ <sup>6</sup>, as one axis contracts the other expands in response to the applied electric field. However, if the Al:HfO<sub>2</sub> thin films have a positive  $e_{33,f}$ <sup>7-9</sup>, then the Al:HfO<sub>2</sub> thin films could be electrically analogous to auxetic materials in that it could expand in response to an applied electric field<sup>10</sup>. No matter the origin of the positive transverse piezoelectric coefficient, the fact that it is positive make the thin ALD grown Al:HfO<sub>2</sub> thin films an interesting material for future piezoMEMS applications.

## 6.2. Future Work

### 6.2.1. Fine Tuning Dopant Concentration of Al:HfO<sub>2</sub>

Mueller *et al.* conducted the initial study of Al-doped HfO<sub>2</sub> thin films and demonstrated that  $P_r$  and relative dielectric permittivity were dependent on the Al-dopant concentration, shown in Figure 6.1.<sup>11</sup> Kühnel *et al.* demonstrated the role Si-dopant concentration can have on ESD

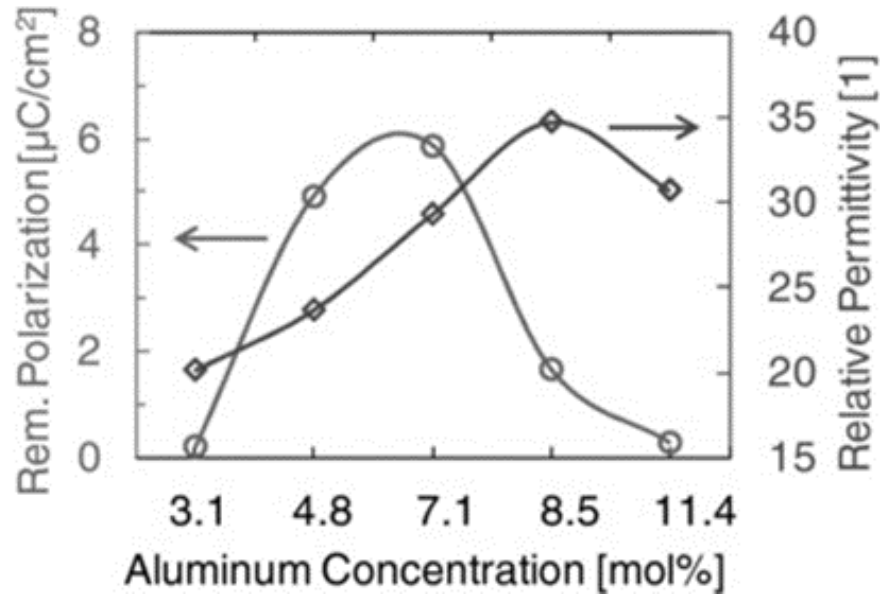


Figure 6.1. A plot of  $P_r$  and relative dielectric permittivity as a function of Al-dopant concentration in HfO<sub>2</sub> thin films.<sup>1</sup>

and  $\eta$  values, as shown in Figure 6.2., which demonstrated a peak in ESD around 6 at%<sup>12</sup>. The

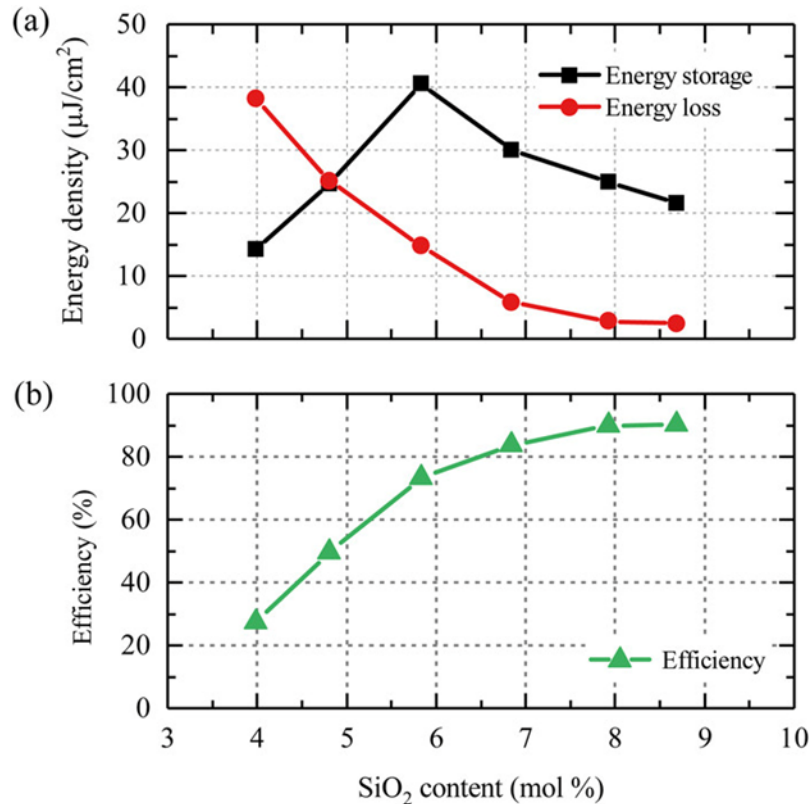


Figure 6.2. Energy storage density, energy loss (a), and efficiency (b) at 3 V of planar 10 nm thick Si:HfO<sub>2</sub> thin films as a function Si-dopant concentration. Reprinted with permission from [Kati Kühnel, Malte Czernohorsky, Clemens Mart, and Wenke Weinreich, Journal of Vacuum Science & Technology B 37 (2), 021401 (2019). Copyright 2019, American Vacuum Society.

ESD and  $\eta$  values reported in this work for 4 at% and 8 at% Al:HfO<sub>2</sub> thin films suggests that a 6 at% Al:HfO<sub>2</sub> thin film could provide higher ESD values than the 4 at% or 8 at%. The lower electric field transition from AFE to FE than the 8 at% Al:HfO<sub>2</sub> thin films expected in the 6 at% Al:HfO<sub>2</sub> thin films could enable higher ESD values to be reached. The 6 at% Al:HfO<sub>2</sub> thin films would also be expected to have a slimmer loop than that of the 4 at%, resulting in the material still maintaining high  $\eta$  values requisite for these materials to be considered for commercial applications.

The piezoelectric response of the material is another parameter that could be optimized through varying the doping concentration. Kirbach *et al.* demonstrated that the Si-dopant

concentration in Si:HfO<sub>2</sub> thin films the piezoelectric response of the thin films varied<sup>8</sup>. The thin films with either 2.7 cat% or 3.8 cat% Si experienced wake-up with electric field cycling, and a subsequent decrease in  $d_{33,f}$  of the material<sup>8</sup>. The  $d_{33,f}$  of the 2 at% went from 17.8 pm/V to 0 after 60k electric field cycles, while the  $d_{33,f}$  of most AFE-like 5.6 cat% Si:HfO<sub>2</sub> thin film increased from 14.6 to 14.8 after 160k cycles<sup>8</sup>. This suggest that the piezoelectric response of a 6 at% or 8 at% Al:HfO<sub>2</sub> thin film might have higher endurance than that of the 4 at% Al:HfO<sub>2</sub> thin film studied in this work.

### 6.2.2. Other 3D Ferroelectric Thin Film Growth and Characterization

As much as this work demonstrates the versatility of AFE-like Al:HfO<sub>2</sub> thin films for applications such as energy storage and piezoMEMS, there are other ferroelectric thin film materials that could show promise as a 3D ferroelectric thin film. For example, we were recently successful at producing PbHfO<sub>3</sub>, another antiferroelectric thin film material, via ALD<sup>13,14</sup>.

PbHfO<sub>3</sub> thin films maintained low  $P_r$  up to  $10^7$  cycles, as shown in Figure 6.3.<sup>13</sup>. The relative

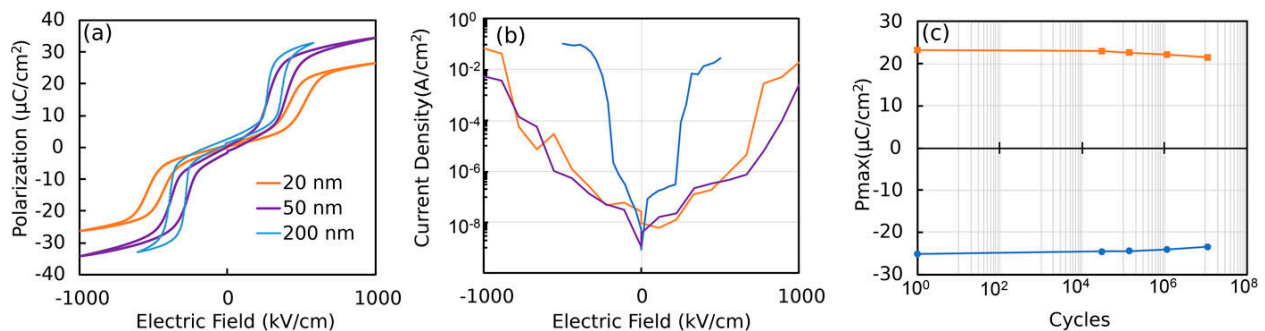


Figure 6.3. (a) P-E loops for a 20nm, 50nm, and 200 nm PbHfO<sub>3</sub> thin films taken at 1 kHz, (b) leakage current density versus applied electric field for each thickness measured, (c) fatigue measurements for the 20 nm thin film. Reproduced from [Brendan Hanrahan, Cosme Milesi-Braut, Asher Leff, Alexis Payne, Shi Liu, Mael Guennou, and Nicholas Strnad, The other model antiferroelectric: PbHfO<sub>3</sub> thin films from ALD precursors, APL Materials **9** (2), 021108 (2021).], with the permission of AIP Publishing.

dielectric permittivity of the PbHfO<sub>3</sub> thin films at zero field was 150. In 2021, Strnad *et al.*

reported the first growth of PbHf<sub>x</sub>Ti<sub>1-x</sub>O<sub>3</sub> (PHT) via ALD in 2021 which showed a zero field

relative dielectric permittivity value of 550<sup>14</sup>. Strnad *et al.* also successfully produced PZT thin films via ALD, with a relative dielectric permittivity of 500 at zero field<sup>14</sup>. Both PHT and PZT thin films produced via ALD are expected to have large piezoelectric responses than that of Al:HfO<sub>2</sub>, and thus could be even more useful materials for piezoMEMS applications.

## References

- 1 R. Materlik, TU Dresden, 2019.
- 2 S. Dutta, Pratyush, B., Glinsek, S., Richter, C. , Aramberri, H. , Lu, H., Schroeder, U.,  
Defay, E., Gruverman, A., Iniguez, J. , Condensed Matter (2021).
- 3 Patrick D. Lomenzo, Qanit Takmeel, Chuanzhen Zhou, Chris M. Fancher, Eric Lambers,  
Nicholas G. Rudawski, Jacob L. Jones, Saeed Moghaddam, and Toshikazu Nishida,  
Journal of Applied Physics **117** (13), 134105 (2015).
- 4 Min Hyuk Park, Han Joon Kim, Yu Jin Kim, Taehwan Moon, and Cheol Seong Hwang,  
Applied Physics Letters **104** (7), 072901 (2014).
- 5 R. Materlik, C. Künneth, and A. Kersch, Journal of Applied Physics **117** (13), 134109  
(2015).
- 6 J. Liu, S. Liu, L. H. Liu, B. Hanrahan, and S. T. Pantelides, Physical Review Applied **12**  
(3), 034032 (2019).
- 7 T. S. Böske, J. Müller, D. Bräuhaus, U. Schröder, and U. Böttger, Applied Physics  
Letters **99** (10), 102903 (2011).
- 8 S. Kirbach, M. Lederer, S. Eßlinger, C. Mart, M. Czernohorsky, W. Weinreich, and T.  
Wallmersperger, Applied Physics Letters **118** (1), 012904 (2021).
- 9 Sergej Starschich, David Griesche, Theodor Schneller, and Ulrich Böttger, ECS Journal  
of Solid State Science and Technology **4** (12), P419 (2015).
- 10 Jian Liu, Shi Liu, Jia-Yue Yang, and Linhua Liu, Phys. Rev. Lett. **125** (19), 197601  
(2020).
- 11 Stefan Mueller, Johannes Mueller, Aarti Singh, Stefan Riedel, Jonas Sundqvist, Uwe  
Schroeder, and Thomas Mikolajick, Advanced Functional Materials **22** (11), 2412  
(2012).
- 12 Kati Kühnel, Malte Czernohorsky, Clemens Mart, and Wenke Weinreich, Journal of  
Vacuum Science & Technology B **37** (2), 021401 (2019).
- 13 Brendan Hanrahan, Cosme Milesi-Brault, Asher Leff, Alexis Payne, Shi Liu, Mael  
Guennou, and Nicholas Strnad, APL Materials **9** (2), 021108 (2021).
- 14 Nicholas A. Strnad, Brendan M. Hanrahan, Daniel M. Potrepka, Jeffrey S. Pulskamp,  
Raymond J. Phaneuf, and Ronald G. Polcawich, Journal of the American Ceramic  
Society **104** (3), 1216 (2021).